



Title	Advanced XAFS analysis for local structure of functional materials
Author(s)	Sirisit, Natee
Citation	北海道大学. 博士(工学) 甲第13392号
Issue Date	2018-12-25
DOI	10.14943/doctoral.k13392
Doc URL	http://hdl.handle.net/2115/80070
Type	theses (doctoral)
File Information	Sirisit_Natee.pdf



[Instructions for use](#)

Advanced XAFS analysis for local structure of
functional materials

先端 XAFS 解析の開発と
機能性物質の局所構造

Natee Sirisit

Division of Quantum Science and Engineering,
Graduate School of Engineering, Hokkaido
University

December 2018

Table of Contents

Acknowledgements	iv
List of Abbreviations	vi
Chapter 1 Introduction	1
1.1. Background	1
1.2. X-ray Absorption Spectroscopy.....	2
1.2.1. XAFS	5
1.2.1.1. XANES	5
1.2.1.2. EXAFS.....	7
1.3. Objective.....	11
Chapter 2 General experimental procedure	16
2.1. Common detector used in the XAFS.....	17
2.1.1. Ionization chamber.....	17
2.1.2. Ge detector	19
2.1.3. Photon counting pixel detector	20
2.2. XAFS data processing.....	23
2.3. EXAFS data analysis	23
Chapter 3 A New Indicator for Single Metal Dispersion on a TiO ₂ (110) Surface Premodified with a Mercapto Compound.....	28
3.1. Introduction.....	28
3.2. Titanium Dioxide or TiO ₂	30
3.2.1. Structural properties of TiO ₂	30
3.2.2. Surface properties of TiO ₂ (110).....	32

3.3. Experimental procedure	33
3.3.1. Sample preparation	33
3.3.2. PTRF-EXAFS	34
3.4. Results and discussion	37
3.4.1. Ni deposition on a TiO ₂ (110) surface premodified with <i>o</i> -MBA (Ni/ <i>o</i> -MBA/TiO ₂ (110)).....	37
3.4.2. Pt deposition on a TiO ₂ (110) surface premodified with <i>o</i> -MBA (Pt/ <i>o</i> - MBA/TiO ₂ (110)).....	43
3.4.3. Formation mechanism of atomically dispersed metal species and small metal clusters on <i>o</i> -MBA/TiO ₂ (110): Comparison of Ni, Pt, Cu, and Au cases	47
3.5. Conclusions.....	50
Chapter 4 What is the origin for Mechanochromism of Gold (I) complex (C ₆ F ₅ Au) ₂ (μ-1,4-Diisocyano benzene) - Direct evidence for the presence of Aurophilic interaction	57
4.1. Background	57
4.2. Experimental procedure	60
4.3. Results and Discussion	62
4.4. Conclusion	71
Chapter 5 Evidence for Multi-Atom Resonance X-ray Raman Spectroscopy - An <i>In Situ</i> Low Z-element and Bond-specific X-ray spectroscopy	76
5.1. Introduction	76
5.2. Experimental procedure	77
5.2.1. Sample preparation	77

5.2.2. Instrument	79
5.3. Results and Discussion	81
5.3.1. Tantalum compound	81
5.3.2. Erbium compound.....	87
5.4. Conclusion	88
Chapter 6 General conclusion.....	92

Acknowledgements

The success of this thesis can be succeeded by the attentive support from a lot of people that cannot be fitted in this limited space. First, I would like to express my deep gratitude to my advisor, Prof. Kiyotaka Asakura, for his supervision, support, encouragement, and giving me the opportunity to work in this research topic, without him my graduate study would not have been possible. It has been a pleasure to work under someone who is an expert in the field of synchrotron X-ray absorption spectroscopy. His excitement and enthusiasm are something I will always remember and admire.

I would like to thank Associate Prof. Satoru Takakusagi for his valuable suggestion and patiently advise me in spite of my zero knowledge about what we were working with. I would also like to thank Prof. Hiroko Ariga-Miwa for her suggestion.

I would like to thank Prof. Yasuhiro Iwasawa and Prof. Tomoya Uruga for their trust and providing me a precious beamtime. I would like to thank Prof. Hajime Ito for providing me with exciting novel materials for X-ray absorption study presented in this thesis.

I would like to thank Assistance Prof. Hiromitsu Uehara for taking care of me when I was working with him in the early year despite knowing nothing what he was doing. It has been a pleasure working with him.

Additionally, I am very grateful for all the technical support I received at Spring-8 from Dr. Oki Sekizawa, and Dr. Tomohiro Sakata. Their expertise and professionalism made my experiences at this facility much more enjoyable.

I would also like to thank members of Prof. Asakura's research group, both past and present, Assistance Prof. Yuki Wakisaka, Dr. Felix Feitan, Dr. Can Liu, Dr. Upendar Kashaboina, Mr. Daiki Kido, Mr. Hiroshi Konno, Ms. Nagisa

Suyama, Mr. Yuya Iwasaki, Mr. Satoshi Seki, Mr. Tohma Kitayama, Mr. Yoshihiro Honda, Mr. Yojiro IWATA, Mr. Yuto Nakamura, Ms. Elizabeth Barrow, Mr. Grant Spencer Seuser, Ms. Yuko Hamagami, Ms. Hiromi Kusakari, Ms. Mayumi Kawashima for all their discussion, and support. In particular, I would like to thank Assistance Prof. Yuki Wakisaka and Mr. Daiki Kido for their companionship on many research trips to synchrotron facilities, and friendly working atmosphere without you the long hours at the beam-line would have not been enjoyable.

I am greatly indebted to Royal Thai government for their financial support. I owe great thanks to my friends in every country for their encouragement and enthusiasm.

Finally, I would like to thank my parents for all their support and encouragement, without them I would not be where I am today.

Natee Sirisit

List of Abbreviations

AFM:	Atomic Force Microscopy
DCM:	Double Crystal Monochromator
DSC:	Differential Scanning Calorimetry
EXAFS:	Extended X-ray Absorption Fine Structures
FTIR:	Fourier Transformed Infrared
FY:	Fluorescence Yield
GOF:	Goodness of Fit
IMSS:	Institute of Materials Structure Science
IR:	Infrared
LEED:	Low-Energy Electron Diffraction
MARPE:	Multi-atom Resonant Photoemission
MBA:	Mercaptobenzoic Acid
MEED:	Medium-Energy Electron Diffraction
PF:	Photon Factory
PL:	Photoluminescence
PTRF-XAFS:	Polarization-dependent Total-Reflection Fluorescence X-ray Absorption Fine Structure
RXRS:	Resonant X-ray Raman Scattering
RIXS:	Resonant Inelastic X-ray Scattering
STM:	Scanning Tunneling Microscopy
TGA:	Thermogravimetric Analysis
UHV:	Ultra-High Vacuum
XAS:	X-ray Absorption Spectroscopy
XAFS:	X-ray Absorption Fine Structures

XANES:	X-ray Absorption Near Edge Structures
XES:	X-ray Emission Spectroscopy
XPS:	X-ray Photoelectron Spectroscopy
XRD:	X-ray Diffraction
XRS:	X-ray Raman Scattering

Chapter 1

Introduction

1.1. Background

Human being has been using catalysts in everyday from gigantic scale in industries to small objects in everyday life [1-4]. Catalysts have been improved day by day for the sake of human being. There are several factors govern the catalyst efficiency such as kind of atom, atom arrangement, structure. Precision catalysis will be the next research topic in the future because of the rise of special demand such as very specific target, efficiency improvement, new application. Precision catalysis requires a synthesis with atomic-level precision because a difference of only one atom might cause significant change in their reactivities and properties. Not only is synthesis an essential for the precision catalysis but also the analysis method to determine the structure precisely. Metal containing compound have drawn much interest because of their wide applications such as catalyst, fuel cell, sensors, electronic and magnetic devices. Microscopic structure plays an important role in precision catalysis compare to the traditional catalyst. To illustrate, the location of Co ions in TiO_2 lattice, for example, Co ions are in the tetrahedral hole, or Co ions are in octahedral hole or even Co ions substitute some of the Titanium cations would affect the physical and chemical properties of the material. This local structure information is crucial to understand and hence develop the better precision catalysis. There are a few techniques able to obtain the local structure information. One of the techniques is X-ray absorption fine structure or XAFS. XAFS is a versatile, powerful, and unique tool for studying structure of materials in chemistry, biology, physics, and other fields [5-15]. In this study, the local structure of various systems which show unique properties, but it is difficult to obtain its structure, has been investigated. In addition, the evidence which might lead to the brand-new type of XAFS called MARX-Raman is discussed.

1.2. X-ray Absorption Spectroscopy

First, I would like to review X-ray absorption spectroscopy (XAS), which is the superset of one of the key techniques (XAFS) discussed in this thesis. X-rays are light with energies ranging from ~ 500 eV to 500 keV, or wavelengths from 25 Å to 0.25 Å. At this energy regime, X-ray can either be totally or partially absorbed by all matter. In this process, which is known as the photoelectric effect, an X-ray photon with energy greater than the binding energy of a tightly bound core-level electron is absorbed and the electron is ejected from the atom. The ejected electron has kinetic energy equal to the energy of the incident X-ray minus the binding energy of the electron. As the energy of the incident X-rays approaches the binding energy of a core level electron there is a sharp rise in the absorption coefficient as the cross section of the X-ray increases. This gives rise to experimentally observed absorption edges when an X-ray has sufficient energy to promote a core level electron as shown in figure 1.2 (top). The X-ray absorption

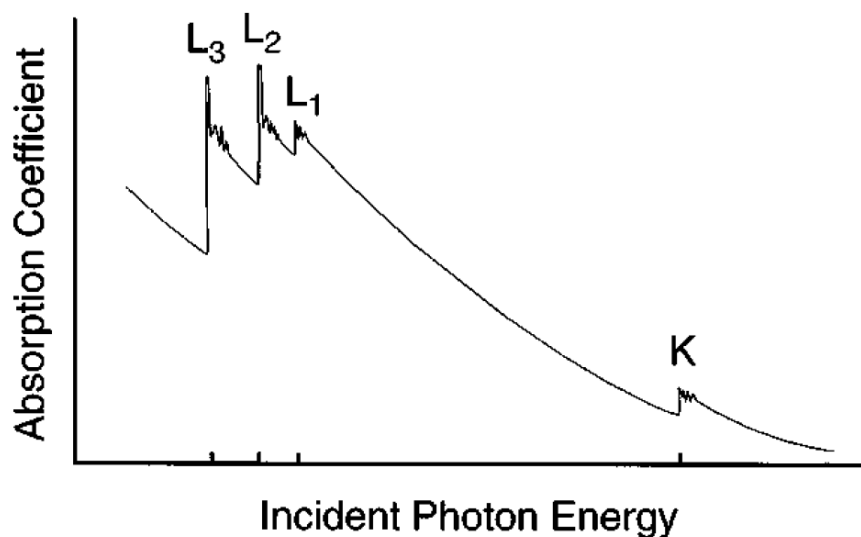


Figure 1.1 Schematic view of x-ray absorption coefficient as a function of incident photon energy. Four x-ray edges are shown: K, L₁, L₂, and L₃. Note that the overall decrease in absorption as a function of energy is punctuated by four sharps, step-function-like increases at each edge. Above each edge are the oscillatory wiggles known as the EXAFS.

coefficient or $\mu(E)$ is calculated from the decrease of X-ray intensity with distance x as its relationship can be written into the following equation.

$$\mu(E) = \frac{-d \ln I}{dx}$$

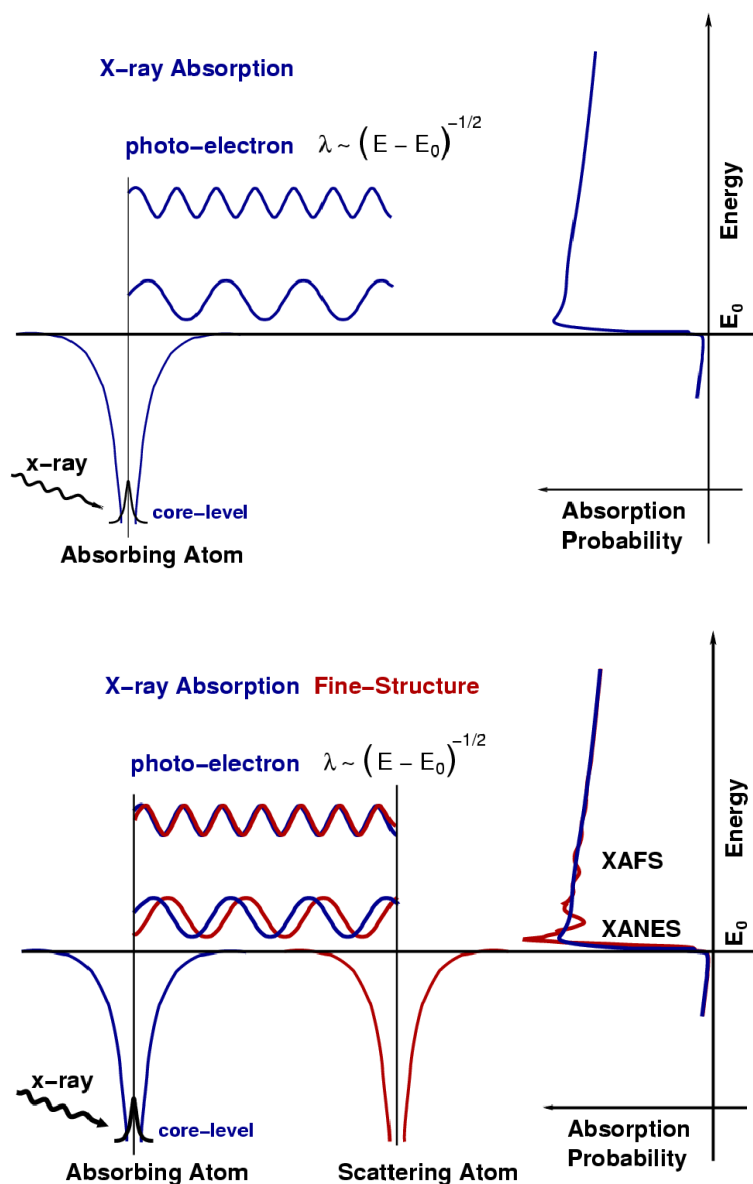


Figure 1.2 (Top) X-ray absorption in a single atom system, and (bottom) X-ray absorption fine structure (XAFS) in a multi-atom system.

In an isolated atom, $\mu(E)$ smoothly decrease as the X-ray energy increase, figure 1.2 (top). At specific energies which are the characteristic of the atoms in the material, however, there are sharp increases called X-ray absorption edges (E_0) as mentioned previously. There are the results of absorption of X-ray photon by the core shell electron in the atoms to the vacuum level. The atomic mass photo-absorption cross-section as a function of X-ray energy is shown in figure 1.1 [16]. The K-edge refers to the excitation of 1s electrons, the L₁-edge refers to excitation of 2s electrons, and the L₃- and L₂-edges refer to the excitation 2p_{3/2} and 2p_{1/2} electrons respectively. Since every atom has core-level electrons with well-defined binding energies, we can select the element to probe by tuning the x-ray energy to an appropriate absorption edge. The edge energies vary with atomic number approximately as Z^2 , which allows most elements to be probed by XAS with x-ray energies between 5 and 35 keV. Thus, making XAS is an element-specific method.

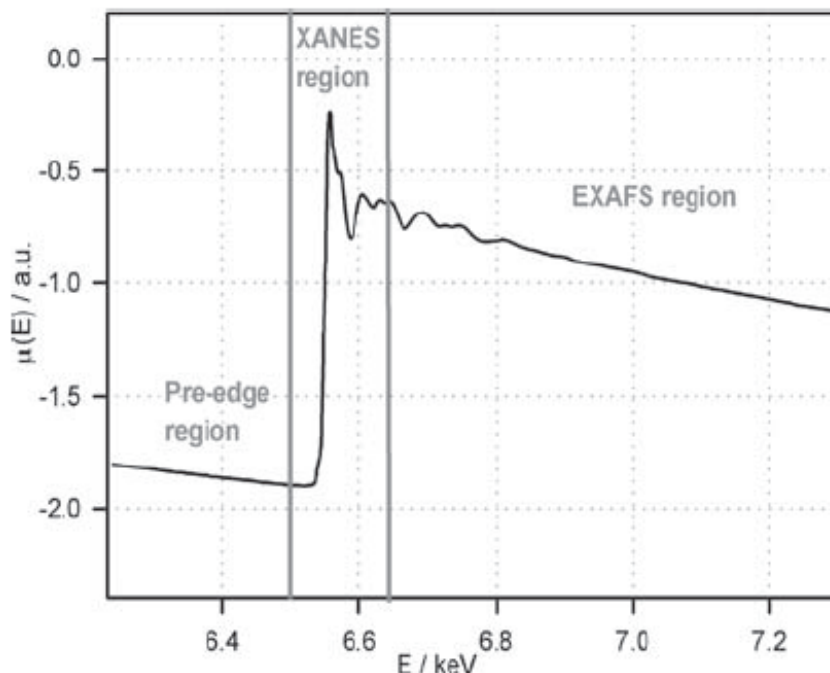


Figure 1.3 Example of an X-ray absorption spectrum, in which the Prepeak-, XANES-, and EXAFS-regions are formally separated from each other.

1.2.1. XAFS

In a multiatomic system, nevertheless, fine structures are observed in μ when outgoing photoelectrons of the absorbing atom interact with neighboring atoms resulting in scattering and subsequent constructive and destructive interference of the outgoing and scattered wavefunctions. The schematic of X-ray absorption in a single atomic system and XAFS in a multi-atom system are compared and illustrated in figure 1.2. The modulation of the absorption coefficient as a function of X-ray excitation energy when the absorbing atom is in a chemical environment is known as X-ray absorption fine structure (XAFS). XAFS includes both Extended X-ray Absorption Fine Structure (EXAFS) and X-ray Absorption Near Edge Structure (XANES) as shown in figure 1.3 [8, 9]. XAFS is a versatile, powerful, and unique tool for studying structure of the materials in chemistry, biology, physics, and other fields [6-10, 17]. It is a subcategory of X-ray absorption spectroscopy. XAFS provides bond distances, type of atoms and coordination numbers around the X-ray absorbing atom. The region within 50 eV of an absorption edge is called XANES region, while the region beyond 50 eV to over 1000 eV is called EXAFS region. This division is owing to the difference in scattering behavior of the electron as a function of its kinetic energy. XAFS occurs because the photo-electron can scatter from a neighboring atom. The scattered photoelectron can return to the absorbing atom, modulating the amplitude of the photoelectron wave-function at the absorbing atom. This, in turn, modulates the absorption coefficient $\mu(E)$, causing the XAFS.

1.2.1.1. XANES

X-ray absorption near-edge structure (XANES) spectroscopy using synchrotron radiation is a well-established technique providing information on the electronic, structural and magnetic properties of matter [18]. In XANES, a photon is absorbed, and an electron is excited from a core state to an empty state. To excite an electron in a given core-level, the photon energy has to be equal to or higher than the binding energy of this core-level. When we perform the XANES experiment, the changes in the absorption of X-rays due to the photoelectric effect is measured. At a certain energy, a sharp rise in the absorption

will be observed. This sharp rise in absorption is called the absorption edge. In a multi-atom system, there are scattering contributions to the absorption coefficient (μ) from all the neighboring atoms resulting in multiple scattering pathways.

The absorption coefficient, $\mu(E)$, is in theory proportional to the probability that an X-ray photon will be absorbed by an electron in the absorbing atom producing a transition between initial and final quantum states as described by Fermi's Golden Rule

$$\mu(E) = |\langle \psi_i | H | \psi_f \rangle|^2 ; H = (\hat{\epsilon} \cdot \vec{r}) e^{i(\hat{k} \cdot \vec{r})} \quad (1)$$

where ψ_i is the initial state function which describes a core-level electron, X-ray photon, and no photoelectron; ψ_f is the final state function which describes a photoelectron, core-hole, and No X-ray; and H is the interaction Hamiltonian between the electromagnetic field of the X-ray and the electron. The Hamiltonian expression includes the electric field vector of the X-ray ϵ , the forward scattering vector k , and the electron coordinate vector r . If we further expand the Hamiltonian, we get

$$H = (\hat{\epsilon} \cdot \vec{r}) + (\hat{\epsilon} \cdot \vec{r})(\hat{k} \cdot \vec{r}) + \dots \quad (2)$$

XANES is dominated by the first term in equation (2) which is the dipole moment. The quadrupole transition is more than 100 times smaller and often can be neglected. However, this transition becomes important in the case of the K-edge XANES of transition metals because of its sensitivity to metal d-electron-ligand hybridization. In this case, the 3d density of states is much larger than the 4p density of states and the quadrupole peaks appear in the pre-edge region where there is no 4p density of states.

The incident X-ray photon energy in the XANES region is equal to or just above (~ 10 's of eV) the absorption threshold E_0 resulting in transitions of the core-level electron into previously bound and quasi-bond states. In actuality, there is not a sharp boundary between XANES and EXAFS, so choosing an energy of demarcation is somewhat arbitrary. The IUCr Dictionary suggests

around 50 eV above E_0 (IUCr 2011), but 30 eV above E_0 is also commonly used [9]. The theory of XANES is less well developed than EXAFS, but strides are being made. We can now predict the general characteristics of XANES resulting from most structures.

1.2.1.2. EXAFS

Extended X-ray Absorption Fine Structure or EXAFS appears in the X-ray absorption spectrum 100 – 1000 eV above the X-ray absorption edge [16, 19]. In this region, incident photon whose energy exceeds the core binding energy will eject core electron. The photoelectron ejected by the absorption process travels outward the X-ray absorbing atom as a spherical wave. When the excited atom is surrounded by other atoms, the outgoing spherical photoelectron wave is scattering back toward the X-ray absorbing atoms. The phase of the reflected wave depends on the photoelectron wavelength and the atomic number of the scatterer. This photoelectron interference modifies the absorption cross section and results in modulation of transmitted X-ray intensity over a range of 50 – 1500 eV. The resulting modulation is called EXAFS. The amplitude of modulation depends on the atomic number and the backscattering strength of the neighboring atoms and the distance from absorbing atom.

The EXAFS function $\chi(E)$ can be defined as

$$\chi(E) = \frac{\mu(E) - \mu_0(E)}{\Delta\mu_0(E)} \quad (3)$$

where $\mu(E)$ is the experimentally measured absorption coefficient, $\mu_0(E)$ is a smooth background function representing the absorption of the X-ray by an isolated atom, and $\Delta\mu_0(E)$ is the measured jump in absorption at the threshold energy (the binding energy of the core-level electron, E_0). The example of Au (I) complex, $[(C_6F_5Au)_2(\mu-1,4\text{-diisocyanobenzene})]$, spectrum in $\mu(E)$ is shown in figure 1.4. It is a good practice to describe EXAFS by the wave behavior of the photoelectron created in the X-ray absorption process, it is common to convert the X-ray energy to wavenumber (k) which is defined as

$$k = \frac{1}{\hbar} \sqrt{2m_e(E - E_0)} \quad (4)$$

where m_e is the electron mass. The example of Au (I) complex, $[(C_6F_5Au)_2(\mu-1,4\text{-diisocyanobenzene})]$ (figure 1.4), spectrum converted to k is shown in figure 1.5. After conversion, the data are now ready for analysis. In many cases, however, an additional transformation is employed. Considering the EXAFS equation as defined in equation 5, we can see that each individual term is a modulated sinusoidal. Adding up multiple sine waves of different amplitudes periods, and phase will cause something look like in figure 1.5. The transformation needed to decompose a function into constitute sine waves is the Fourier transformation. After applying the Fourier transformation, the resulting spectrum can look something like figure 1.6. The transform of the Au (I) complex shows multiple peaks because there are several shells of scattering atoms at somewhat well-defined distances.

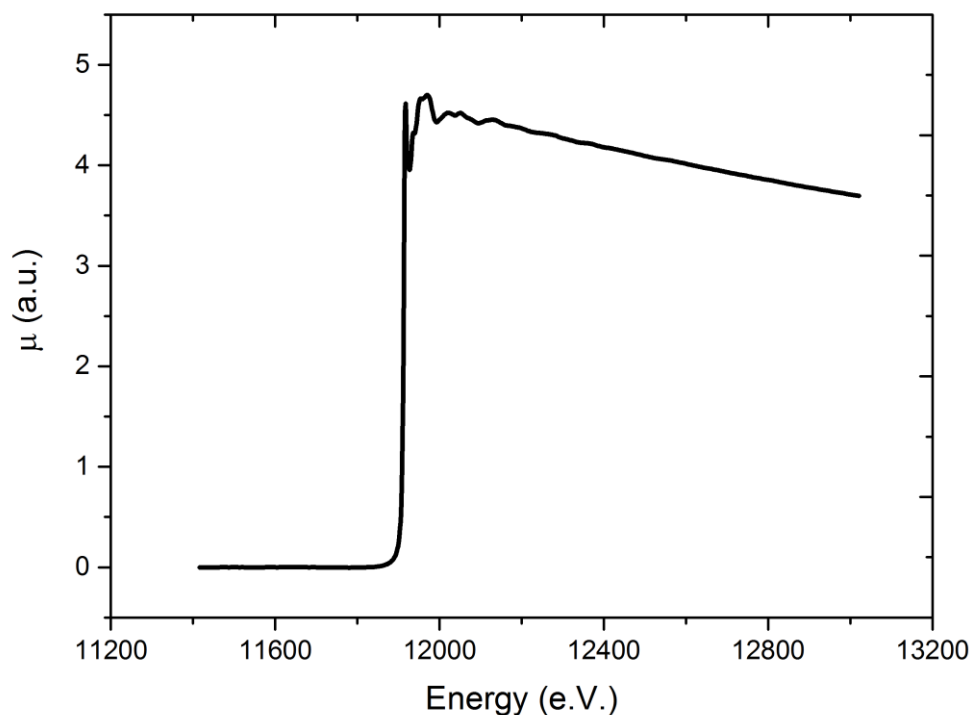


Figure 1.4 $\mu(E)$ for a Gold(I) complex, $[(C_6F_5Au)_2(\mu-1,4\text{-diisocyanobenzene})]$.

$$\chi(k) = S_0^2 \sum_i N_i \frac{f_i(k)}{kD_i^2} e^{-\frac{2D_i}{\lambda(k)}} e^{-2k^2\sigma_i^2} \sin(2kD_i + \delta_i(k)) \quad (5)$$

Because EXAFS is the short-range order technique, element specific, and able to provide the local structure, it is the most suitable tool for investigating metal nanoparticles on supports. By subtracting, the metal-metal bond contribution from the EXAFS oscillation, the metal-oxygen bond length can be elucidated. However, Metal-support bonds such as metal-oxygen and metal-cation bonds contribute to the EXAFS oscillation much less than metal-metal bonds in the metal particles. Therefore, it is difficult to clearly differentiate metal-oxygen bonds from strong metal-metal bonds and large uncertainties are involved in such data analyses [20]. Moreover, the information gained from the conventional EXAFS comes from all of the X-ray absorbing atoms. It would be better for the analysis of metal nanoparticles on supports if the information only

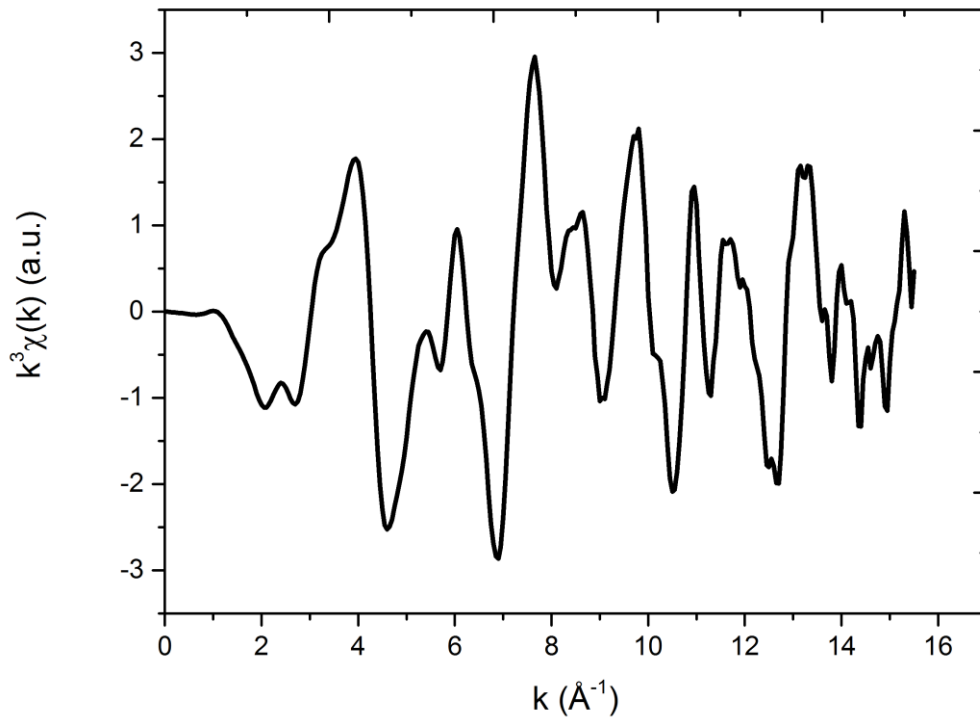


Figure 1.5 $k^3\chi(k)$ of figure 1.4.

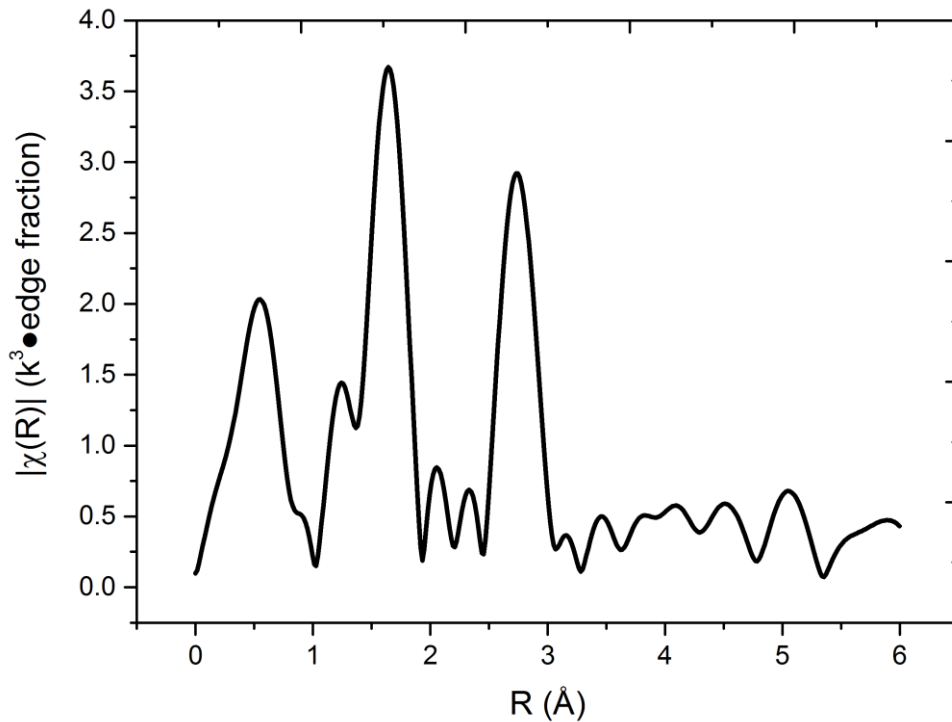


Figure 1.6 Fourier transformation of spectrum in figure 1.4.

comes from the surface where the metal deposited. Polarization-dependent Total-Reflection Fluorescence X-ray Absorption Fine Structure (PTRF-XAFS) analysis can improve such analysis by uniquely provide three-dimensional structural information of the metal species on single crystal surface [20-28].

In EXAFS analysis, we are usually fitting either the Fourier transform or the back-transform. The number of independent points, the number of parameters that we can use in the fitting, is defined by equation 6.

$$N_{ind} = \frac{2(k_{max} - k_{min})(R_{max} - R_{min})}{\pi} \quad (6)$$

Stern et al. suggested that equation 6 could be modified by “+1” or “+2” added to it [29]. However, all of these suggestions are based on the assumption that the data are ideally packed which are unlikely in the actual system. Usually, the number of parameters available for use in the fitting is very limited. For

example, we will have 9 independent points (calculated from equation 6) available if we analyze the data from $k = 3.0 - 10.0 \text{ \AA}^{-1}$ and $R = 1.0 - 3.1 \text{ \AA}$. If you vary the value of E_0 , coordination number (N), bond distance (D), and Debye-Waller factor (σ) in the fitting process, you can only fit the spectrum up to 2 shells. It sounds like a lot, but it is not if you analyze the complicated system. In the system composed of a lot of atoms, and there is a possibility that any atoms can be closed to the x-ray absorbing atom, you might find that you need more than 2 shells in the curve fitting. In addition, you need to be careful when performing the fitting if your system has the atom that slightly contributes to the overall EXAFS oscillation. It can be found that the obtained R-factor (the factor used to identify whether it is a good fit or not) is reasonably good even though the fitting is excluded the atom that contributes slightly.

1.3. Objective

X-ray absorption fine structure (XAFS) provides bond distance, a type of atom, and coordination number around the X-ray absorbing atom. Therefore, it is suitable to determine the local structure of the compounds. XAFS is the most suitable technique to identify its local structure. However, there are several drawbacks in XAFS as mentioned earlier making it difficult to obtain the desired local structural information for the particular system. In this study, I demonstrate how to overcome the drawbacks by applying several techniques in the investigation of the local structure of various systems which show unique properties, but it is difficult to obtain its structure from EXAFS.

1. Conventional XAFS provides one-dimensional local structural information. Nevertheless, three-dimensional local structural information is preferred for the dispersed metal species on metal oxide surface in order to elucidate the complete local structure around the metal species. Such information was obtained by the technique so-called PTRF-XAFS which was demonstrated in Chapter 3.
2. The number of independent points is limited in EXAFS. Thus it is difficult to analyze the complex system which contains many atoms (scattering shells), so the number of parameters uses in the curve fitting. Moreover, care must be taken for the system potentially having scattering shell that slightly contributes to the overall EXAFS

oscillation. It was overcome by employing the Hamilton test or F-test which was demonstrated in Chapter 4.

3. It is quite difficult to observe the XAFS of the low-Z element under the reaction conditions. I demonstrated the evidence which might lead to the development of a new kind of spectroscopy, which has coined the name as Multi-Atom Resonant X-ray Raman (MARX-Raman). It will be a new way to perform an *in situ* XAFS measurement for low Z-element with bond-specific capability.

The thesis is composed of 6 chapters to describe my contributions to new development in XAFS techniques.

Chapter 1 is the introduction and background of the study.

In Chapter 2, the general experimental procedure is described.

In Chapter 3, I describe a method for determining the three-dimensional structure of supported metal catalysts. Supported metal catalysts have drawn much attention for their wide applications such as catalysts, sensors, electronic and magnetic devices. It is very important to control the structure and electronic state of the supported metal, including the metal cluster size. Metal oxides are widely used as substrates for preparing highly dispersed metal clusters with their size less than a few nm. To investigate the metal-metal oxide interaction, a well-defined single crystal metal oxide is needed as a model substrate. In addition, an analysis method capable of providing three-dimensional structural information of the surface species is essential. Polarization-dependent Total-Reflection Fluorescence X-ray absorption fine structure (PTRF-XAFS) analysis can uniquely provide such information around highly dispersed metal species on the single crystal surface. In this study, Ni and Pt were deposited on TiO₂(110) surfaces premodified with ortho-mercaptobenzoic acid (o-MBA). I will demonstrate that three-dimensional structural information of the highly dispersed metal species on the single crystal surface could be obtained by PTRF-EXAFS, unlike conventional EXAFS which cannot provide such information. Moreover, A new indicator, R_{X-M-O} (X=S or O), has been proposed for the single metal dispersion on the TiO₂(110) surface.

In Chapter 3, I talk about XAFS applications to the unique compound (the gold (I) complex, [(C₆F₅Au)₂(μ-1,4-diisocyanobenzene)] (1)) (JACS, 2008 130 100044). The compound undergoes the reversible color change from blue to yellow by mechanical treatment (mechanochromism), the origin of which remains unknown. The mechanochromism draws a lot of interest because it can be used as recording and sensing materials. The origin of the color change was

postulated to be due to the creation of Auophilic interaction. However, the ground Au complex structure remained unknown because of its amorphous structure. I will demonstrate that, by employing XAFS study, the change of local structure of the ground Au complex can be elucidated. In addition, I will also demonstrate how Hamilton test or F-test plays an important role in curve fitting analysis of the complicated system in which slightly contribution to the overall oscillation of the atomic species could be identified.

In Chapter 5, I report the evidence that might lead to the brand-new kind of spectroscopy. XAFS that has been used in the aforementioned provides invaluable local structural information. Since the X-ray has a large penetration ability, it is possible to carry out an *in situ* measurement of catalysts and electrodes under reaction conditions. However, when applied to low Z elements, which have an X-ray absorption edge in the soft X-ray regime, it is quite difficult to observe the XAFS under the reaction conditions. On the other hand, X-ray Raman scattering (XRS) can provide *in situ* XAFS measurements on low Z elements because the XRS uses hard X-rays. However, the X-ray Raman intensity is quite low. Resonant XRS is observed and enhances the Raman sensitivity. In this resonant XRS, the X-ray is tuned to the absorption edge and the Raman signal of the same X-ray absorbing atom is detected. Therefore, the X-ray absorption and Raman emission occur at a single atom. If one uses an absorption edge of the central metal in a metal complex to which low Z atoms are directly coordinated and if the excitation energy transfer occurs from the X-ray absorbing atom to the coordinating low Z atoms, one can obtain the X-ray Raman spectrum of the directly bonded low Z atoms, which is enhanced through the X-ray absorption of the central atom. In this study, the interatomic resonant Raman signals were measured by tuning the X-ray to the excitations of Ta L₃-edge and Er L₁-edge with the detection of Raman emission of N K-edge and C K-edge, respectively, in order to see such an enhancement occurs or not, qualitatively.

Chapter 6 provides a general conclusion and gives future directions for this research.

References

- [1] S.S. Zumdahl, D.J. DeCoste, *Introductory chemistry: A foundation*, Cengage learning, 2018.
- [2] R. Chang, J. Overby, *Chemistry*, 13 ed., McGraw-Hill Education, 2018.
- [3] T.L. Brown, *Chemistry: The Central Science*, Pearson, 2015.
- [4] S.S. Zumdahl, S.A. Zumdahl, *Chemistry*, 9 ed., Cengage Learning, 2013.
- [5] D. Koningsberger, R. Prins, *X-ray absorption: principles, applications, techniques of EXAFS, SEXAFS, and XANES*, (1988).
- [6] Y. Iwasawa, *X-ray absorption fine structure for catalysts and surfaces*, World Scientific, 1996.
- [7] G. Bunker, *Introduction to XAFS: a practical guide to X-ray absorption fine structure spectroscopy*, Cambridge University Press, 2010.
- [8] S. Gross, M. Bauer, EXAFS as Powerful Analytical Tool for the Investigation of Organic–Inorganic Hybrid Materials, *Advanced Functional Materials*, 20 (2010) 4026-4047.
- [9] S. Calvin, *XAFS for Everyone*, CRC press, 2013.
- [10] Y. Iwasawa, K. Asakura, M. Tada, *XAFS Techniques for Catalysts, Nanomaterials, and Surfaces*, Springer International Publishing, Cham, 2017.
- [11] C. Hardacre, Application of EXAFS to molten salts and ionic liquid technology, *Annual Review of Materials Research*, 35 (2005) 29-49.
- [12] M. Askerka, G.W. Brudvig, V.S. Batista, The O₂-Evolving Complex of Photosystem II: Recent Insights from Quantum Mechanics/Molecular Mechanics (QM/MM), Extended X-ray Absorption Fine Structure (EXAFS), and Femtosecond X-ray Crystallography Data, *Accounts of Chemical Research*, 50 (2017) 41-48.
- [13] A. Levina, R.S. Armstrong, P.A. Lay, Three-dimensional structure determination using multiple-scattering analysis of XAFS: applications to metalloproteins and coordination chemistry, *Coordination Chemistry Reviews*, 249 (2005) 141-160.
- [14] A.E. Russell, A. Rose, X-ray Absorption Spectroscopy of Low Temperature Fuel Cell Catalysts, *Chemical Reviews*, 104 (2004) 4613-4636.
- [15] F. Lin, Y. Liu, X. Yu, L. Cheng, A. Singer, O.G. Shpyrko, H.L. Xin, N. Tamura, C. Tian, T.-C. Weng, X.-Q. Yang, Y.S. Meng, D. Nordlund, W. Yang, M.M. Doeff, Synchrotron X-ray Analytical Techniques for Studying Materials Electrochemistry in Rechargeable Batteries, *Chemical Reviews*, 117 (2017) 13123-13186.
- [16] J.J. Rehr, R.C. Albers, Theoretical approaches to x-ray absorption fine structure, *Rev. Mod. Phys.*, 72 (2000) 621-654.
- [17] M. Newville, *Fundamentals of XAFS*, University of Chicago, Chicago, IL, 2004.

- [18] G.S. Henderson, F.M. De Groot, B.J. Moulton, X-ray Absorption Near-Edge Structure (XANES) Spectroscopy, *Reviews in Mineralogy and Geochemistry*, 78 (2014) 75-138.
- [19] Y. Iwasawa, K. Asakura, M. Tada, *XAFS Techniques for Catalysts, Nanomaterials, and Surfaces*, Springer Nature, 2016.
- [20] K. Asakura, Polarization-dependent total reflection fluorescence extended X-ray absorption fine structure and its application to supported catalysis, *Catalysis: Volume 24*, The Royal Society of Chemistry, 2012, pp. 281-322.
- [21] W.J. Chun, K. Asakura, Y. Iwasawa, Anisotropic structure analysis for Mo oxides on TiO₂(110) single crystal surface by polarization-dependent total-reflection fluorescence EXAFS, *Chem. Phys. Lett.*, 288 (1998) 868-872.
- [22] W.-J. Chun, Y. Tanizawa, T. Shido, Y. Iwasawa, M. Nomura, K. Asakura, Development of an in situ polarization-dependent total-reflection fluorescence XAFS measurement system, *Journal of Synchrotron Radiation*, 8 (2001) 168-172.
- [23] Y. Tanizawa, W.J. Chun, T. Shido, K. Asakura, Y. Iwasawa, Three-dimensional analysis of the local structure of Cu on TiO₂(110) by in situ polarization-dependent total-reflection fluorescence XAFS, *Journal of Synchrotron Radiation*, 8 (2001) 508-510.
- [24] Y. Tanizawa, T. Shido, W.J. Chun, K. Asakura, M. Nomura, Y. Iwasawa, Three-dimensional structure analyses of Cu species dispersed on TiO₂(110) surfaces studied by polarization-dependent total-reflection fluorescence X-ray absorption fine structure (PTRF-XAFS), *J. Phys. Chem. B*, 107 (2003) 12917-12929.
- [25] K. Fujikawa, S. Suzuki, Y. Koike, W.-J. Chun, K. Asakura, Self-regulated Ni cluster formation on the TiO₂(110) terrace studied using scanning tunneling microscopy, *Surface Science*, 600 (2006) 117-121.
- [26] Y. Koike, K. Ijima, W.J. Chun, H. Ashima, T. Yamamoto, K. Fujikawa, S. Suzuki, Y. Iwasawa, M. Nomura, K. Asakura, Structure of low coverage Ni atoms on the TiO₂(110) surface - Polarization dependent total-reflection fluorescence EXAFS study, *Chem. Phys. Lett.*, 421 (2006) 27-30.
- [27] Y. Koike, K. Fujikawa, S. Suzuki, W.J. Chun, K. Ijima, M. Nomura, Y. Iwasawa, K. Asakura, Origin of self-regulated cluster growth on the TiO₂(110) surface studied using polarization-dependent total reflection fluorescence XAFS, *J. Phys. Chem. C*, 112 (2008) 4667-4675.
- [28] S. Takakusagi, W.J. Chun, H. Uehara, K. Asakura, Y. Iwasawa, Polarization-Dependent Total-Reflection Fluorescence X-ray Absorption Fine Structure for 3D Structural Determination and Surface Fine Tuning, *Top. Catal.*, 56 (2013) 1477-1487.
- [29] E.A. Stern, Number of relevant independent points in x-ray-absorption fine-structure spectra, *Phys. Rev. B*, 48 (1993) 9825-9827.

Chapter 2

General experimental procedure

Over the last two decades, X-ray Absorption Fine Structure (XAFS) spectroscopy has emerged as an incisive probe of the local structure. Foremost among its strengths are its applicability to amorphous materials and its “tunability” - the ability to probe the environments of different elements in the sample by selecting the incident x-ray energy [4, 5]. It allows determining local structure with elemental sensitivity, the radial distribution of atoms around the selected central site, including bond lengths, coordination numbers, and thermal disorder, and certain information about the electronic structure of the central site, which may be inaccessible by any other technique. XAFS includes both Extended X-Ray Absorption Fine Structure (EXAFS) and X-ray Absorption Near Edge Structure (XANES). The sudden rise in absorption at the edge occurs when an incident x-ray photon has just sufficient energy to cause transition of an electron from the $1s$ state of some element in the sample to an unfilled state of predominantly p-character (i.e. angular momentum $l = 1$ with respect to the central absorbing atom). In the near edge region, XANES, transitions may occur to unfilled bound states, nearly-bound states (resonances), or continuum states of the appropriate symmetry. In the EXAFS region, well above the absorption edge (≥ 30 eV), transitions are to continuum states.

When charged particles, in particular electrons or positrons, are forced to move in a circular orbit, photons are emitted. At relativistic velocities (when the particles are moving at close to the speed of light) these photons are emitted in a narrow cone in the forward direction, at a tangent to the orbit. In a high energy electron or positron storage ring, these photons are emitted with energies ranging from infra-red to energetic (short wavelength) X-rays. This radiation is called “Synchrotron Radiation”. Synchrotron radiation is notable for its:

- High brightness and high intensity, many orders of magnitude more than with X-rays produced in conventional X-ray tubes
- Highly polarized
- High collimation, i.e. small angular divergence of the beam
- Wide energy spectrum: synchrotron radiation is emitted with a wide range of energies, allowing a beam of any energy to be produced.

- High brilliance, exceeding other natural and artificial light sources by many orders of magnitude.
- Pulsed light emission (pulse durations at or below one nanosecond, or a billionth of a second).

These notable characteristics of synchrotron radiation make the XAFS more practicable.

Structural information such as local structure with elemental sensitivity, the radial distribution of atoms around the selected central site, including bond lengths, coordination numbers, and thermal disorder, and certain information about the electronic structure of the central site were determined by X-ray Absorption Fine Structure (XAFS) spectroscopy which includes both Extended X-Ray Absorption Fine Structure (EXAFS) and X-ray Absorption Near Edge Structure (XANES). XANES and EXAFS of the samples were performed in the transmission or fluorescence mode at various synchrotron facilities as described in detail by each chapter.

2.1. Common detector used in the XAFS

Photon, that is, X-rays, may be treated either as electromagnetic waves or as particles. Photons are detected by means of the electrons they produce when they interact in the material of the detector is made. The main interactions are photoelectric effect and Compton scattering. The electrons produced by these interactions deposit their energy in the detector and thus generate a voltage pulse that signifies the passage of the photon. The height of the voltage pulse is proportional to the energy deposited in the detector. The detectors used in this thesis is described in the following section.

2.1.1. Ionization chamber

Ionization chamber is commonly used for detecting the energy of incident x-ray and that after pass through the sample in transmission mode. Ionization chamber is a kind of gas-filled detector. Gas-filled detectors operate by utilizing the ionization produced by radiation as it passes through a gas. It typically consists of two electrodes to which a certain electrical potential is applied. The space between the electrodes is filled with a gas. Ionization radiation, passing

through the space between the electrodes, deposits part or all of its energy by generating electron-ion pairs. Both electrons and ions are charge carriers that move under the influence of the electric field. Their motion induces a current on the electrodes, which may be measured. Or, through appropriate electronics, the charge produced by the radiation may be transformed into a pulse, in which case particles are counted individually. The general schematic diagram is shown in figure 2.1 [6]. Ionization chamber operates in a region where increasing of applied voltage does not produce a greater number of ions collected per unit time. That said, the charge collected stays constant despite a change in the voltage because the recombination rate is zero and no new charge is produced. The output signal is proportional to the particle energy deposited in the detector. Therefore, measurement of particle energy is possible. The voltage applied is less than 1000

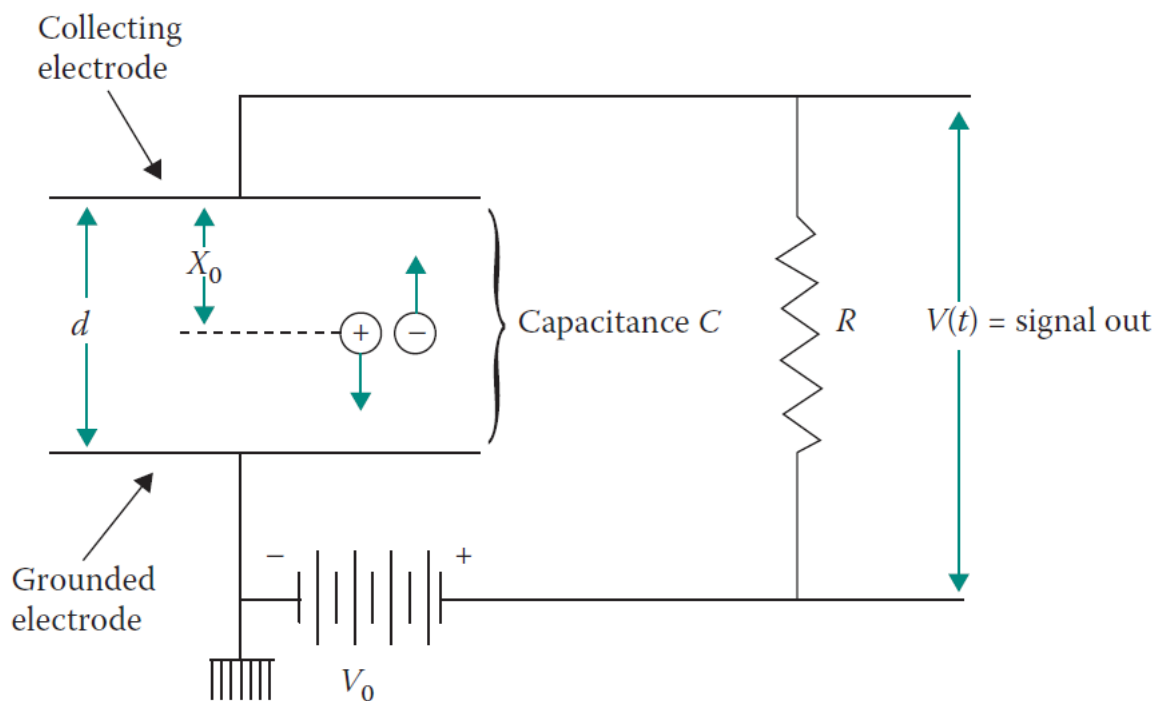


Figure 2.1 The electronic circuit of a parallel-plate ionization chamber.

V. Ionization chamber is simple, reliable, exhibit good linearity, and can handle high count rates.

2.1.2. Ge detector

In the fluorescence detection mode, we are only interested in photons of a few specific energies. They are the ones that correspond to fluorescence from the atom the edge of which we are measuring. Other x-rays, such as those scattered from the sample, constitute undesirable background. Energy-discriminating detectors solve this problem by counting only photons within a chosen energy range. The common energy-discriminating detector is a multi-element detector using germanium. This detector uses hyperpure germanium that permanently house inside the cooling medium such as liquid nitrogen. The common designs are shown in figure 2.2 [6]. The Ge detector is a kind of semiconductor detectors. Semiconductors are solid-state devices that operate essentially like ionization chambers. The charge carriers in semiconductors are not electrons and ions, as in the gas-filled detector, but electrons and holes. The most important advantage of semiconductor detectors, compared to other types of radiation detectors, is their

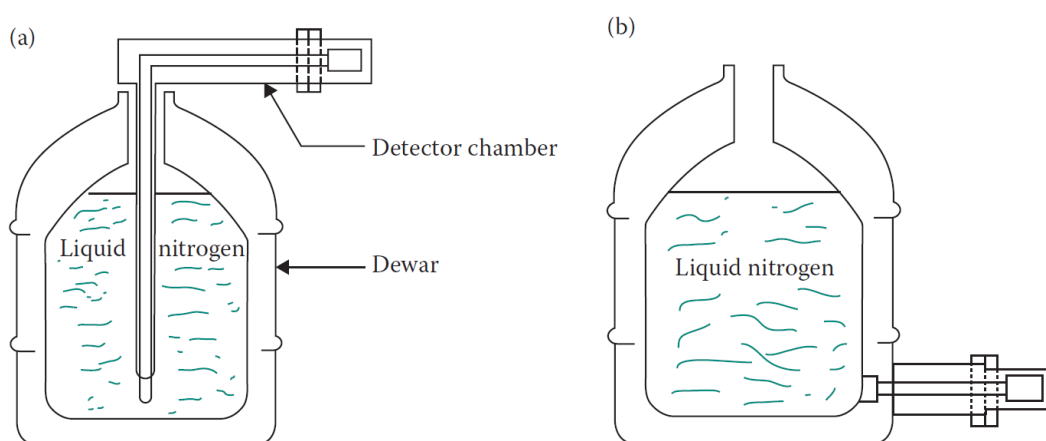


Figure 2.2 (a) A dipstick cryostat (cross section), (b) an integral cryostat (cross section).

superior energy resolution: the ability to resolve the energy of particles out of a polyenergetic energy spectrum.

2.1.3. Photon counting pixel detector

Detector is also an important piece in the experiment. It must have several important characteristics. One of important characteristic is linear response which indicates a straight-line transfer function of the detector. Nonlinearity detector affects the obtained results and may leading to the misinterpretation. The first set of published articles of MARPE suffer from the nonlinearity response of the detector being used [7, 8] but was corrected in later publication [9, 10]. Because the proposed phenomena involve the energy transfer between the atom, one would expect very low probability for the event to occur. Thus, using detector with minute noise or no noise at all is very important because of low signal. MEDIPIX3 is a good candidate detector for our proposal [1, 11, 12]. MEDIPIX3 is a photon counting and tracking pixel detectors developed by an international

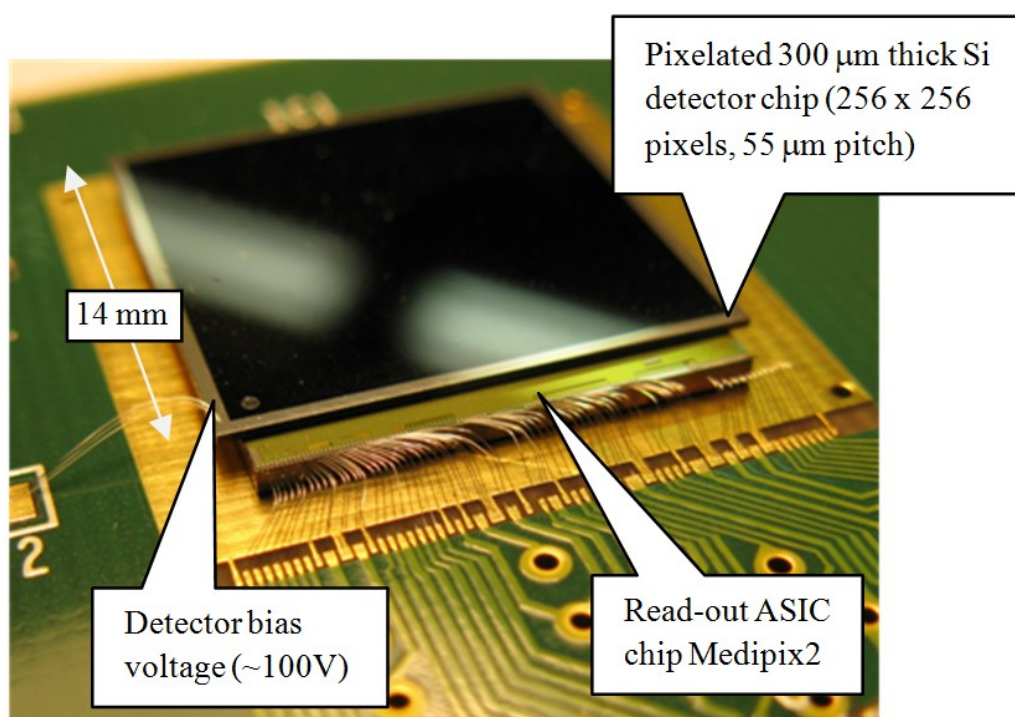


Figure 2.3 Single Medipix 2 assembly mounted and wire-bonded on a carrier board [3].

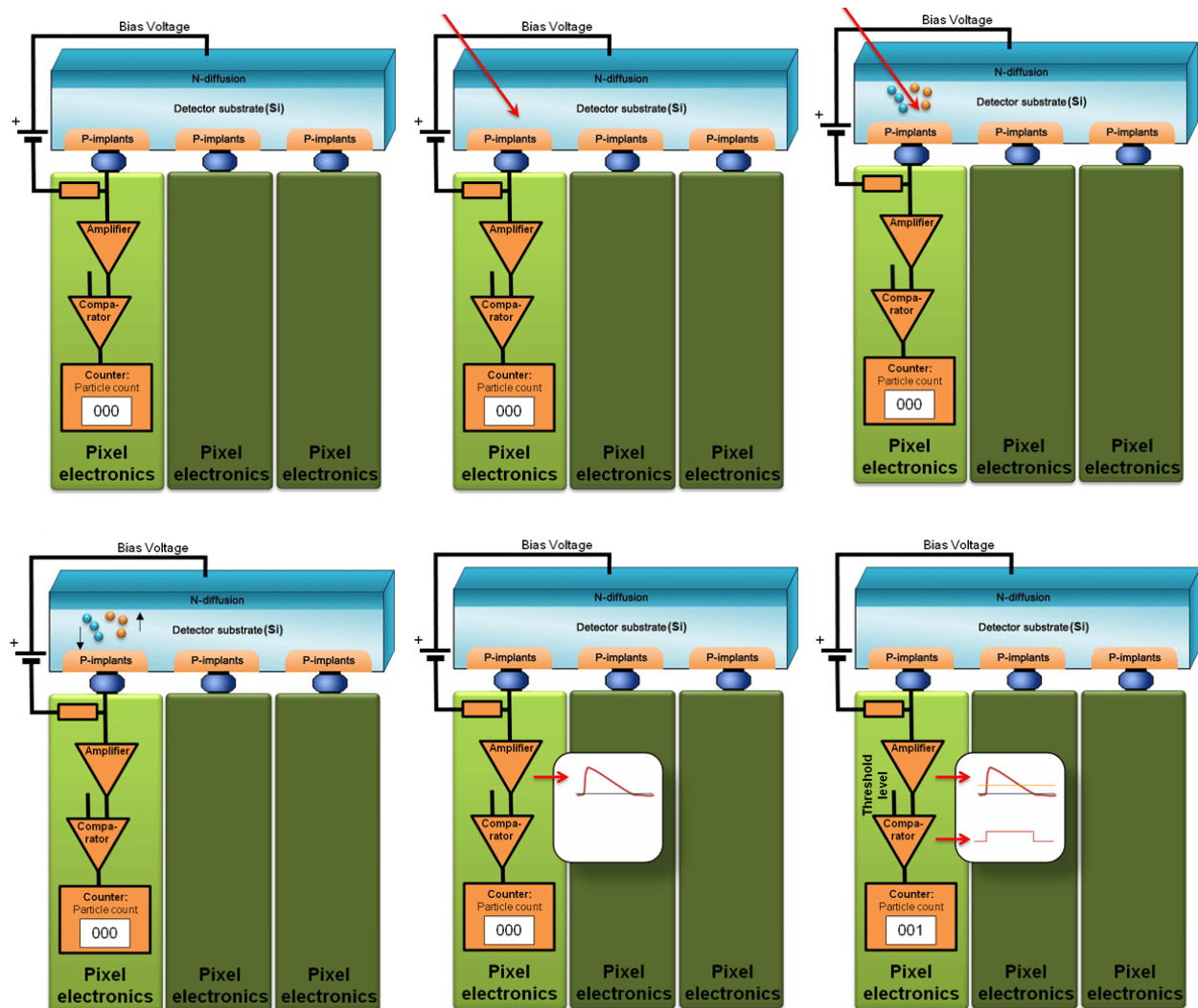


Figure 2.4 Principle of the phonon counting in a single pixel [2]. (From left to right, from top to bottom) The radiation generates electron-hole pairs (charge) in the sensor. The charge is collected to the appropriate pixel, amplified and compared with a pre-set comparator level (energy threshold). The counter is increased if the detected pulse is above the energy level.

consortium including CERN, DESY, DESY, ESRF and Diamond. It is a pixel array hybrid photon-counting detector consist of a monolithic semiconductor with a photodiode array configuration which is bump-bonded to CMOS base application-specific readout chips (ASICs). The general Medipix assembly is shown in figure 2.3. The principle of the photon counting in a single pixel has been illustrated below in figure 2.4. When the photon beam impinges on the detector, electron-hole pairs are generated. Under the influence of electric field

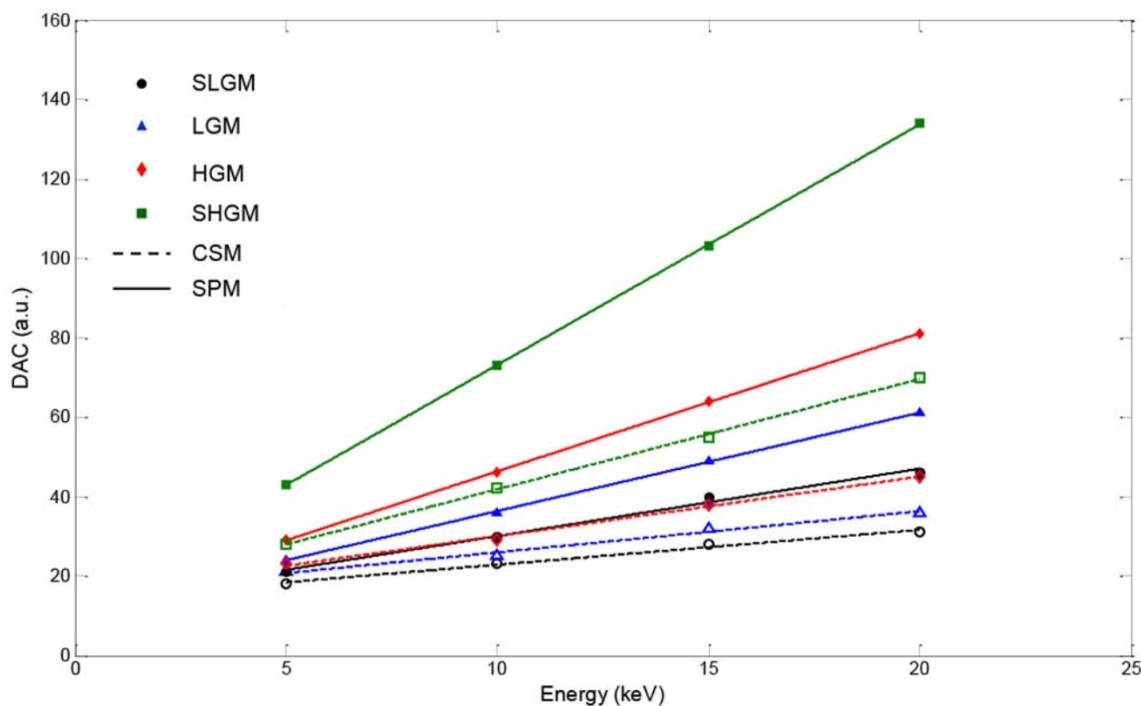


Figure 2.5 Linearity response (markers) and fits (lines) of the detector at different energies for Single Pixel Mode (solid line) and Charge Summing Mode (dash lines) for each of the four gains [1].

generated from applying bias voltage, both electrons and holes will move in opposite direction because of the difference of their charges. The charges are collected at the pixel electrodes which is bump-bonded to a CMOS electronic layer, pass through an amplifier and a shaper. Then, the signal is compared with a pre-set level which is set by energy threshold. Number of counts is increased if the detected signal is above the energy level. Therefore, no noise and no dark current are achieved. MEDIPIX3 offers zero dead time between frames, no external cooling system required, spectroscopic imaging and compact size. In addition, Excellence linear response is obtained for the photon energy in the range of 5 to 20 keV as shown in figure 2.5. Typical Medipix3 contains 256 X 256 pixels array of 55 μm X 55 μm pitch each, forming a total area 14.08 mm X 14.08 mm. Medipix3 can be increased its total area by bump-bonding multiple chips to larger monolithic sensors. Detector used in the experiment are 2 X 2 chips forming 512 X 512 pixels array or 262,144 pixels. Because every individual impinged photon is analyzed by the electronic circuits in each pixel, therefore the

detector could be considered as 262,144 individual counting detectors or even spectrometers.

2.2. XAFS data processing

There are several data processing steps that are needed to refine the final spectrum for analysis [4, 13-17]. These preprocessing procedures include removal of data points that are clearly in error (deglitching), changing the energy scale to align several scans, and averaging several scans to produce a high quality spectrum for analysis.

2.3. EXAFS data analysis

1. Convert measured intensities to $\mu(E)$.

Starting with measured intensities before and after the sample, we construct $\mu(E)$ by using following equation:

For transmission XAFS,

$$I = I_0 e^{-\mu(E)t}$$

$$\mu(E)t = \ln\left(\frac{I_0}{I}\right)$$

For fluorescence XAFS,

$$\mu(E)t = \left(\frac{I_f}{I_0}\right)$$

2. Subtract a pre-edge background.

We subtract away the background that fits the pre-edge region. This gets rid of the absorption due to other edges.

3. Scale $\mu(E)$ to go from 0 to 1 or normalization.

One estimates the edge step, $\Delta\mu_0(E_0)$ by extrapolating a simple fit to the above $\mu(E)$ to the edge. One normalizes by this value to get the absorption from 1 x-ray.

$$\chi(E) = \frac{\mu(E) - \mu_0(E)}{\Delta\mu_0(E_0)}$$

4. Remove a post-edge smooth background function $\mu_0(E)$ to isolate the XAFS, χ .

We don't have a measurement of $\mu_0(E)$ (the absorption coefficient without neighboring atoms). We approximate $\mu_0(E)$ by an adjustable, smooth function: a spline. Then, fit a smooth polynomial spline to the XAFS to remove the slowly varying (low-frequency) components of $\mu(E)$.

5. Identify the threshold energy E_0 and convert from E to k space.

$$k = \sqrt{\frac{2m(E - E_0)}{\hbar^2}}$$

6. Weight XAFS.

The raw EXAFS (k) usually decays quickly with k , and difficult to assess or interpret by itself. Therefore, we multiply the XAFS to weight the higher- k portion of the spectra by k^2 or k^3 .

7. Fourier transform from k to R space.

$\chi(k)$ is composed of sine waves, so we'll Fourier Transform from k to R -space. To avoid ringing, we'll multiply by a smoothing window function to eliminate ripple from truncation of $\chi(k)$.

8. Model $f(k)$ and $\delta(k)$ and analyse $\chi(k)$ to get distances R , and coordination number N .

To model the EXAFS, we use the EXAFS Equation:

$$\chi(k) = S_0^2 \sum_i N_i \frac{f_i(k)}{kD_i^2} e^{-\frac{2D_i}{\lambda(k)}} e^{-2k^2\sigma_i^2} \sin(2kD_i + \delta_i(k))$$

where $f(k)$ and $\delta(k)$ are photoelectron backscattering and phase shift of the neighboring atom. (The sum is over "shells" of similar neighboring atoms). If we know these properties, we can determine:

D – distance to neighboring atom.

N – coordination number of neighboring atoms.

σ^2 – mean-square disorder of neighbor distance.

All procedures are performed with use of the computer software package named REX2000 [18] and FEFF [19-21]. REX2000 and FEFF used in this work is version 2.6.0 and 8.40, respectively, running on windows 10 operating system.

References

- [1] E.N. Gimenez, R. Ballabriga, G. Blaj, M. Campbell, I. Dolbnya, E. Frodjh, I. Horswell, X. Llopart, J. Marchal, J. McGrath, D. Omar, R. Plackett, K. Sawhney, N. Tartoni, Medipix3RX: Characterizing the Medipix3 Redesign With Synchrotron Radiation, *IEEE Transactions on Nuclear Science*, 62 (2015) 1413-1421.
- [2] IEAP-CTU, Principle of the phonon counting in a single pixel, 2007.
- [3] IEAP-CTU, Single Medipix 2 assembly mounted and wire-bonded on a carrier board., 2007.
- [4] J.J. Rehr, R.C. Albers, Theoretical approaches to x-ray absorption fine structure, *Rev. Mod. Phys.*, 72 (2000) 621-654.
- [5] Y. Iwasawa, K. Asakura, M. Tada, *XAFS Techniques for Catalysts, Nanomaterials, and Surfaces*, Springer International Publishing, Cham, 2017.
- [6] N. Tsoulfanidis, *Measurement and detection of radiation*, CRC press, 2010.
- [7] A. Kay, E. Arenholz, S. Mun, F.J. Garcia de Abajo, C.S. Fadley, R. Denecke, Z. Hussain, M.A. Van Hove, Multi-atom resonant photoemission: A method for determining near-neighbor atomic identities and bonding, *Science*, 281 (1998) 679-683.
- [8] A.W. Kay, E. Arenholz, B.S. Mun, J.G. de Abajo, C.S. Fadley, R. Denecke, Z. Hussain, M.A. Van Hove, Multiple atom resonant photoemission: A new technique for studying near-neighbor atomic identities and bonding, *J Electron Spectrosc Relat Phenom*, 101 (1999) 647-652.
- [9] A.W. Kay, F.J.G. de Abajo, S.H. Yang, E. Arenholz, B.S. Mun, N. Mannella, Z. Hussain, M.A. Van Hove, C.S. Fadley, Multiatom resonant photoemission, *Phys. Rev. B*, 63 (2001) 115119.
- [10] A.W. Kay, F.J. Garcia de Abajo, S.H. Yang, E. Arenholz, B.S. Mun, N. Mannella, Z. Hussain, M.A. Van Hove, C.S. Fadley, Multi-atom resonant photoemission, *J Electron Spectrosc Relat Phenom*, 114-116 (2001) 1179-1189.
- [11] R. Ballabriga, J. Alozy, G. Blaj, M. Campbell, M. Fiederle, E. Frojdj, E.H.M. Heijne, X. Llopart, M. Pichotka, S. Procz, L. Tlustos, W. Wong, The Medipix3RX: a high resolution, zero dead-time pixel detector readout chip allowing spectroscopic imaging, *Journal of Instrumentation*, 8 (2013) C02016.
- [12] E.N. Gimenez, R. Ballabriga, M. Campbell, I. Horswell, X. Llopart, J. Marchal, K.J.S. Sawhney, N. Tartoni, D. Turecek, Characterization of Medipix3

With Synchrotron Radiation, IEEE Transactions on Nuclear Science, 58 (2011) 323-332.

[13] M. Newville, Fundamentals of XAFS, University of Chicago, Chicago, IL, 2004.

[14] S. Calvin, XAFS for Everyone, CRC press, 2013.

[15] G. Bunker, Introduction to XAFS: a practical guide to X-ray absorption fine structure spectroscopy, Cambridge University Press, 2010.

[16] D. Koningsberger, R. Prins, X-ray absorption: principles, applications, techniques of EXAFS, SEXAFS, and XANES, (1988).

[17] Y. Iwasawa, X-ray absorption fine structure for catalysts and surfaces, World Scientific, 1996.

[18] T. Taguchi, REX2000 Version 2.5: Improved DATA Handling and Enhanced User-Interface, AIP Conference Proceedings, 882 (2007) 162-164.

[19] A.L. Ankudinov, B. Ravel, J.J. Rehr, S.D. Conradson, Real-space multiple-scattering calculation and interpretation of x-ray-absorption near-edge structure, Phys. Rev. B, 58 (1998) 7565-7576.

[20] A.L. Ankudinov, C.E. Bouldin, J.J. Rehr, J. Sims, H. Hung, Parallel calculation of electron multiple scattering using Lanczos algorithms, Phys. Rev. B, 65 (2002) 104107.

[21] A.L. Ankudinov, A.I. Nesvizhskii, J.J. Rehr, Dynamic screening effects in x-ray absorption spectra, Phys. Rev. B, 67 (2003) 115120.

Chapter 3

A New Indicator for Single Metal Dispersion on a TiO₂(110) Surface Premodified with a Mercapto Compound

3.1. Introduction

Supported metal catalysts have drawn much attention for their wide applications such as catalysts, sensors, electronic and magnetic devices. It is very important to control the structure and electronic state of the supported metal, including the metal cluster size, to obtain the best performance for a particular application. It has been known that the catalytic activity depends on metal cluster size, its structure and the interfacial interaction with the support. Therefore, the structures of metal clusters and their metal-substrate interactions must be precisely determined to understand growth mechanism and hence the distinctive catalytic activity.

Metal oxides are widely used as substrates for preparing highly dispersed metal clusters with their size less than a few nm. TiO₂ is well known oxide support for metal catalysts because of its properties and stability. Its atomic scale structure is extensively studied by various techniques, especially surface science techniques, such as ab initio calculation, X-ray diffraction spectroscopy (XRD), low-energy electron diffraction (LEED), medium-energy electron diffraction (MEED), X-ray photoelectron spectroscopy (XPS), scanning tunneling microscopy (STM), atomic force microscopy (AFM) [5]. TiO₂(110) (1 X 1) surface structure has an isotropic structure as shown in Figure 3.1 (a). There are protruding oxygen atoms called “bridging oxygen atom” running along [001] direction. The troughs between bridging oxygen rows are the places where 5-fold Ti and in-plane oxygen atoms situated. One interesting feature of TiO₂(110) surface is the feature so called “self-limiting growth mode” when deposited with late transition metals such as Ni, Cu, Pd, Au. This feature is very important for preparing well-defined nanocluster for various application.

As has been mentioned previously that the catalytic activity depends on the structure of active species, it would help us gain the optimal performance for the interested application if we are able to synthesize them with atomic-level precision. The ability to manipulate with atomic-level precision is currently an emerging technology to enhance the selectivity and efficiency for one interested application and is so called precision catalysis. Precision catalysis requires a synthesis with atomic-level precision because a difference of only one atom might cause significant change in their reactivities and properties. Thus, the understanding of metal-TiO₂ (110) interaction is the key to archive highly dispersed and fine controlled manipulation of the active species on the support.

To archive highly dispersed supported metal catalyst, the metal species should not be mobilized freely on the support surface causing aggregation. The immobilization of metal species could be achieved when the binding of metal species to the support surface is strong. The widely used method to get such the desired effect is by grafting a metal complex or by the anchoring of a metal species through a linker molecule. Grafting metal complex is done by deposit the organometallic compound onto oxide surface through the reaction between reactive functional group and OH species of the support surface. Then, the immobilized metal complex is appropriately treated to convert to an active metal structure or ready to use if it is already an active structure [6]. Grafting methods generally need the synthesis of organometallic compounds with the desired

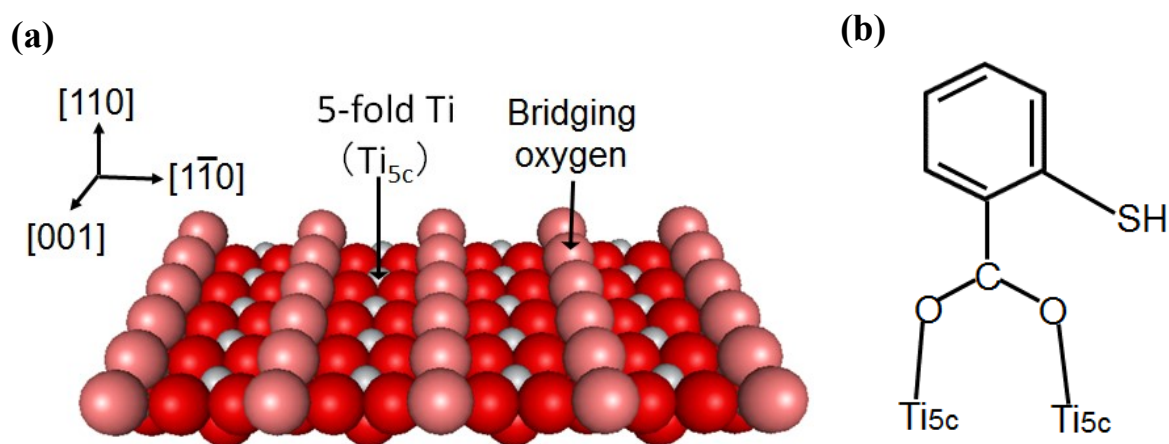


Figure 3.1 (a) Structural model of the TiO₂(110) surface. (b) Chemical structure of *o*-MBA absorbed on TiO₂(110) [1-3]. Ti_{5c} indicates a fivefold coordinated Ti atom on the TiO₂(110) surface.

structure. These compounds, in general, are often decomposed in air or at high temperature. The highly dispersed supported metal catalyst could be obtained without the need of organometallic compounds, nevertheless, through premodified surface method. In this premodified surface method, the surface of oxide support is premodified with an organic compound which strongly binds to a metal atom. This method has benefit that there is an enormous number of organic compound available to suit for pre-modification purposes and selective fine tuning of the surface metal structure. Recently, atomic dispersed metals on metal oxide substrate are also obtained by a premodified surface method [7-10].

To investigate the metal-metal oxide interaction, a well-defined single crystal metal oxide is needed as a model substrate because conventional powder support materials have ill-defined surfaces, hence three-dimensional structural analysis is not applicable. In addition, an analysis method capable of providing three-dimensional structural information of the surface species is essential. XAFS (X-ray absorption fine structure) is a technique providing information of the local structure of the X-ray absorbing atom. The XAFS technique has widely been used to obtain the local structure information of metal particles dispersed on metal oxide powder. However, the metal-oxide interface structures derived from conventional XAFS are indecisive. Polarization-dependent X-ray absorption fine structure (PTRF-XAFS) analysis can uniquely provide three-dimensional structural information around highly dispersed metal species on single crystal surface [11-23].

In this study, $\text{TiO}_2(110)$ surface is premodified with ortho-mercaptobenzoic acid (o-MBA) which its structure is shown in figure 3.1 (b). The o-MBA was previously used in the preparation of the atomically dispersed of Cu on $\text{TiO}_2(110)$ [10]. The premodified surface $\text{TiO}_2(110)$ with o-MBA is subsequently deposited with the group 10 metals Ni, and Pt, both of which are the important catalysts. Pt has been widely used in industrial catalysis such as automobile, petrochemical, fuel cell catalysts. The structures of Ni and Pt deposited on premodified surface $\text{TiO}_2(110)$ are studied using PTRF-EAXFS.

3.2. Titanium Dioxide or TiO_2

3.2.1. Structural properties of TiO_2

Titanium dioxide has been widely used as a pigment [24], in sunscreens [25, 26], paints [27], ointments, toothpaste, etc. In 1972, Fujishima and Honda discovered the photocatalytic splitting of water on TiO₂ electrode under ultraviolet (UV) light [28, 29]. Since then, many research efforts have been devoted to the researches on TiO₂ material which have led to many promising applications in area ranging from photovoltaics and photocatalysis to photo/electrochromics and sensors. Nowadays, titanium dioxide is the most well-known and studied photocatalyst. Table 3.1 shows three major polymorphs of titanium dioxide.

Table 3.1 Important polymorph of titanium dioxide [30]

Polymorph	Crystal System	Lattice constants (Å)	Space Group	Density (g/cm³)
Anatase	Tetragonal	$a=3.784$ $c=9.515$	I4 ₁ /amd	3.79
Brookite	Orthorhombic	$a=9.184$ $b=5.447$ $c=5.145$	Pbca	3.99
Rutile	Tetragonal	$a=4.5936$ $c=2.9587$	P4 ₂ /mnm	4.13

Figure 3.2 shows the basic unit cell structure of anatase and rutile phase of TiO₂. Rutile has 6 atoms per unit cell but, in the case of anatase, it has 12 atoms per unit cell – both which are tetragonal. In both polymorphs, each O²⁻ is coordinated to Ti⁴⁺ ions and each Ti⁴⁺ ion is octahedrally coordinated to 6 O²⁻ ions. These two crystal structures have been described frequently in terms of infinite columns of edge sharing TiO₆ octahedra. They differ in distortion and interconnections of octahedra. The distortion is greater in anatase than in rutile. The Ti-Ti distances in anatase are greater (3.79 and 3.04 Å in anatase vs. 3.57 and 2.96 Å in rutile) whereas the Ti-O distances are shorter than in rutile (1.934 and 1.980 Å in anatase vs. 1.949 and 1.980 Å in rutile). In the rutile structure each octahedron is in contact with 10 neighbor octahedrons (two sharing edge oxygen pairs and eight sharing corner oxygen atoms) while in the anatase structure each octahedron is in contact with eight neighbors (four sharing an edge and four

sharing a corner). The differences in crystal structure cause the difference in mass densities and electronic properties for anatase and rutile phase.

TiO₂ is an important oxide support for noble metal catalysts because of its stability and semiconducting properties [5]. TiO₂ is also an important support

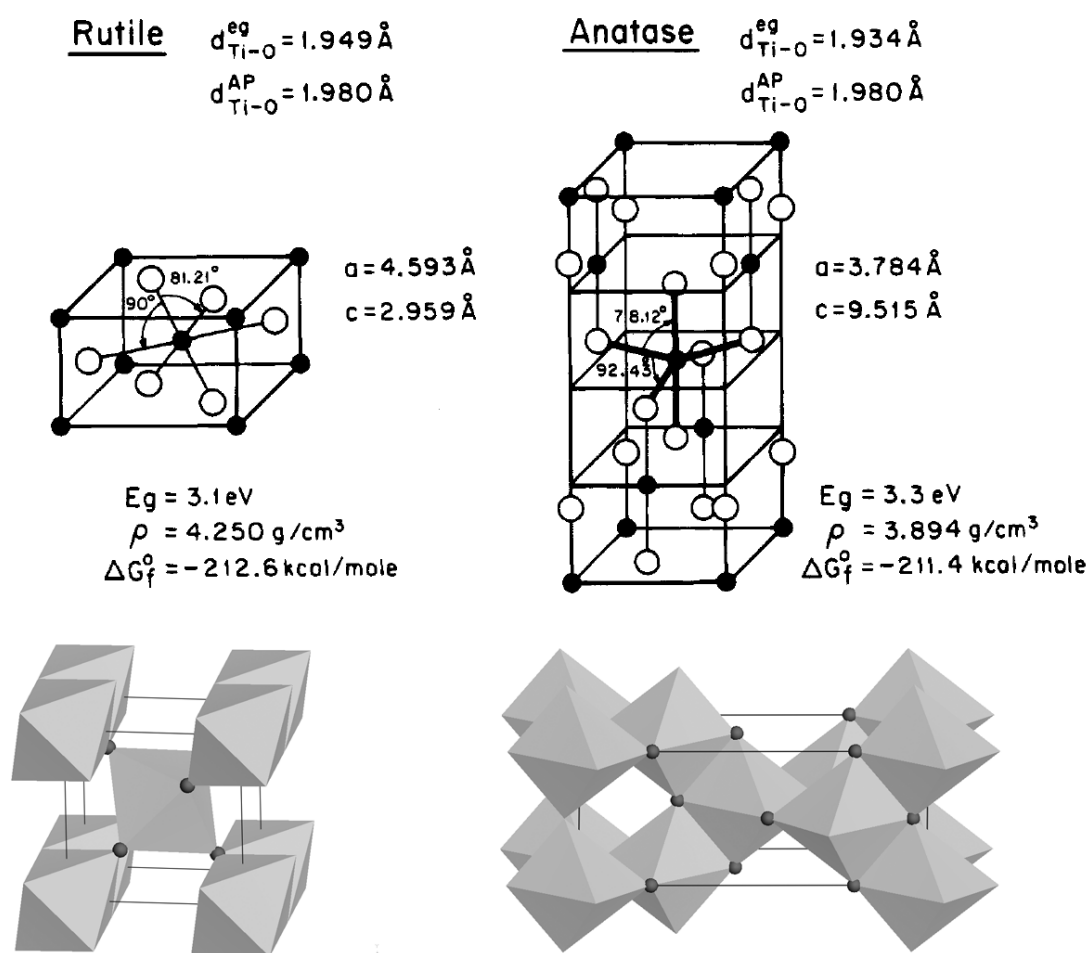


Figure 3.2 Structure of rutile and anatase TiO₂ [8], and corresponding octahedra

material for metal to prepare dispersed metal catalysts [7-10, 31, 32]. In particular, TiO₂(110) (1 X 1) surface is the most intensively studied TiO₂ surface.

3.2.2. Surface properties of TiO₂(110)

TiO₂(110) (1 X 1) surface structure has an isotropic structure as shown in Figure 1.2. There are protruding oxygen atoms called “bridging oxygen atom” running along [001] direction. The troughs between bridging oxygen rows are the places where 5-fold Ti and in-plane oxygen atoms situated. An interesting feature of late transition metals on the TiO₂(110) surface is a self-limiting growth mode. Self-limiting growth modes are often observed in film growths of compound semiconductors, quantum dots on Si, metal islands on the surfaces of metals, and so on. These processes are important when one wishes to prepare well-defined nanoclusters for electronic, optical, and magnetic devices and catalysts [33-42].

3.3. Experimental procedure

3.3.1. Sample preparation

TiO₂(110) substrate samples used in the experiment was optically polish 0.05% Nb-doped TiO₂(110) (20×20×1 mm³) which was purchased from Shinkosya Co., Japan. They were cleaned as has been reported previously in the literature [43, 44]. Briefly, TiO₂(110) substrate samples were immersed in a 10% HF solution for 10 minutes, then annealing in air at 700 °C for 1 hour. The difficulty of pre-modification of the TiO₂(110) surface with *o*-MBA vapor caused by low vapor pressure of *o*-MBA is overcome by a wet chemical process. The process is not complicate and can be used to employ many other functional organic compounds for surface modification of the support. The cleaned support surface was immersed in a 2 mM solution of *o*-MBA (Toronto Research Chemicals Inc., Canada) in ethanol for more than 24 h to modify the TiO₂(110) surface with an *o*-MBA monolayer. The substrate sample was then transferred to an ultra-high vacuum (UHV) PTRF-XAFS chamber. Ni was evaporated onto the *o*-MBA-modified TiO₂(110) surface via the resistive heating of a tungsten filament wrapped with Ni wire (99.999% purity, Nilaco Co., Japan). Pt was deposited by generating Pt vapor through the electron bombardment of a Pt rod (99.98% purity, Nilaco Co., Japan) by applying a high voltage (typically 800 V) between the filament and the Pt rod. The Ni and Pt coverages were estimated to be 0.27 ML and 0.11 ML (where 1 ML is defined as 5.2×10¹⁴/cm² based on the TiO₂(1×1) unit cell) from the X-ray photoelectron spectroscopy (XPS) Ni 2p_{3/2}-Ti 2p_{3/2} and Pt 4f_{7/2}-Ti 2p_{3/2} peak area ratios, respectively. The samples thus obtained are designated as Pt/*o*-MBA/TiO₂(110) and Ni/*o*-MBA/TiO₂(110) hereafter.

3.3.2. PTRF-XAFS

The PTRF-XAFS measurement system composes of three UHV chambers which are a sample preparation chamber, an PTRF-XAFS measurement chamber, and a mobile sample transfer chamber [18]. After deposition of Ni or Pt onto the $\text{TiO}_2(110)$ substrate samples, the samples were then transferred to PTRF-XAFS measurement chamber without exposure to air. The measurement chamber was equipped with a six-axis goniometer to adjust the total reflection conditions and sample orientations against the electric vector of the incident X-ray. PTRF-XAFS measurements were performed at the BL9A unit of the Photon Factory at the Institute of Materials Structure Science (KEK-IMSS-PF, Tsukuba, Japan) [45].

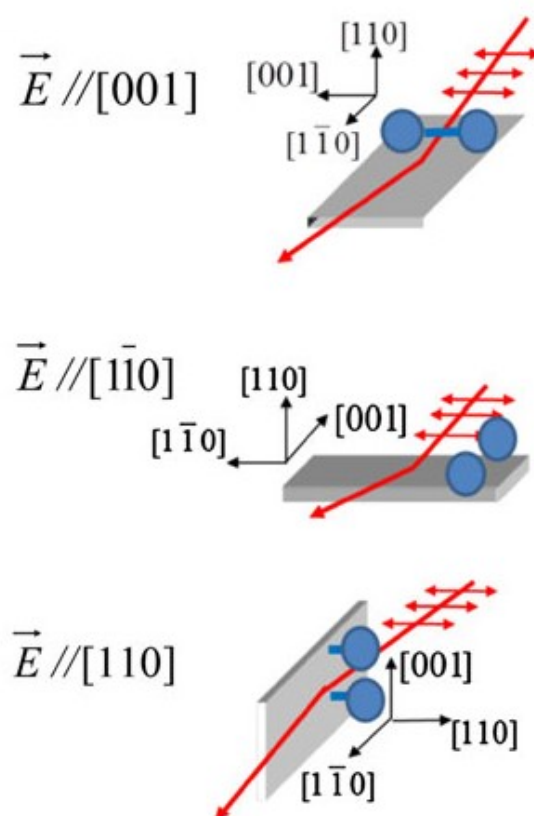


Figure 3.3 Three possible orientations for PTRF-XAFS measurements. Red arrows show the electric vector direction [4].

The storage ring energy and ring current were 2.5 GeV and 450 mA, respectively. The X-rays were monochromatized using a Si(111) double-crystal monochromator and were focused using a pair of bent conical mirrors. The energy of incident X-ray were analyzed by ionization chamber. Ni K α or Pt L α fluorescence signals were detected using a 19-element pure Ge solid-state detector (SSDGL0110S, Canberra, USA). The self-absorption effect is negligible in our case because the coverage was sufficiently small. Because the TiO₂(110) has an anisotropic surface structure, as shown in Figure 3.1 (a), PTRF-XAFS measurements were carried out in three orientations against the electric vector (\mathbf{E}) of the incident X-rays, i.e., two orientations parallel to the surface, $\mathbf{E} // [001]$, $[1\bar{1}0]$ and an orientation perpendicular to the surface; $\mathbf{E} // 110$. Figure 3.3 shows the three orientations performed in the measurement.

The EXAFS oscillations, $\chi(k)$, were extracted by using the program package Rex2000 version 2.6.0 (Rigaku Co., Japan) [46]. The background was estimated by the spline smoothing method with a Cook-Sayers criterion [47] and normalized by the edge height using a Victoreen equation. The polarization dependence of the overall XAFS oscillation value, $\chi_{\text{obs}}(k)$, is given by either eq. (1) or (2) [48].

$$\chi_{\text{obs}}(k) = 3 \sum_i \cos^2 \theta_i \cdot \chi_i(k) \text{ at Ni K-edge} \quad (1)$$

$$\chi_{\text{obs}}(k) = \sum_i (0.7 + 0.9 \cos^2 \theta_i) \cdot \chi_i(k) \text{ at Pt L}_3\text{-edge} \quad (2)$$

Here θ_i and $\chi_i(k)$ are the angle between the i -th bond direction and the electric vector of the X-rays and the partial XAFS oscillation accompanying the i -th bond, respectively. When the polarized x-ray with its electric vector perpendicular to the surface of a single crystal is used, the information selectively toward the interface direction is provided. On the other hand, when the polarized X-ray with its electric vector parallel to the surface, it will provide the in-plane information selectively. The preliminary analysis was carried out applying a least-squares curve fitting method, as summarized in eq. 3 and 4.

$$\chi(k) = \sum_i \frac{S_i N_i F_i(k_i) e^{-2k_i^2 \sigma_i^2} \sin(2k_i r_i + \varphi_i(k_i))}{k_i r_i^2} \quad (3)$$

$$k_i = \sqrt{k^2 - 2m\Delta E_i/\hbar^2} \quad (4)$$

Here S_i , N_i^* , σ_i , r_i , and ΔE_i are the inelastic reduction factor, effective coordination number, Debye-Waller factor, bond distance, and energy shift in the origin of the photoelectron kinetic energy of the i -th bond, respectively. The backscattering amplitude, $F_i(k_i)$, and phase shift, $\varphi_i(k_i)$, were calculated using the FEFF8.04 algorithm [49]. The inelastic reduction factors, S_i , were estimated using reference compounds and the same fitting parameters were employed within the same coordination shells. Three-dimensional structures were determined by an iterative method using the FEFF8.04 code [49] based on a real-space model structure. The goodness of fit between the observed XAFS oscillation values ($\chi_{obs}(k)$) and calculated values ($\chi_{cal}(k)$) was evaluated using eq. 5.

$$R' = \sqrt{\frac{1}{n_{data}} \sum_k \frac{(\chi_{obs}(k) - \chi_{cal}(k))^2}{\varepsilon(k)^2}} \quad (5)$$

The n_{data} is the number of data points. The $\varepsilon(k)$ is the error. The structure model was adopted when R' values lower than unity were obtained for all three orientations ($E//[001]$, $[1\bar{1}0]$, and $[110]$).

3.4. Results and discussion

3.4.1. Ni deposition on a TiO₂(110) surface premodified with *o*-MBA (Ni/*o*-MBA/TiO₂(110))

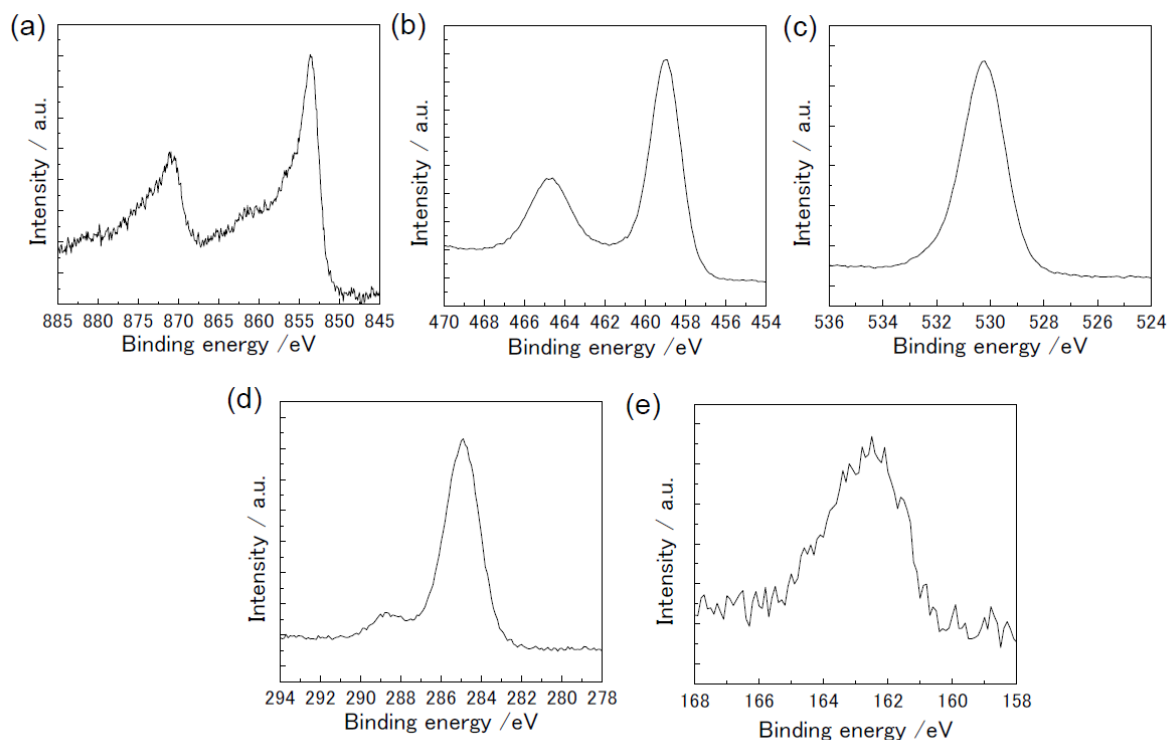


Figure 3.4 (a) Ni2p_{3/2}, (b) Ti2p, (c) O1s, (d) C1s and (d) S2p XPS spectra of Ni/*o*-MBA/TiO₂(110). The spectra were calibrated so that Ti2p_{3/2} peak appeared at 459.0 eV of the binding energy expected for bulk TiO₂.

Figure 3.4 shows the PTRF-EXAFS spectra of Ni/*o*-MBA/TiO₂(110) along with the spectra of some reference compounds. The spectra evidently show that PTRF-EXAFS oscillation envelopes of the sample are damped more very quickly in the higher *k* region compared to the Ni foil. It indicates that the nearest neighbor atom of X-ray absorbing atom is not Ni, but rather a light atom such as C, O, or S. Moreover, the amplitude of the EXAFS oscillation in the [001] and [1 $\bar{1}$ 0] directions were almost equal to each other but were both slightly lower than that in the [11] direction. A preliminary curve fitting analysis shows that Ni-S (0.219±0.003 nm) and Ni-O (0.185±0.003 nm) interactions were the major contribution in all three spectra. Contribution from Ni-Ni interactions was not

found which implies that there was no Ni aggregation. Ni-S bond length from the

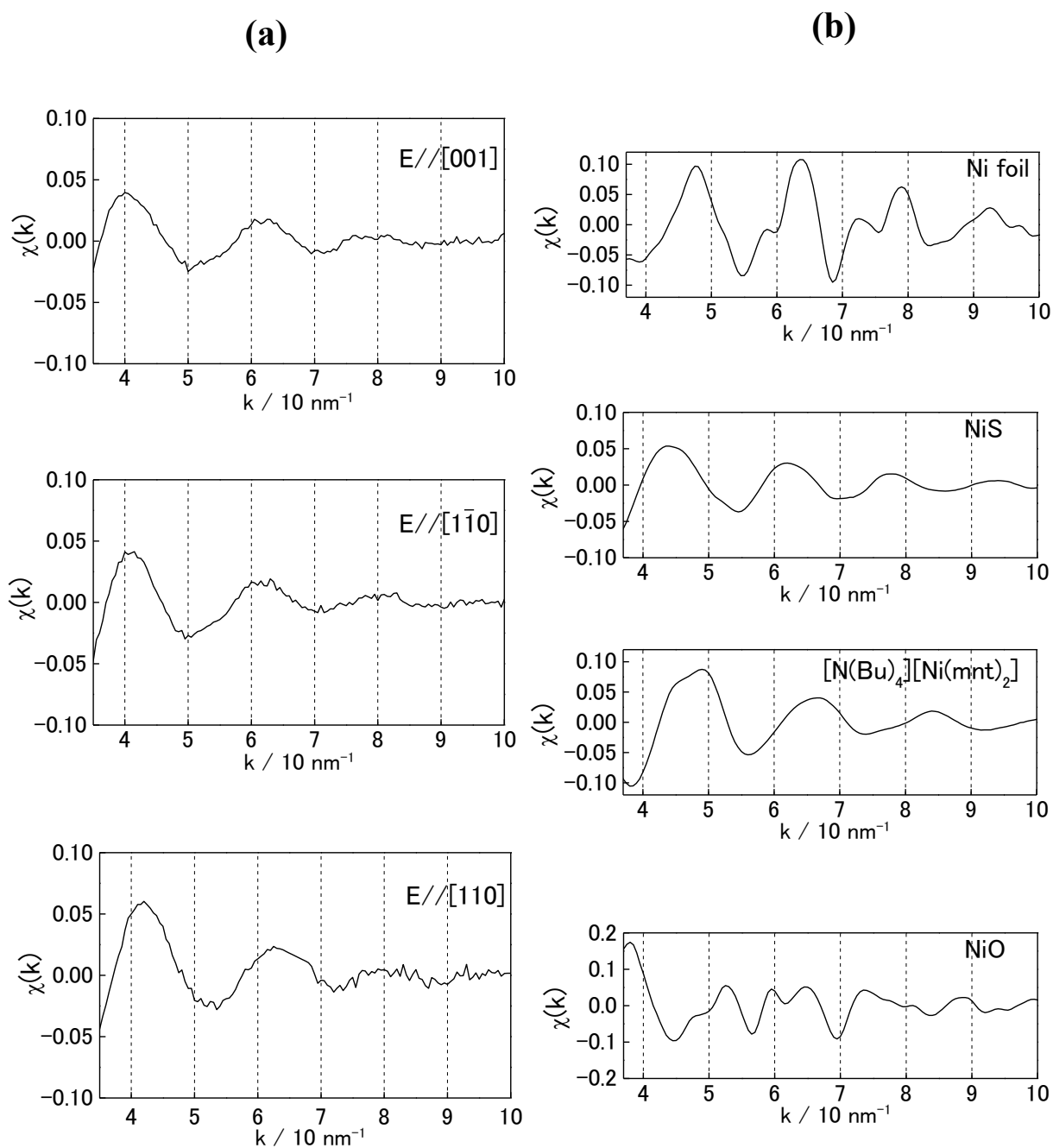


Figure 3.5. (a) Ni K-edge XAFS spectra of Ni/o-MBA/TiO₂(110) obtained at three different polarization directions. (b) Ni K-edge XAFS spectra of reference samples (Ni foil, nickel sulfide (NiS), tetrabutylammonium bis(maleonitriledi thiolato) nickel(III) ($[N(\text{Bu})_4][\text{Ni}(\text{mnt})_2]$), and nickel oxide (NiO)).

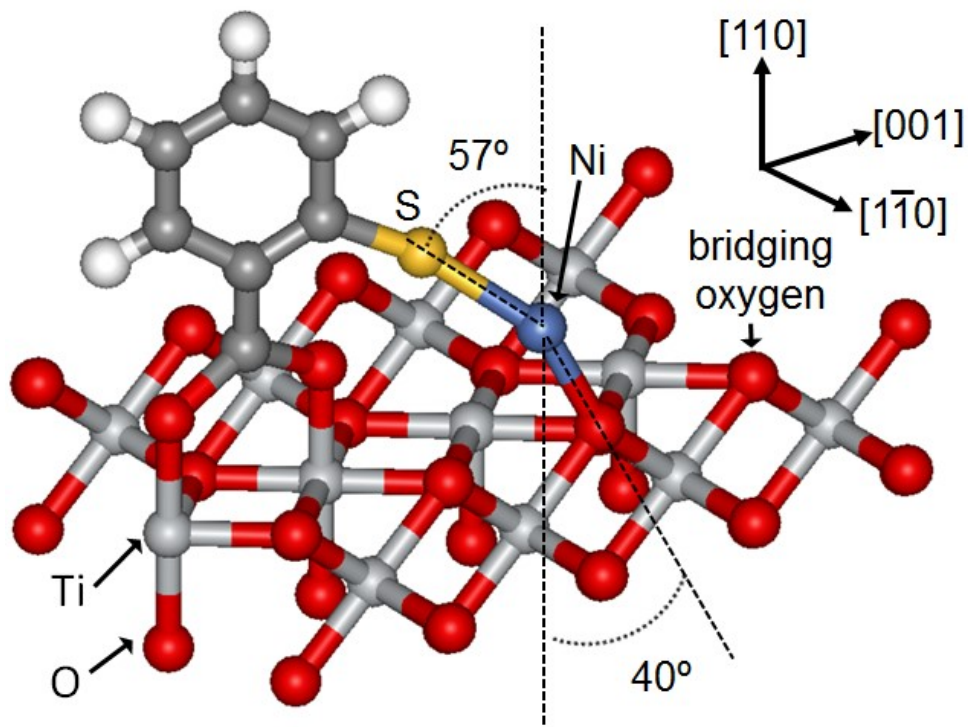


Figure 3.6 A model structure for the Ni/o-MBA/ TiO₂(110) surface.

preliminary analysis was comparable to or little shorter than those in [(N(Bu)₄)]Ni(mnt)₂ (0.214 nm) [50] and NiS (millerite, 0.226 and 0.238 nm).

FEFF code and a real-model structure were used to determine the three-dimensional structure of the Ni species. Figure 3.5 and 3.6 represent the proposed model structure and the polarization-dependent FEFF simulations overlaying with the experimental spectra, respectively. The EXAFS oscillations calculated based on the proposed model are almost resemble with the experimental spectra. The Ni-S bond length was 0.219 nm. The Ni-O interaction distance was 0.185 nm. The Ni-S bond angles relative to the surface normal was 57°. The Ni-O bond angles relative to the surface normal was 40°. The precision of FEFF simulations are found to be better than 3°. The S-Ni-O bond angle was estimated to be 156°.

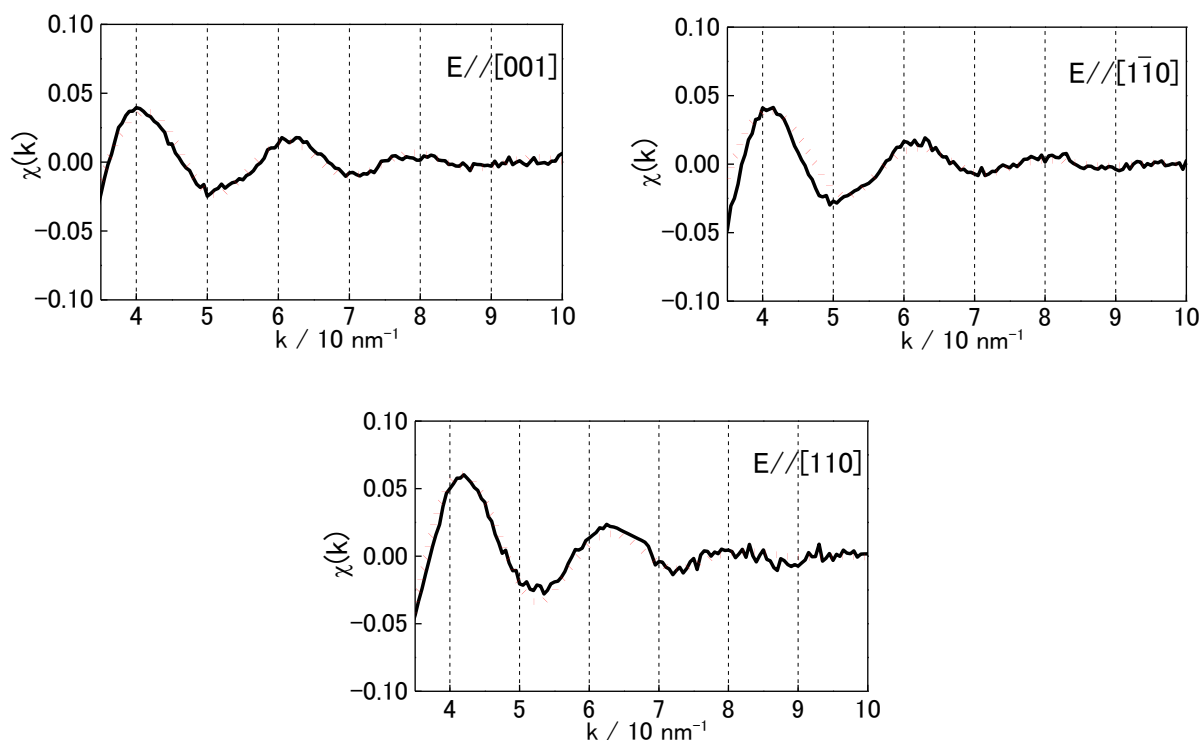


Figure 3.7 Comparison between the observed XAFS oscillations of the Ni/o-MBA/TiO₂(110) surface (black solid line) and those calculated based on the model structure in Figure 3.6 (red dotted line).

Figure 3.8 (a) and (b) shows the Ni K-edge XANES spectra of Ni/o-MBA/TiO₂(110) in three different polarization directions together with the spectra of some reference compounds. The oxidation state of Ni was estimated by the XANES results because the Ni2p_{3/2} XPS peak binding energies of Ni compounds are rather insensitive to formal oxidation state as has been reported previously in the literature [51]. Ni K-edge energies were determined as the first inflection point of the absorption edge for Ni foil, NiO and NiS and as the second inflection point for [N(Bu)₄][Ni(mnt)₂]. The XANES spectra were calibrated with the inflection point of Ni foil as 8331.7 eV. The K-edge energy is sensitive to oxidation state and to ligand to which the metal is bonded. For instance, a linear relation was found between the Ni K-edge energies and oxidation states in Ni oxy-compounds [52]. From the results in the report, it thus could be assumed a linear relation between oxidation states for each of the oxy- and the sulfur-containing compounds and the K-edge energies. The Ni K-edge energies for Ni/o-MBA/TiO₂(110) are found to be 8340.8 ± 0.1 eV in all polarization directions.

From the proposed model showing that the Ni bonds with one oxygen and one sulfur as shown in figure 3.6, the oxidation state then can be assigned to be +2 (see the dotted line in figure 3.8 (c)).

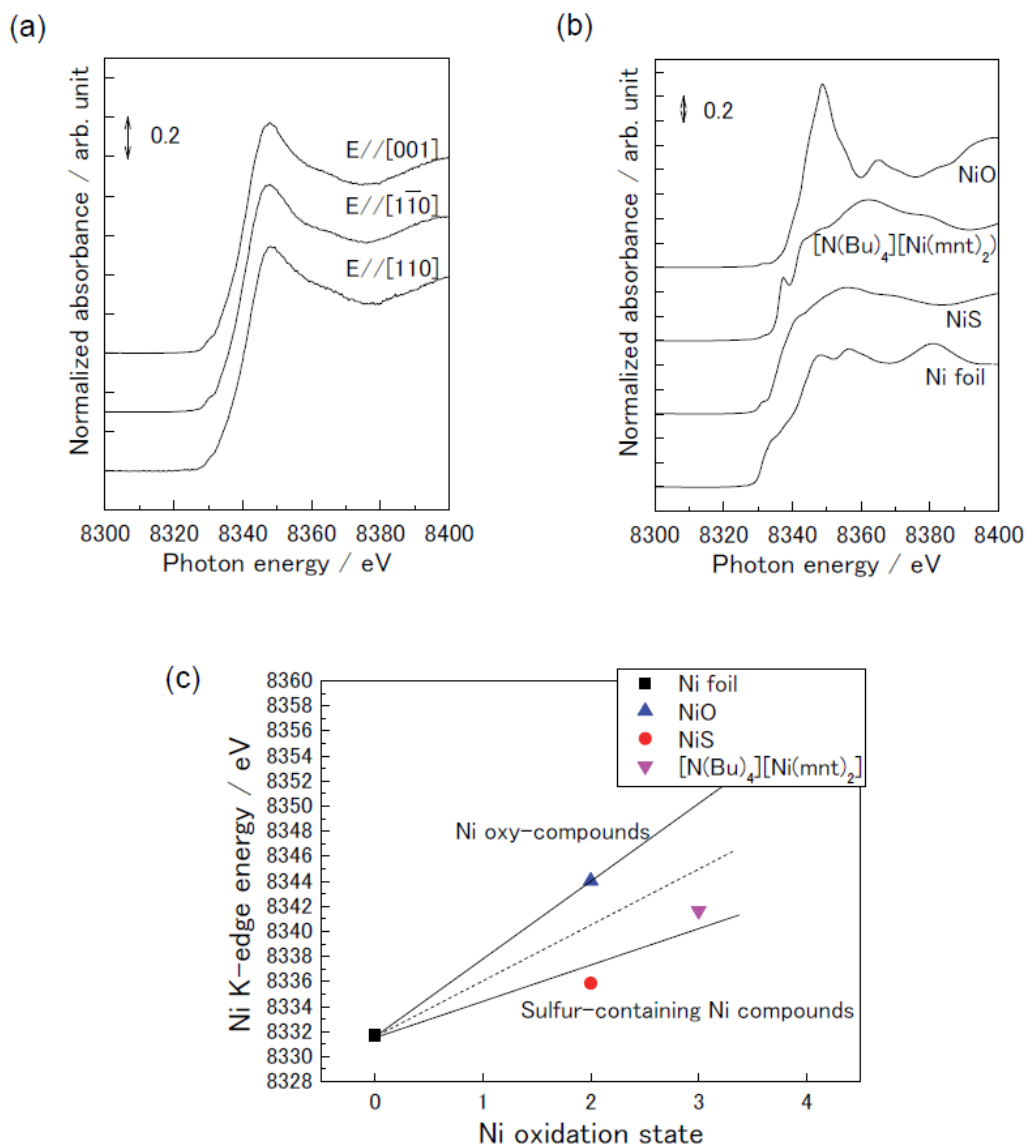


Figure 3.8 (a) Ni K-edge XANES spectra of Ni/o-MBA/TiO₂(110) in three different polarization directions. (b) Ni K-edge XANES spectra of reference compounds which are Ni metal (Ni foil), oxy-compound with Ni-O bonds (NiO) and sulfur-containing compounds with Ni-S bonds (NiS and $[N(Bu)_4][Ni(mnt)_2]$). (c) Plot of Ni K-edge energies for the reference compounds as a function of oxidation state. The dotted line shows the intermediate one between the lines corresponding to the oxy- and sulfur-containing compounds.

Previous studies of Ni deposited directly on a $\text{TiO}_2(110)$ surface have shown that atomically dispersed Ni is stabilized only at specific step edges ($\langle 1\bar{1}n \rangle$) through the formation of two Ni-O bonds (O-Ni-O), and that the Ni atoms are located at imaginary Ti sites when the Ni coverage is very low (~ 0.02 ML) [21]. Aggregation of Ni was also observed with the formation of clusters on the terrace surfaces when the coverage was increased above 0.05 ML [22, 53]. The stable Ni adsorption sites on the terrace surfaces could be atop bridging oxygens because these oxygen atoms have a dangling bond that points upward from the surface [54]. A single Ni-bridging oxygen bond is not sufficiently strong to fix the Ni atom at the atop site so that the Ni can hop to the next bridging oxygen atom and diffuse along the [001] direction. The Ni atoms eventually find other Ni atoms and form clusters before reaching the step edges if the Ni coverage is sufficiently high (> 0.05 ML). In the present study, I used a $\text{TiO}_2(110)$ surface with a very low step density (less than 4 lines every $1 \mu\text{m}^2$). The S atoms of *o*-MBA adsorbed on the $\text{TiO}_2(110)$ terrace surfaces were able to immediately immobilize the migrating Ni atoms in cooperation with the bridging oxygens, accompanied by rotation of the bond connecting the COO- moiety and the phenyl ring. The S-Ni-O bond angle was estimated to be 156° . Thus, Ni aggregation was effectively blocked on the surface even at a high Ni coverage (0.27 ML).

3.4.2. Pt deposition on a TiO₂(110) surface premodified with *o*-MBA (Pt/*o*-MBA/TiO₂(110))

Figure 3.9 shows XPS spectra of Pt/*o*-MBA/TiO₂(110). The spectra were calibrated so that Ti2p_{3/2} peak appeared at 459.0 eV of the binding energy expected for bulk TiO₂ [55]. S2p XPS spectrum confirms the presence of *o*-MBA on the TiO₂(110). The Ti2p and Pt4f XPS spectra were used to calculate the coverage of Pt on *o*-MBA/TiO₂(110) substrate as mention previously in

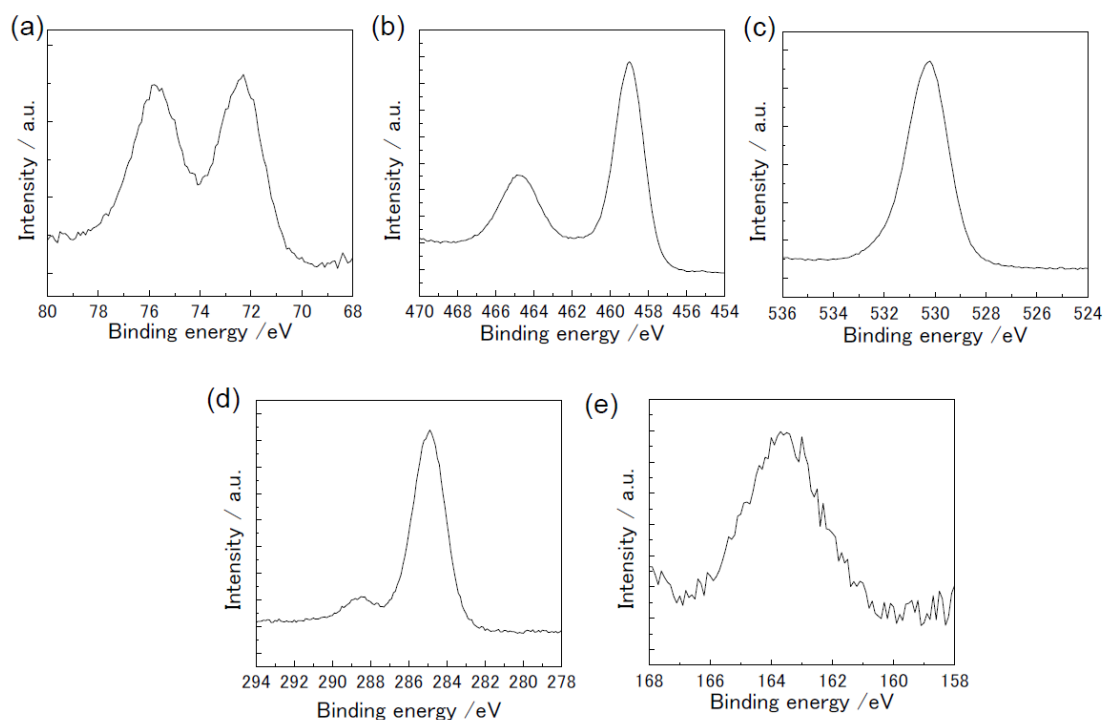


Figure 3.9 (a) Pt4f, (b) Ti2p, (c) O1s, (d) C1s and (e) S2p XPS spectra of Pt/*o*-MBA/TiO₂(110).

experimental section. Figures 3.10 (a) and (b) show the polarization -dependent EXAFS spectra obtained from Pt/*o*-MBA/TiO₂(110) as well as the spectra for reference compounds, respectively. Unlike Ni/*o*-MBA//TiO₂(110), Pt/*o*-MBA//TiO₂(110) does not show a significant degree of polarization dependence in the XAFS spectra in Figure 3.10 (a). Moreover, A preliminary curve fitting analysis shows the presence of Pt-S bonds (0.229 nm) and Pt-Pt bonds (0.267 nm) in all orientations, as shown in Table 3.2. The Pt-Pt bond distance was 0.01 nm

shorter than that in bulk Pt metal (0.277 nm), and it has been reported that the Pt-Pt bond distance is gradually shortened as the Pt particle size decreases [56]. Effective coordination number (N^*) of the Pt-Pt bond suggests the average Pt structure might be a trimer species. It is also possible that a mixture of atomically

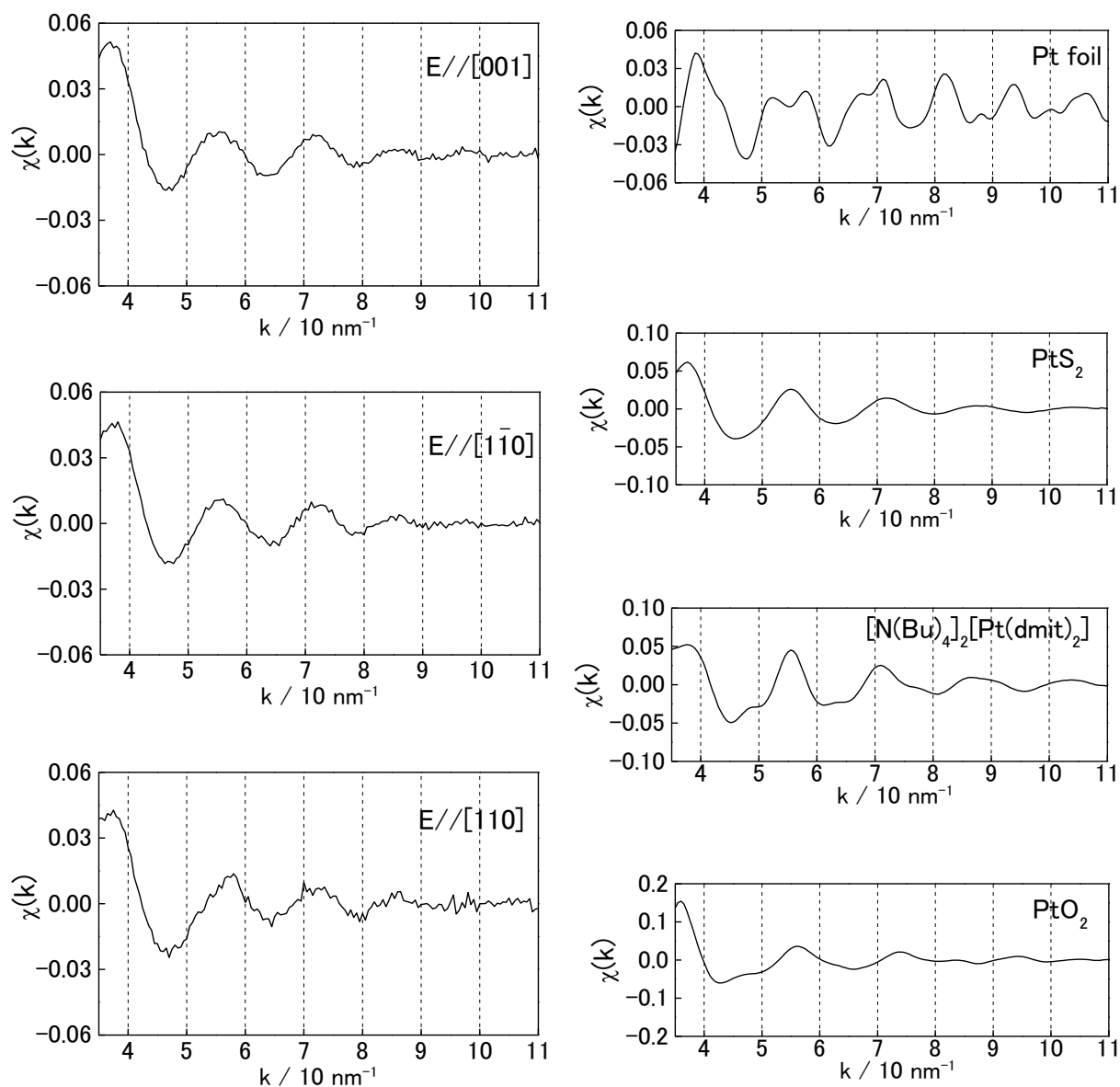


Figure 3.10 (a) Pt L_3 -edge XAFS spectra of Pt/o-MBA/TiO₂(110) obtained at three different polarization directions. (b) Pt L_3 -edge XAFS spectra of reference samples (Pt foil, platinum sulfide (PtS₂), bis(tetrabutylammonium) bis(1,3-dithiole-2-thione-4,5-dithiolato) platinum(II) ($[N(\text{Bu})_4]_2[\text{Pt}(\text{dmit})_2]$), and platinum oxide (PtO₂)).

dispersed Pt and small Pt clusters, such as dimers, trimers, and tetramers, were formed on the surface nonetheless.

Table 3.2 Curve fitting results for Pt/o-MBA/TiO₂(110) data obtained at three different polarization directions[#]

Orientation	Bond	N^*	r / nm	$\Delta E / \text{eV}$	$\sigma / 10^{-5} \text{ nm}$	$R \text{ factor} / \%$
$E // [001]$	Pt-S	1.1 ± 0.2	0.230 ± 0.002	6 ± 2	0.008 ± 0.002	1.4
	Pt-Pt	1.8 ± 0.4	0.267 ± 0.002	0 ± 2	0.007 ± 0.001	
$E // [1\bar{1}0]$	Pt-S	1.2 ± 0.2	0.229 ± 0.002	(6)	(0.008)	1.1
	Pt-Pt	1.7 ± 0.3	0.268 ± 0.002	(0)	(0.007)	
$E // [110]$	Pt-S	1.2 ± 0.2	0.229 ± 0.003	(6)	(0.008)	5.1
	Pt-Pt	1.5 ± 0.3	0.266 ± 0.003	(0)	(0.007)	

[#]Parentheses indicate those values fixed during the fitting procedure.

The average oxidation state of Pt in Pt/o-MBA/TiO₂(110) was determined from the XPS and XANES results. Figure 3.11 (a) and (b) shows the Pt L₃-edge XANES spectra of Pt/o-MBA/TiO₂(110) in three different polarization directions together with the spectra of some reference compounds. Figure 3.11 (c) is the plot of white line (WL) intensities (peak areas) for the reference compounds shown in Figure 3.11 (b) as a function of oxidation state. Since the WL, intense absorption peak, at the Pt L₃-edge is mainly assigned to electron transition from 2p_{3/2} to 5d_{3/2} and 5d_{5/2}, it is known as an informative index for the oxidation state and also for the ligand to which platinum is bonded. The WL intensities for Pt/o-MBA/TiO₂(110) were 8.5 ± 0.2 in three different polarization directions. I assume here that the Pt species were bonded to one or more oxygen atoms since bonding only with sulfur may not be enough to stabilize them although Pt-O bond is not detected in Table 3.2 probably due to its small backscattering factor compared with those of platinum and sulfur. Then the average oxidation state of the Pt species can be expected to be +1~+2 depending on the oxygen contribution as

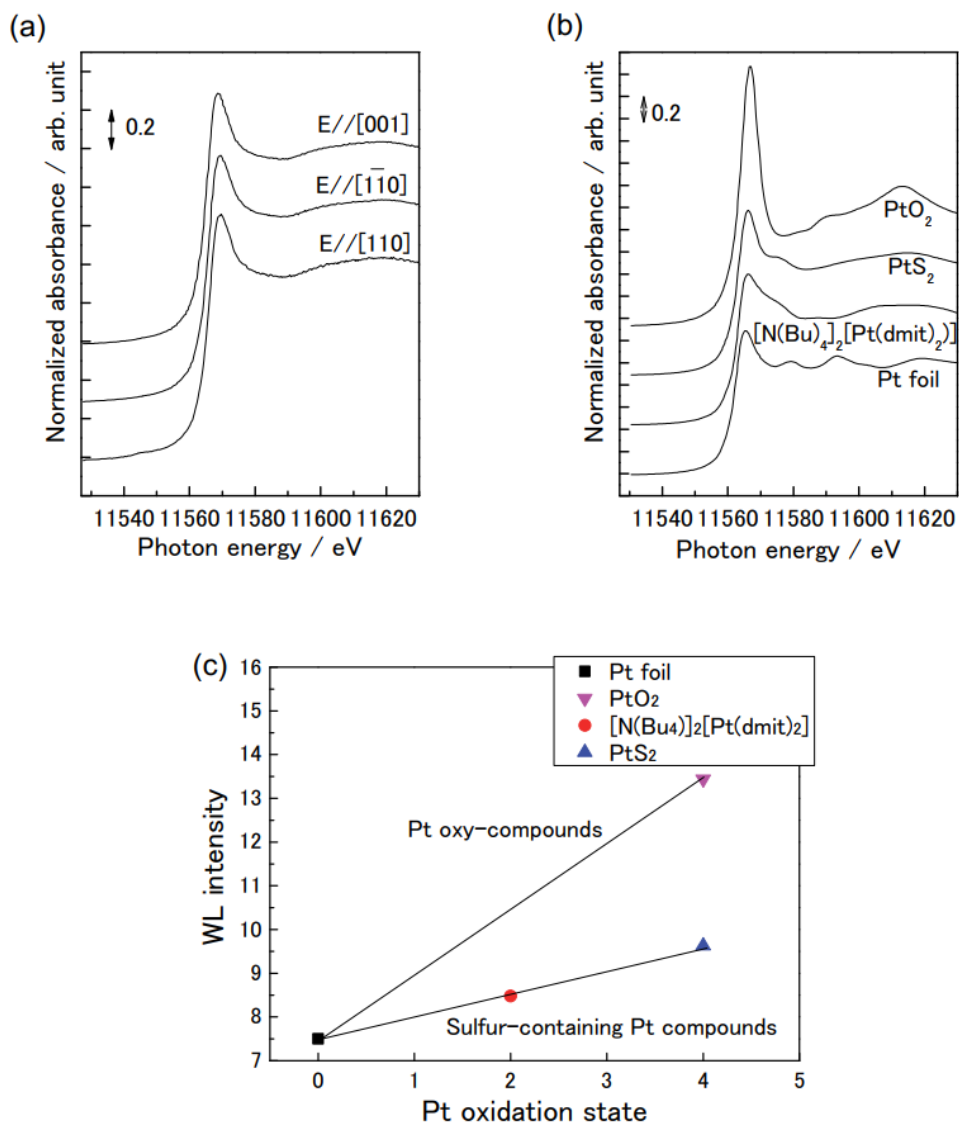


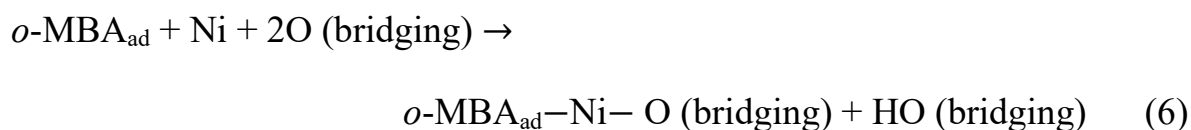
Figure 3.11 (a) Pt L_3 -edge XANES spectra of Pt/o-MBA/TiO₂(110) in three different polarization directions. (b) Pt L_3 -edge XANES spectra of reference compounds which are Pt metal (Pt foil), oxy-compound with Pt-O bonds (PtO₂) and sulfur-containing compounds with Pt-S bonds (PtS₂ and [N(Bu)₄]₂[Pt(dmit)₂]). (c) Plot of white line (WL) peak areas for the reference compounds as a function of oxidation state.

shown in Figure 3.11 (c). The XPS binding energy of the Pt4f_{7/2} peak is 72.3 eV (Figure 3.9 (a)) which is higher than that of Pt metal (71.2 eV) [57] and lower than those of PtS(II) (72.55 eV) [58], PtO(II) (74.4 eV) [59], which supports the XANES results.

A previous scanning tunneling microscopy (STM) study of Pt deposited on a bare TiO₂(110) surface found that the Pt had aggregated to form clusters with heights below 0.8 nm even at a low coverage of 0.07 ML [60]. In the present study, because Pt-S bonds were detected and the formation of small clusters at a Pt coverage of 0.11 ML, it can be concluded that pre-modification of the TiO₂(110) surface with *o*-MBA effectively suppressed any significant aggregation of the deposited Pt atoms, although the dispersion effect of the *o*-MBA was not strong enough to produce perfect atomic dispersion of the Pt atoms.

3.4.3. Formation mechanism of atomically dispersed metal species and small metal clusters on *o*-MBA/TiO₂(110): Comparison of Ni, Pt, Cu, and Au cases

Metal atoms deposited on a bare TiO₂(110) surface will migrate until they find stable adsorption sites. Because the single metal-O bond on the terrace surface is too weak to stabilize the metal monomers, these atoms will continue to diffuse until finding other metal atoms, resulting in aggregation and the formation of clusters. However, when *o*-MBA is applied to the TiO₂(110) surface, the dangling S bonds can be directed toward the diffusing metal atoms. If metal-S bond formation is energetically favorable compared with metal-metal bond formation, the metal atoms will be trapped by the S-metal-O bonding motif and stabilized, as illustrated in Figure 3.6. Otherwise, aggregation of the metal atoms will take place. The formation of the S-metal-O bonding motif can be described as follows, using Ni as an example.



Deposited Ni, Cu [10], and Au [31] atoms have all been found to form a stable S-metal-O bonding motif on the *o*-MBA/TiO₂(110) surface.

In Table 3.3, the strengths of metal-metal (M-M) and metal-S (M-S) bonds (as assessed by their bond dissociation energies at 298 K, D_{298}°) are listed for Ni, Pt, Cu, and Au [61, 62]. The D_{298}° (M-M) value for Pt is the highest among the four metals, and Pt is the only metal for which D_{298}° (M-M) is greater than D_{298}° (M-S). These results indicate that metal-S bond formation is energetically

more favorable compared with metal-metal bond formation in the case of Ni, Cu, and Au, but not for Pt, which is in agreement with our Pt/*o*-MBA/TiO₂(110) results discussed in Section 3.4.2. The affinity of the metal atoms for oxygen will also be important in addition to the affinity for sulfur to account for the stability of the S-metal-O bond. Thus, the metal-oxygen (M-O) bond strengths ($D_{298}^{\circ}(\text{M-O})$) for Ni, Pt, Cu, and Au are also listed in Table 3.3 [61, 63]. The affinity for oxygen decreases in the order of Ni > Cu > Pt > Au. It can be defined a term, R_{S-M-O} , that roughly estimates the formation preference and energetic stability of the S-metal-O bonding motif compared with metal-metal formation, as follows.

$$R_{S-M-O} = \frac{D_{298}^{\circ}(\text{M-S}) + D_{298}^{\circ}(\text{M-O})}{D_{298}^{\circ}(\text{M-M})} \quad (7)$$

The R_{S-M-O} values for Ni, Pt, Cu, and Au are 3.6, 1.6, 3.1, and 2.8, respectively. Thus, the R_{S-M-O} value for Pt is the lowest, indicating that this metal generates the least stable S-metal-O bonding motif. The aggregation of Pt is the most likely to proceed due to the fact that it has the highest $D_{298}^{\circ}(\text{M-M})$, lowest $D_{298}^{\circ}(\text{M-S})$ and 2nd lowest $D_{298}^{\circ}(\text{M-O})$ values, indicating the preferential formation of Pt-Pt bonds, resulting in clustering on the *o*-MBA/TiO₂(110). In the case of Ni and Cu, both $D_{298}^{\circ}(\text{M-S})$ and $D_{298}^{\circ}(\text{M-O})$ values contribute almost equally to the corresponding R_{S-M-O} values. In contrast, in the case of Au, the $D_{298}^{\circ}(\text{M-S})$ value makes a much greater contribution compared with the $D_{298}^{\circ}(\text{M-O})$ value. Although the $D_{298}^{\circ}(\text{M-O})$ and $D_{298}^{\circ}(\text{M-M})$ values for Au are the lowest and 2nd highest among the four metals, respectively, this metal has a relatively high R_{S-M-O} of 2.8 because of its high $D_{298}^{\circ}(\text{M-S})$. These results suggest a high affinity of Au atoms for S atoms, in good agreement with previous reports [64, 65].

Similarly, if the O-metal-O bonding motif can be obtained through the formation of two metal-O bonds on the TiO₂(110) surface, metal monomers can be stabilized on a TiO₂(110) surface [8, 21]. In the previous study, atomically dispersed Ni species were formed without employing *o*-MBA to generate the O-Ni-O motif at the $\langle 1\bar{1}n \rangle$ step edges under conditions in which the Ni coverage was very low (~ 0.02 ML) [21]. Cu was also atomically dispersed on a TiO₂(110) surface premodified with an acetic anhydride layer [8]. This Cu formed an O-Cu-O motif, in which one oxygen was a bridging O from the TiO₂(110) and the other was contributed by the acetate. There also is an attempt to prepare the O-Au-O

bonding motif on a similar surface, although this trial was unsuccessful and instead generated Au aggregates that formed clusters [66]. It can be also defined a term $R_{O-M-O} = 2D_{298}^{\circ}(M-O) / D_{298}^{\circ}(M-M)$ that allows us to compare the energetic stability between O-metal-O and metal-metal bond formation, in a similar manner to the procedure outlined in the above discussion of the S-metal-O bonding motif. The R_{O-M-O} values for Ni, Cu, and Au are 3.8, 3.0, and 2.0, respectively, indicating the stability of the O-metal-O bond motif decreases in the order of Ni > Cu > Au. This result suggests the low stability of the O-Au-O motif and thus predicts Au aggregation. Therefore, the R_{O-M-O} value might also serve as a good indicator to show the possibility of obtaining an atomically dispersed species on an oxide surface.

Table 3.3 Strengths of metal-metal (M-M), metal-sulfur (M-S) and metal-oxygen (M-O) bonds (bond dissociation energies at 298 K, D_{298}°) for Ni, Pt, Cu, and Au [61], and the corresponding R_{S-M-O} and R_{O-M-O} values.

Metal	$D_{298}^{\circ}(\text{M-M}) /$ kJ/mol	$D_{298}^{\circ}(\text{M-S})$ / kJ/mol	$D_{298}^{\circ}(\text{M-O}) /$ kJ/mol	R_{S-M-O}		R_{O-M-O}	
Ni	201	344	382	3.6	○ ^b	3.8	○ ^e
Pt	307	233 ^a	246 ^a	1.6	× ^b		
Cu	177	276	269	3.1	○ ^c	3.0	○ ^f
Au	226	418	221	2.8	○ ^d	2.0	× ^g

^a $D_{298}^{\circ}(\text{M-S})$ and $D_{298}^{\circ}(\text{M-O})$ for Pt are taken from references [62] and [63], respectively. ^b Present work. ^c Reference 9. ^d Reference [67]. ^e Reference [31]. ^f Reference [21]. ^g Reference [8].

○ and × indicate atomic dispersion of the evaporated metal atoms and aggregation of them, respectively.

3.5. Conclusions

Atomically dispersed Ni species were formed on a TiO₂(110) surface premodified with *o*-MBA. The three-dimensional structure of the Ni species was determined using the PTRF-EXAFS technique. A S-Ni-O motif, which is similar to the local metal structure found in previous studies with Cu and Au, was formed on the modified TiO₂(110) surface. In contrast, Pt was not atomically dispersed but instead aggregated to form clusters on the *o*-MBA/TiO₂(110) due to the low affinity of Pt atoms for S atoms compared with that for other Pt atoms. The energetic stabilities of the S-metal-O motif when using Ni, Pt, Cu, and Au were discussed based on the difference between the S-metal-O and metal-metal bond formation energies. A new indicator, R_{X-M-O} (X=S or O), has been proposed for the single metal dispersion on the TiO₂(110) surface.

REFERENCES

- [1] T. Steiner, S-H...S hydrogen-bond chain in thiosalicylic acid, *Acta Crystallographica Section C*, 56 (2000) 876-877.
- [2] U. Helmstedt, S. Lebedkin, T. Höcher, S. Blaurock, E. Hey-Hawkins, 4-Thiolatobenzoate-Bridged Gold/Zirconium Complex and Its Mononuclear Precursors, *Inorg. Chem.*, 47 (2008) 5815-5820.
- [3] C.E. Rowland, N. Belai, K.E. Knope, C.L. Cahill, Hydrothermal Synthesis of Disulfide-Containing Uranyl Compounds: In Situ Ligand Synthesis versus Direct Assembly, *Crystal Growth & Design*, 10 (2010) 1390-1398.
- [4] S. Takakusagi, W.J. Chun, H. Uehara, K. Asakura, Y. Iwasawa, Polarization-Dependent Total-Reflection Fluorescence X-ray Absorption Fine Structure for 3D Structural Determination and Surface Fine Tuning, *Top. Catal.*, 56 (2013) 1477-1487.
- [5] U. Diebold, The surface science of titanium dioxide, *Surface Science Reports*, 48 (2003) 53-229.
- [6] F. Averseng, M. Vennat, M. Che, Grafting and Anchoring of Transition Metal Complexes to Inorganic Oxides, *Handbook of Heterogeneous Catalysis*, Wiley-VCH, New York, 2008, pp. 522-539.
- [7] W.-J. Chun, Y. Koike, K. Ijima, K. Fujikawa, H. Ashima, M. Nomura, Y. Iwasawa, K. Asakura, Preparation of atomically dispersed Cu species on a TiO₂ (110) surface premodified with an organic compound, *Chem. Phys. Lett.*, 433 (2007) 345-349.
- [8] W.-J. Chun, Y. Koike, H. Ashima, K. Kinoshita, K. Ijima, K. Fujikawa, S. Suzuki, M. Nomura, Y. Iwasawa, K. Asakura, Atomically dispersed Cu species on a TiO₂(110) surface precovered with acetic anhydride, *Chem. Phys. Lett.*, 470 (2009) 99-102.
- [9] M. Flytzani-Stephanopoulos, B.C. Gates, Atomically dispersed supported metal catalysts, *Annu. Rev. Chem. Biomol. Eng.*, 3 (2012) 545-574.
- [10] S. Takakusagi, H. Nojima, H. Ariga, H. Uehara, K. Miyazaki, W.J. Chun, Y. Iwasawa, K. Asakura, Fine tuning and orientation control of surface Cu complexes on TiO₂(110) premodified with mercapto compounds: the effect of different mercapto group positions, *Physical Chemistry Chemical Physics*, 15 (2013) 14080-14088.
- [11] W.J. Chun, K. Asakura, Y. Iwasawa, Surface structure analysis of dispersed metal sites on single crystal metal oxides by means of polarization-dependent total-reflection fluorescent EXAFS, *Appl Surf Sci*, 100 (1996) 143-146.

- [12] K. Asakura, W.J. Chun, M. Shirai, K. Tomishige, Y. Iwasawa, In-situ polarization-dependent total-reflection fluorescence XAFS studies on the structure transformation of Pt clusters on α -Al₂O₃(0001), *J. Phys. Chem. B*, 101 (1997) 5549-5556.
- [13] W.J. Chun, K. Asakura, Y. Iwasawa, Polarization-dependent total-reflection fluorescence XAFS study of Mo oxides on a rutile TiO₂(110) single crystal surface, *J. Phys. Chem. B*, 102 (1998) 9006-9014.
- [14] W.J. Chun, K. Asakura, Y. Iwasawa, The structure analysis of MoO_x/TiO₂(110) by polarization-dependent total-reflection fluorescence X-ray absorption fine structure, *Catal Today*, 44 (1998) 309-314.
- [15] W.J. Chun, K. Asakura, Y. Iwasawa, Anisotropic structure analysis for Mo oxides on TiO₂(110) single crystal surface by polarization-dependent total-reflection fluorescence EXAFS, *Chem. Phys. Lett.*, 288 (1998) 868-872.
- [16] K. Asakura, W.J. Chun, Y. Iwasawa, Polarization-dependent total-reflection fluorescence EXAFS study about active structures on single crystal oxides as model catalyst surfaces, *Top. Catal.*, 10 (2000) 209-219.
- [17] W.J. Chun, K. Asakura, Y. Iwasawa, Anisotropic ordering of Mo species deposited on TiO₂(110) characterized by polarization-dependent total reflection fluorescence EXAFS (PTRF-EXAFS), *Catal Today*, 66 (2001) 97-103.
- [18] W.-J. Chun, Y. Tanizawa, T. Shido, Y. Iwasawa, M. Nomura, K. Asakura, Development of an in situ polarization-dependent total-reflection fluorescence XAFS measurement system, *Journal of Synchrotron Radiation*, 8 (2001) 168-172.
- [19] Y. Tanizawa, W.J. Chun, T. Shido, K. Asakura, Y. Iwasawa, Three-dimensional analysis of the local structure of Cu on TiO₂(110) by in situ polarization-dependent total-reflection fluorescence XAFS, *Journal of Synchrotron Radiation*, 8 (2001) 508-510.
- [20] Y. Tanizawa, T. Shido, W.J. Chun, K. Asakura, M. Nomura, Y. Iwasawa, Three-dimensional structure analyses of Cu species dispersed on TiO₂(110) surfaces studied by polarization-dependent total-reflection fluorescence X-ray absorption fine structure (PTRF-XAFS), *J. Phys. Chem. B*, 107 (2003) 12917-12929.
- [21] Y. Koike, K. Ijima, W.J. Chun, H. Ashima, T. Yamamoto, K. Fujikawa, S. Suzuki, Y. Iwasawa, M. Nomura, K. Asakura, Structure of low coverage Ni atoms on the TiO₂(110) surface - Polarization dependent total-reflection fluorescence EXAFS study, *Chem. Phys. Lett.*, 421 (2006) 27-30.
- [22] Y. Koike, K. Fujikawa, S. Suzuki, W.J. Chun, K. Ijima, M. Nomura, Y. Iwasawa, K. Asakura, Origin of self-regulated cluster growth on the TiO₂(110)

surface studied using polarization-dependent total reflection fluorescence XAFS, *J. Phys. Chem. C*, 112 (2008) 4667-4675.

[23] W.J. Chun, K. Miyazaki, N. Watanabe, Y. Koike, S. Takakusagi, K. Fujikawa, M. Nomura, Y. Iwasawa, K. Asakura, Au Clusters on TiO₂(110) (1 x 1) and (1 x 2) Surfaces Examined by Polarization-Dependent Total Reflection Fluorescence XAFS, *J. Phys. Chem. C*, 117 (2013) 252-257.

[24] G. Pfaff, P. Reynders, Angle-Dependent Optical Effects Deriving from Submicron Structures of Films and Pigments, *Chemical Reviews*, 99 (1999) 1963-1981.

[25] A. Salvador, M.C. Pascual-Martí, J.R. Adell, A. Requeni, J.G. March, Analytical methodologies for atomic spectrometric determination of metallic oxides in UV sunscreen creams, *Journal of Pharmaceutical and Biomedical Analysis*, 22 (2000) 301-306.

[26] R. Zallen, M.P. Moret, The optical absorption edge of brookite TiO₂, *Solid State Communications*, 137 (2006) 154-157.

[27] J.H. Braun, A. Baidins, R.E. Marganski, TiO₂ pigment technology: a review, *Progress in Organic Coatings*, 20 (1992) 105-138.

[28] A. Fujishima, K. Honda, Electrochemical photolysis of water at a semiconductor electrode, *Nature*, 238 (1972) 37-38.

[29] D.A. Tryk, A. Fujishima, K. Honda, Recent topics in photoelectrochemistry: Achievements and future prospects, *Electrochimica Acta*, 45 (2000) 2363-2376.

[30] S.-D. Mo, W.Y. Ching, Electronic and optical properties of three phases of titanium dioxide: Rutile, anatase, and brookite, *Physical Review B*, 51 (1995) 13023.

[31] K. Asakura, S. Takakusagi, H. Ariga, W.-J. Chun, S. Suzuki, Y. Koike, H. Uehara, K. Miyazaki, Y. Iwasawa, Preparation and structure of a single Au atom on the TiO₂(110) surface: control of the Au-metal oxide surface interaction, *Faraday Discuss.*, 162 (2013) 165-177.

[32] S. Takakusagi, A. Kunimoto, N. Sirisit, H. Uehara, T. Ohba, Y. Uemuara, T. Wada, H. Ariga, W.J. Chun, Y. Iwasawa, K. Asakura, A New Indicator for Single Metal Dispersion on a TiO₂(110) Surface Premodified with a Mercapto Compound, *J. Phys. Chem. C*, 120 (2016) 15785-15791.

[33] J. Tersoff, R.M. Tromp, Shape transition in growth of strained islands: Spontaneous formation of quantum wires, *Phys Rev Lett*, 70 (1993) 2782-2785.

[34] A.-L. Barabási, Self-assembled island formation in heteroepitaxial growth, *Appl Phys Lett*, 70 (1997) 2565-2567.

- [35] H. Brune, M. Giovannini, K. Bromann, K. Kern, Self-organized growth of nanostructure arrays on strain-relief patterns, *Nature*, 394 (1998) 451.
- [36] M. Kästner, B. Voigtländer, Kinetically Self-Limiting Growth of Ge Islands on Si(001), *Phys Rev Lett*, 82 (1999) 2745-2748.
- [37] S.C. Parker, A.W. Grant, V.A. Bondzie, C.T. Campbell, Island growth kinetics during the vapor deposition of gold onto TiO₂(110), *Surface Science*, 441 (1999) 10-20.
- [38] L. Vitali, M.G. Ramsey, F.P. Netzer, Nanodot Formation on the $\text{Si}(111)$ - (7×7) Surface by Adatom Trapping, *Phys Rev Lett*, 83 (1999) 316-319.
- [39] D.A. Chen, M.C. Bartelt, S.M. Seutter, K.F. McCarty, Small, uniform, and thermally stable silver particles on TiO₂(110)-(1 \times 1), *Surface Science*, 464 (2000) L708-L714.
- [40] A. Kolmakov, D.W. Goodman, In situ scanning tunneling microscopy of oxide-supported metal clusters: Nucleation, growth, and thermal evolution of individual particles, *The Chemical Record*, 2 (2002) 446-457.
- [41] J. Zhou, D.A. Chen, Controlling size distributions of copper islands grown on TiO₂(110)-(1 \times 2), *Surface Science*, 527 (2003) 183-197.
- [42] Q. Wu, T.E. Madey, Site specific nucleation of Ni nanoclusters on S(4 \times 4)/W(111), *Surface Science*, 555 (2004) 167-178.
- [43] R. Nakamura, N. Ohashi, A. Imanishi, T. Osawa, Y. Matsumoto, H. Koinuma, Y. Nakato, Crystal-Face Dependences of Surface Band Edges and Hole Reactivity, Revealed by Preparation of Essentially Atomically Smooth and Stable (110) and (100) n-TiO₂ (Rutile) Surfaces, *The Journal of Physical Chemistry B*, 109 (2005) 1648-1651.
- [44] Y. Yuichi, N. Kazuko, O. Takeo, M. Yuji, K. Hideomi, Preparation of Atomically Smooth TiO₂ Single Crystal Surfaces and Their Photochemical Property, *Japanese Journal of Applied Physics*, 44 (2005) L511.
- [45] M. Nomura, A. Koyama, Design of an XAFS beamline at the Photon Factory: possibilities of bent conical mirrors, *Journal of Synchrotron Radiation*, 6 (1999) 182-184.
- [46] T. Taguchi, REX2000 Version 2.5: Improved DATA Handling and Enhanced User-Interface, *AIP Conference Proceedings*, 882 (2007) 162-164.
- [47] J.W. Cook, D.E. Sayers, Criteria for automatic x-ray absorption fine structure background removal, *Journal of Applied Physics*, 52 (1981) 5024-5031.

- [48] K. Asakura, Polarization-dependent total reflection fluorescence extended X-ray absorption fine structure and its application to supported catalysis, *Catalysis: Volume 24*, The Royal Society of Chemistry, 2012, pp. 281-322.
- [49] A.L. Ankudinov, B. Ravel, J.J. Rehr, S.D. Conradson, Real-space multiple-scattering calculation and interpretation of x-ray-absorption near-edge structure, *Phys. Rev. B*, 58 (1998) 7565-7576.
- [50] R.D. Willett, C.J. Gómez-García, B.L. Ramakrishna, B. Twamley, (NBu₄)Ni(mnt)₂: A novel bistable high temperature spin-Peierls-like system, *Polyhedron*, 24 (2005) 2232-2237.
- [51] H.W. Nesbitt, D. Legrand, G.M. Bancroft, Interpretation of Ni2p XPS spectra of Ni conductors and Ni insulators, *Physics and Chemistry of Minerals*, 27 (2000) 357-366.
- [52] A.N. Mansour, C.A. Melendres, Analysis of X-ray Absorption Spectra of Some Nickel Oxycompounds Using Theoretical Standards, *The Journal of Physical Chemistry A*, 102 (1998) 65-81.
- [53] K. Fujikawa, S. Suzuki, Y. Koike, W.-J. Chun, K. Asakura, Self-regulated Ni cluster formation on the TiO₂(110) terrace studied using scanning tunneling microscopy, *Surface Science*, 600 (2006) 117-121.
- [54] P.L. Cao, D.E. Ellis, V.P. Dravid, First-principles study of initial stage of Ni thin-film growth on a TiO₂ (110) surface, *Journal of Materials Research*, 14 (2011) 3684-3689.
- [55] A.F. Carley, P.R. Chalker, J.C. Riviere, M.W. Roberts, The identification and characterisation of mixed oxidation states at oxidised titanium surfaces by analysis of X-ray photoelectron spectra, *Journal of the Chemical Society, Faraday Transactions 1: Physical Chemistry in Condensed Phases*, 83 (1987) 351-370.
- [56] Y. Lei, J. Jelic, L.C. Nitsche, R. Meyer, J. Miller, Effect of Particle Size and Adsorbates on the L₃, L₂ and L₁ X-ray Absorption Near Edge Structure of Supported Pt Nanoparticles, *Top. Catal.*, 54 (2011) 334-348.
- [57] M. Peuckert, H.P. Bonzel, Characterization of oxidized platinum surfaces by X-ray photoelectron spectroscopy, *Surface Science*, 145 (1984) 239-259.
- [58] NIST X-ray Photoelectron Spectroscopy Database, National Institute of Standards and Technology, Gaithersburg, 2012.
- [59] T. Fleisch, G.J. Mains, Photoreduction and reoxidation of platinum oxide and palladium oxide surfaces, *The Journal of Physical Chemistry*, 90 (1986) 5317-5320.

- [60] J.B. Park, S.F. Conner, D.A. Chen, Bimetallic Pt–Au Clusters on TiO₂(110): Growth, Surface Composition, and Metal–Support Interactions, *The Journal of Physical Chemistry C*, 112 (2008) 5490-5500.
- [61] D.R. Lide, *Strengths of Chemical Bonds*, CRC handbook of chemistry and physics, Boca Raton, FL: CRC Press, 2005.
- [62] H. Toulhoat, P. Raybaud, S. Kasztelan, G. Kresse, J. Hafner, Transition metals to sulfur binding energies relationship to catalytic activities in HDS: back to Sabatier with first principle calculations | This work has been undertaken within the “GdR Dynamique Moléculaire Quantique Appliquée à la Catalyse”, a joint project of Centre National de la Recherche Scientifique, Technische Universität Wien, and Institut Français du Pétrole.1, *Catal Today*, 50 (1999) 629-636.
- [63] Y. Nagano, Standard enthalpy of formation of platinum hydrous oxide, *Journal of Thermal Analysis and Calorimetry*, 69 (2002) 831-839.
- [64] H.A. Biebuyck, C.D. Bain, G.M. Whitesides, Comparison of Organic Monolayers on Polycrystalline Gold Spontaneously Assembled from Solutions Containing Dialkyl Disulfides or Alkanethiols, *Langmuir*, 10 (1994) 1825-1831.
- [65] A. Ulman, *An Introduction to Ultrathin Organic Films: From Langmuir--Blodgett to Self--Assembly*, Academic press, 2013.
- [66] W.J. Chun, Y. Koike, K. Ijima, H. Ashima, G. Tateno, M. Nomura, Y. Iwasawa, K. Asakura, Surface Structure of Au species on the Promodified TiO₂(110) with Acetic Anhydride, 2006, pp. 26.
- [67] S. Takakusagi, H. Nojima, H. Ariga, H. Uehara, K. Miyazaki, W.J. Chun, Y. Iwasawa, K. Asakura, Fine tuning and orientation control of surface Cu complexes on TiO₂(110) premodified with mercapto compounds: The effect of different mercapto group positions, *Physical Chemistry Chemical Physics*, 15 (2013) 14080-14088.

Chapter 4

What is the origin for Mechanochromism of Gold (I) complex $(\text{C}_6\text{F}_5\text{Au})_2(\mu\text{-1,4-Diisocyano benzene})$ - Direct evidence for the presence of Auophilic interaction

4.1. Background

Mechanochromism is the phenomenon in which the solid compound undergoes the color change by mechanical treatment such as shearing, grinding, ball milling. The mechanochromism draws a lot of interest because it can be used as recording and sensing materials. It has been reported that gold complexes could exhibit the mechanochromism properties [1-5]. Gold complexes are currently considered to be an important research topic owing to their unique structural and luminescence properties and responses to stimuli [6-8]. The luminescence properties of many gold complexes are sensitive to their molecular arrangements and intermolecular interaction patterns [9-14]. H. Ito prepared the gold (I) complex, $[(\text{C}_6\text{F}_5\text{Au})_2(\mu\text{-1,4-diisocyanobenzene})]$ (**1**), and found its reversible

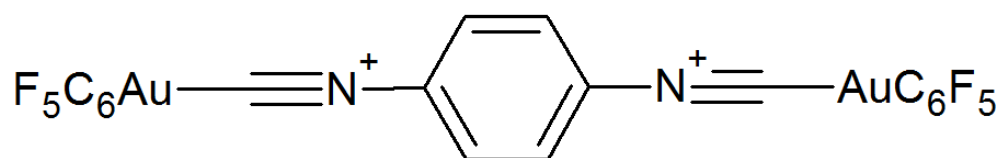


Figure 4.1 molecular structure of **1** or $(\text{C}_6\text{F}_5\text{Au})_2(\mu\text{-1,4-diisocyano benzene})$.

unique mechanochromic property [1]. Its molecular structure is shown in figure 4.1. Figure 4.2 shows the distinct properties of the complex (**1**). They reported that its luminescence color was changed from blue to yellow when the crystal (**1**) was ground to amorphous state. The luminescence color is reverted to the original

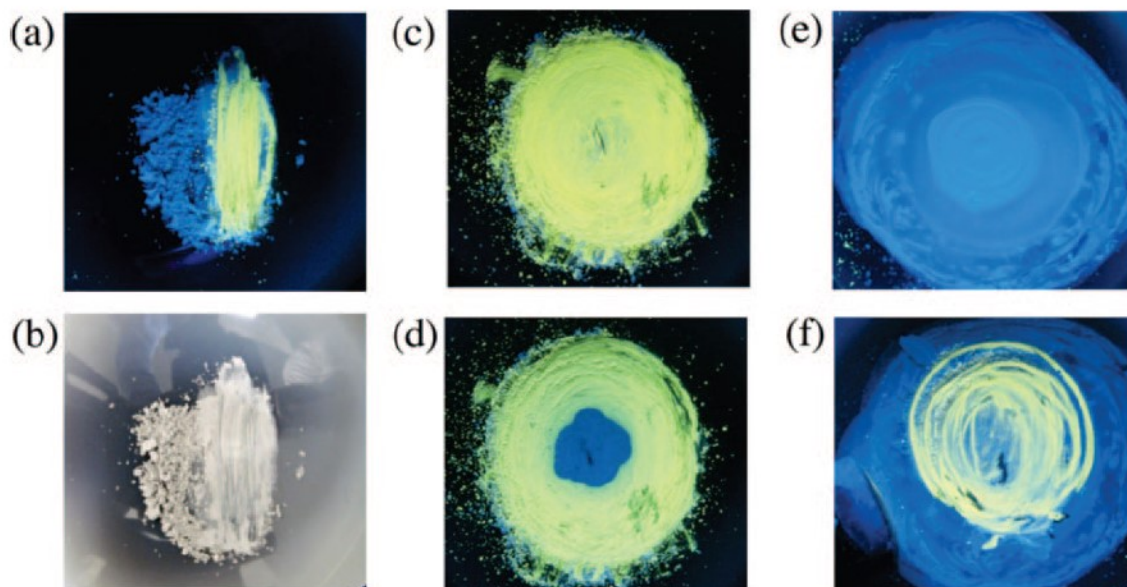


Figure 4.2 Photographs showing Au(I) complex 1 on an agate mortar under UV irradiation with black light (365 nm), unless otherwise noted: (a) Au(I) complex 1 powder after grinding the right-half with a pestle, (b) a same sample under ambient light, (c) entirely ground powder of 1, (d) partial reversion to the blue luminescence by dropwise treatment using dichloromethane onto the center of the ground powder, (e) powder after treatment with dichloromethane, and (f) repetition of the yellow emission by scratching the powder with a pestle [1]. Reprinted (adapted) with permission from (Ito et al.). Copyright (2008) American Chemical Society.

when treat the complex powder with dichloromethane. If the powder obtained from the treatment is scratched with a pestle again, its luminescence color is changed from blue to yellow, the same one as exhibit before the treatment.

Results from analysis of emission spectra are shown in figure 4.4. By looking at these spectra, you can see that emission band from unground solid, treated with dichloromethane, crystal and dilute solution of the solid in solvent are similar. From these results, they concluded that blue emissions occurred from single molecule. Complex (1) was recrystallized from chlorobenzene yielding single crystals suitable for XRD analysis. Single crystal X-ray diffraction (XRD) reveals the structure of blue luminescence polymorph and is shown in figure 4.3. It was found that the shortest Au-Au distance is 5.19 Å. Figure 4.5 shows the IR and powder XRD spectra of complex (1) in various states. It was found that the

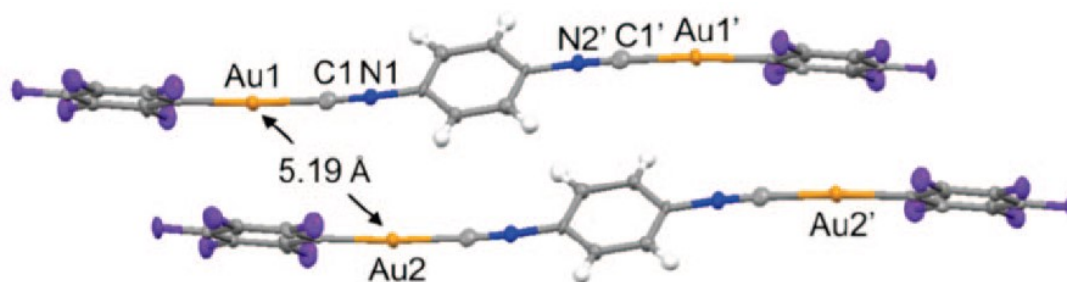


Figure 4.4 Partial view of the crystal packing of a blue luminescent crystal of **1**. Thermal ellipsoids were drawn at 50%-probability level. Crystal data: monoclinic, $P21/c$ (No. 14), $a = 5.190(2) \text{ \AA}$, $b = 17.154(6) \text{ \AA}$, $c = 10.861(4) \text{ \AA}$, $\beta = 90.83(3)^\circ$, $V = 966(2) \text{ \AA}^3$, $Z = 2$. $T = 296.2 \text{ K}$. $2\theta_{\text{max}} = 55.0^\circ$, $R = 0.0355$ ($I > 2.00\sigma(I)$), $R_w = 0.0976$, $\text{GOF} = 1.007$ [1]. Reprinted (adapted) with permission from (Ito et al.). Copyright (2008) American Chemical Society.

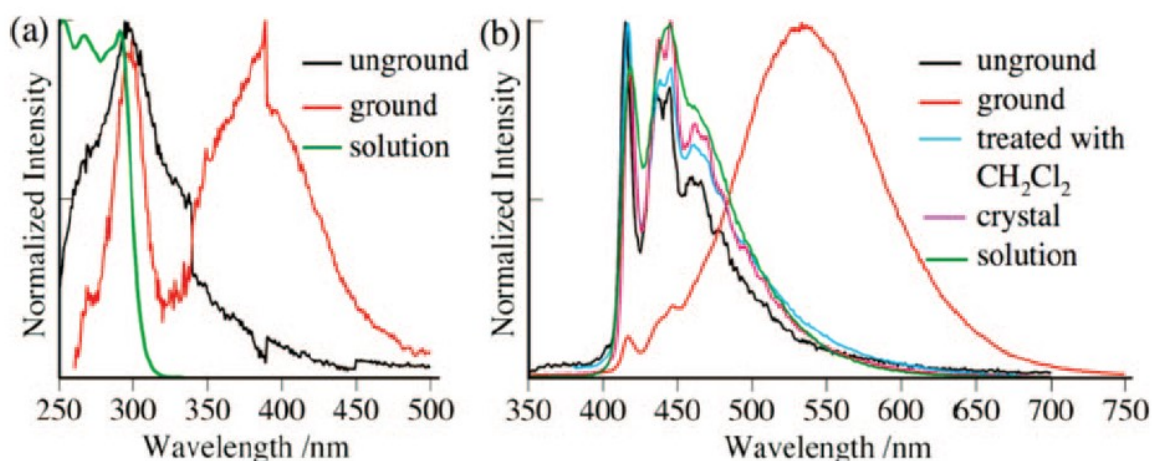


Figure 4.3 (a) Absorption and (b) emission (excited at 260 nm) spectra of **1** in various states. Reprinted (adapted) with permission from (Ito et al.). Copyright (2008) American Chemical Society.

unground solid showed a single absorption at 2220 cm^{-1} which was assigned to the isocyanide $\text{N}\equiv\text{C}$ stretching. On the other hand, the ground solid exhibited two absorbance at 2218 and 2208 cm^{-1} . The authors suggested that considerable changes occur in the coordination mode of the isocyanide ligand to the Au(I) atom upon grinding. The authors also suggested that this change results from the formation of aurophilic bond. In addition, the IR spectra also showed that the IR

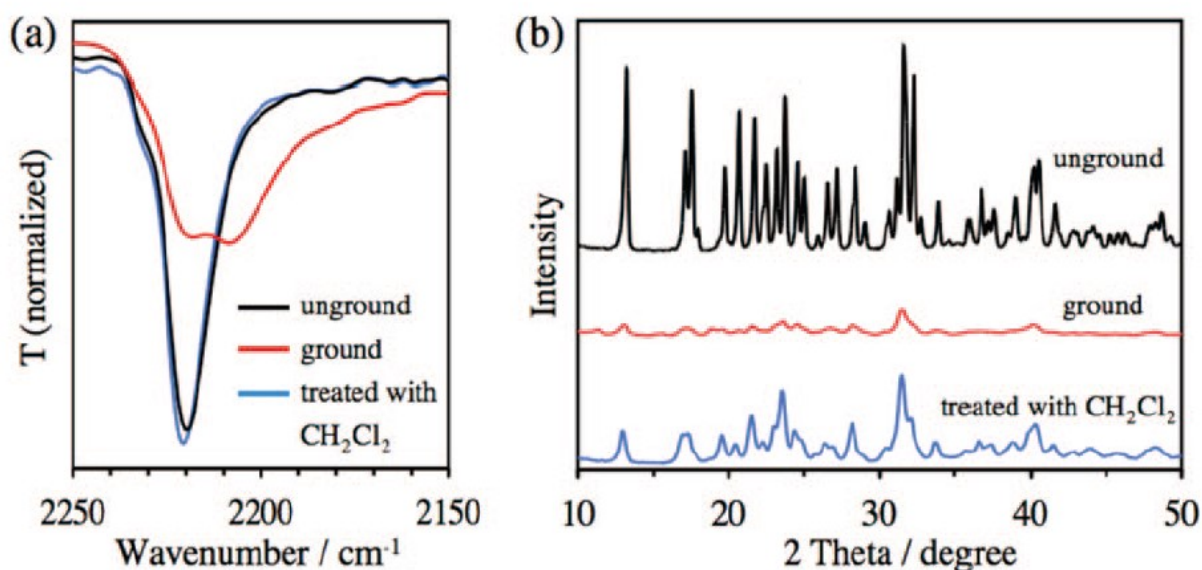


Figure 4.5 IR and XRD spectra of **1** in various states [1]. Reprinted (adapted) with permission from (Ito et al.). Copyright (2008) American Chemical Society.

pattern of ground solid reverted to that of the unground solid upon treatment with dichloromethane. Results from Differential scanning calorimetry (DSC) and Thermogravimetric analysis (TGA) indicated that grinding does not destroy molecular structure. From these results, it can be concluded that mechanochromism due to neither molecular decomposition nor heat.

The origin of the color change was postulated to be due to the creation of Auophilic interaction, according to the author. However, the ground Au complex structure remains unknown because of its amorphous structure (Figure 4.5). We have applied Extended X-ray Absorption Fine Structure (EXAFS) to get the local structure of Au in order to see if there is a microscopic change in its structure after grinding or not.

4.2. Experimental procedure

The $(C_6F_5Au)_2(\mu-1,4\text{-Diisocyanobenzene})$ or crystal **1** was supplied by Prof. Hajime Ito. The synthesis procedure was described elsewhere [1].

EXAFS measurements were performed at the BL12C unit of the Photon Factory at the Institute of Materials Structure Science (KEK-IMSS-PF, Tsukuba,

Japan).¹⁵ The storage ring energy and ring current were 2.5 GeV and 450 mA, respectively. The EXAFS spectra is measured in quick transmission mode which Si(311) as a double crystal monochromator and Ionization chamber as a detector. The Helium cryostat (Jeneis, STVP-100) was set up as shown in figure 4.6 and used to control the sample temperature during measurement from 5K to 297K. After obtaining the data, several procedures were employed to extract the information from the data as has been described in general experimental procedure in Chapter 2.

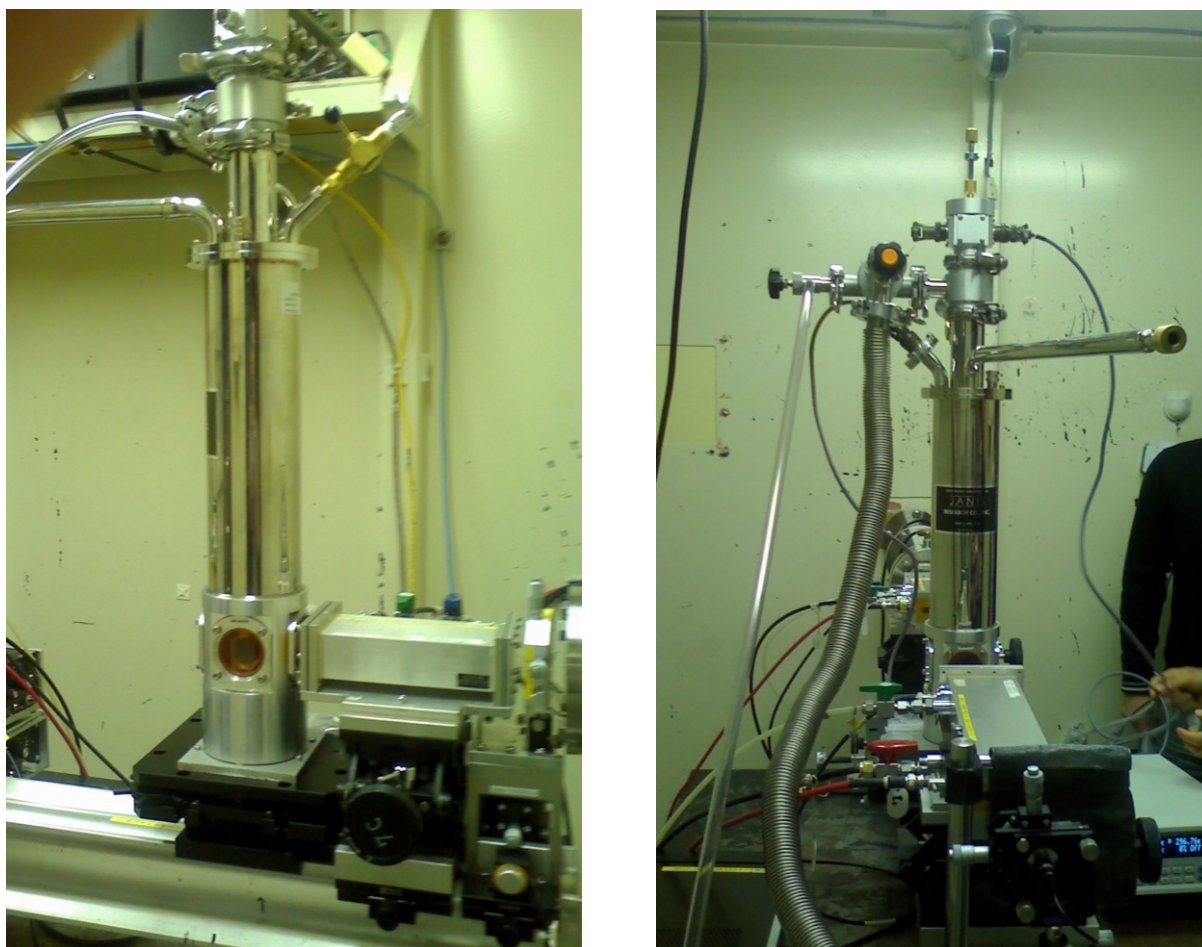


Figure 4.6 Experimental setup

4.3. Results and Discussion

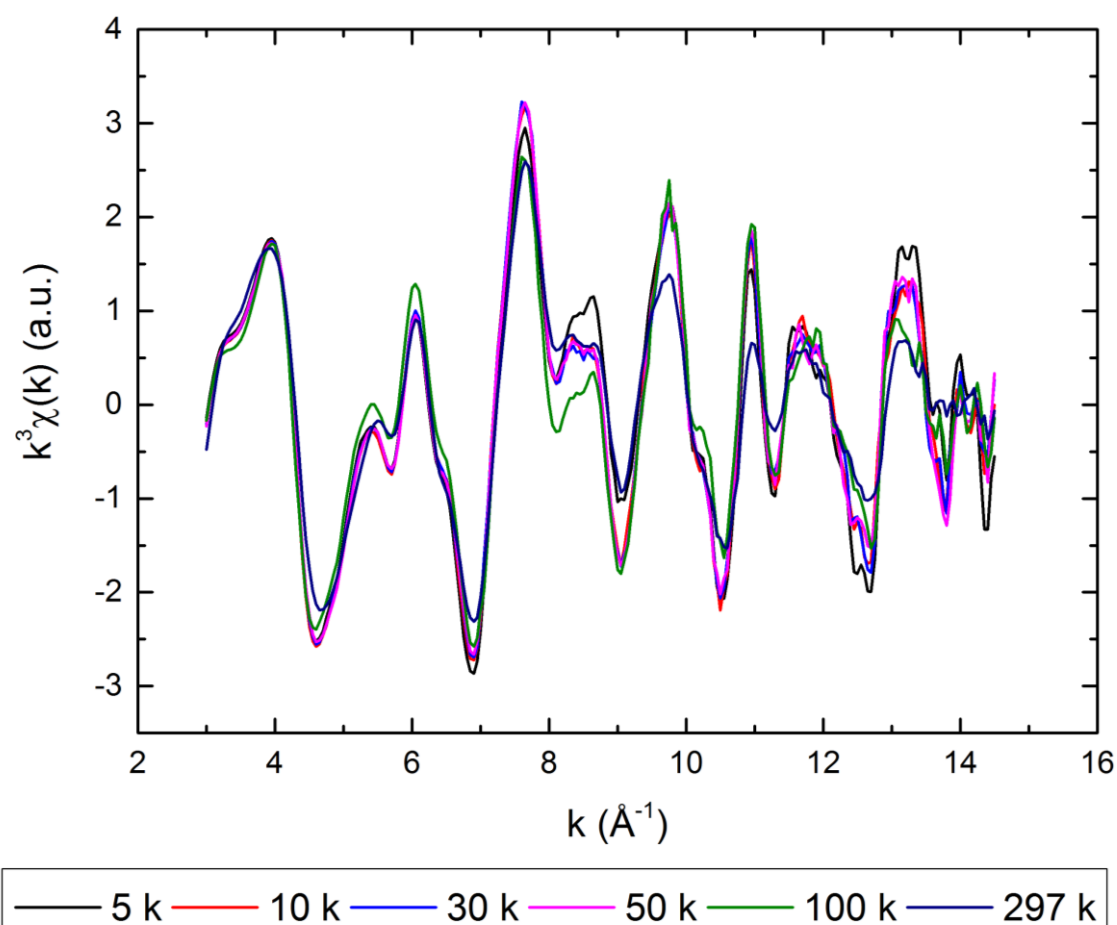


Figure 4.7 XAFS oscillation of various temperature of measurements.

Figure 4.7 shows the k space spectra of ground sample at various measurement temperatures. They show similar features indicating that there is no change in local structure around the Au atom at any temperature. These k space spectra were Fourier transformed into r space and curve fitting were performed. Table 4.1 shows the parameters using in the Fourier transformation. Then, the curve fitting begins with the 5K data set. Backscattering amplitude and phase shift values for Carbon and Gold shell are obtained from the FEFF table as provided in REX2000 computer program [15]. The backscattering amplitude and phase shift for any atomic pair can be transferred from one system to another with accuracy to ca. 0.01 Å [16-18]. If we look the photon travelling path from X-ray absorbing atom or Gold to the next nearest Nitrogen atom, the emitted photoelectron travels through a Carbon atom before reaching the Nitrogen atom.

Since the shape of Au-C-N is almost linear, the focusing effect will occur in this photon travelling path. The backscattering amplitude and phase shift values from the table might not be sufficient or providing the unsuitable values for the curve fitting. Therefore, the special treatment is needed. In this work, the special treatment is done by acquiring backscattering amplitude and phase shift values from the calculation using FEFF 8.40 software package [19]. After successful fitting the 5 K data, then the spectra for other temperatures were fitted by varying just the Debye-Waller factors and fixing all other parameters to those obtained at 5 K. Table 4.2 shows the parameters using in the curve fitting. The curve fitting was done in back k-space. The closeness of the fit was determined by the following equation.

$$R^2 = \frac{\sum(k^n \chi_{obs} - k^n \chi_{cal})^2}{\sum(k^n \chi_{obs})^2}$$

Table 4.1 Parameters using in the Fourier transformation.

Parameters	Values
k range	3.0 – 14.5 Å ⁻¹
dk	0.05
k weight	3
Window type	Hanning
Window width	10

Figure 4.8 shows the results of curve fitting in r space. The dotted lines indicate the fitting range in r space as previously described in Table 4.2. The spectra show the very good fitting results. To know how well the fitting in selected range of r region, the curve fitting results in back k-space or inverse Fourier transform are also shown in Figure 4.9. They also indicate that the very

good fitting result are obtained. The closeness of the fit or R-factor for each fitting results are shown in the Table 4.3. The obtained R-factors indicate the good fitting

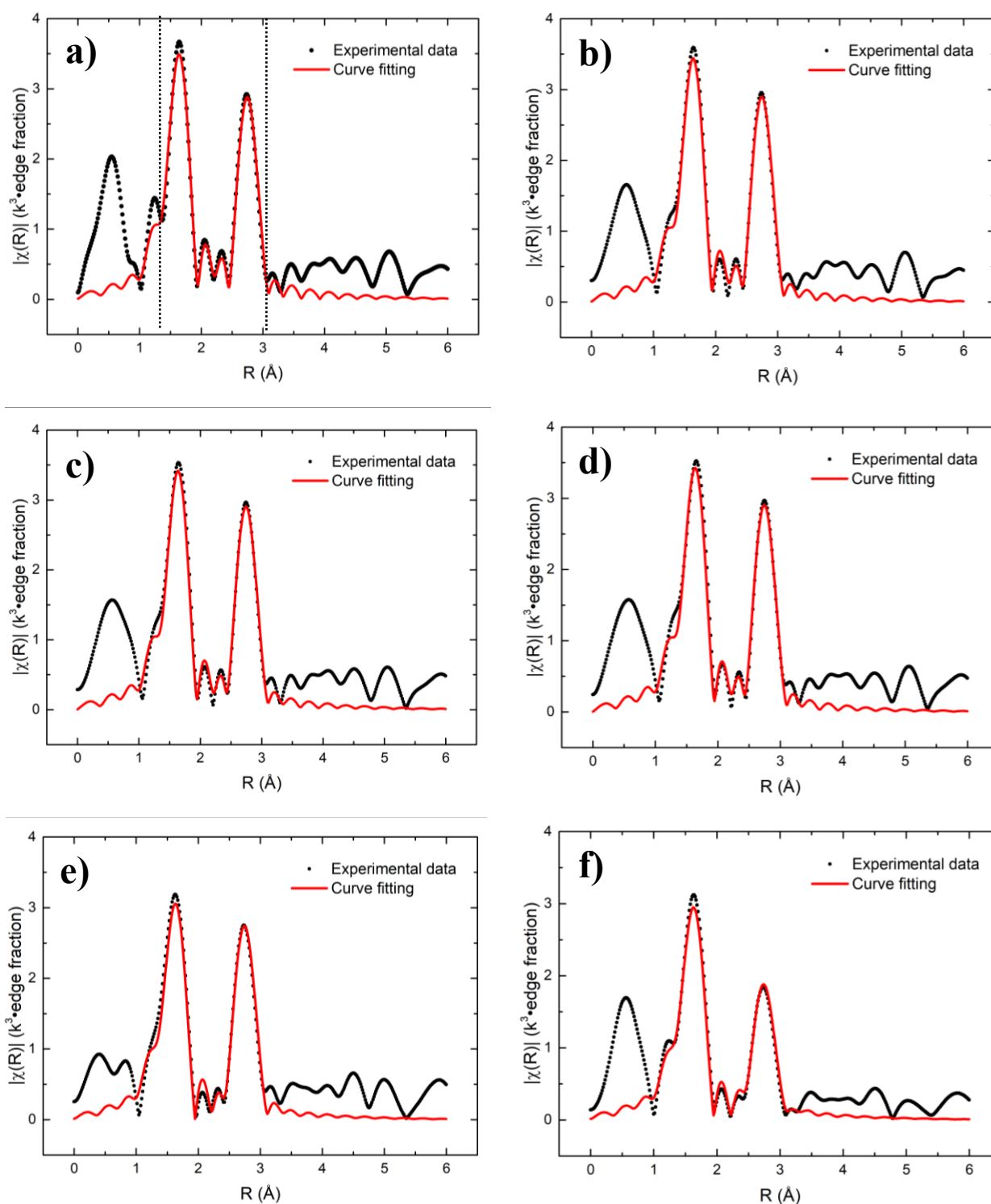


Figure 4.8 R space curve fitting of each measurement temperature a) 5 K, b) 10 K, c) 30 K, d) 50 K, e) 100 K, and f) 297 K. The dotted lines indicate the fitting range.

results and increased as expected due to the restricted parameters and the increase in uncertainty when the measurement temperature increase.

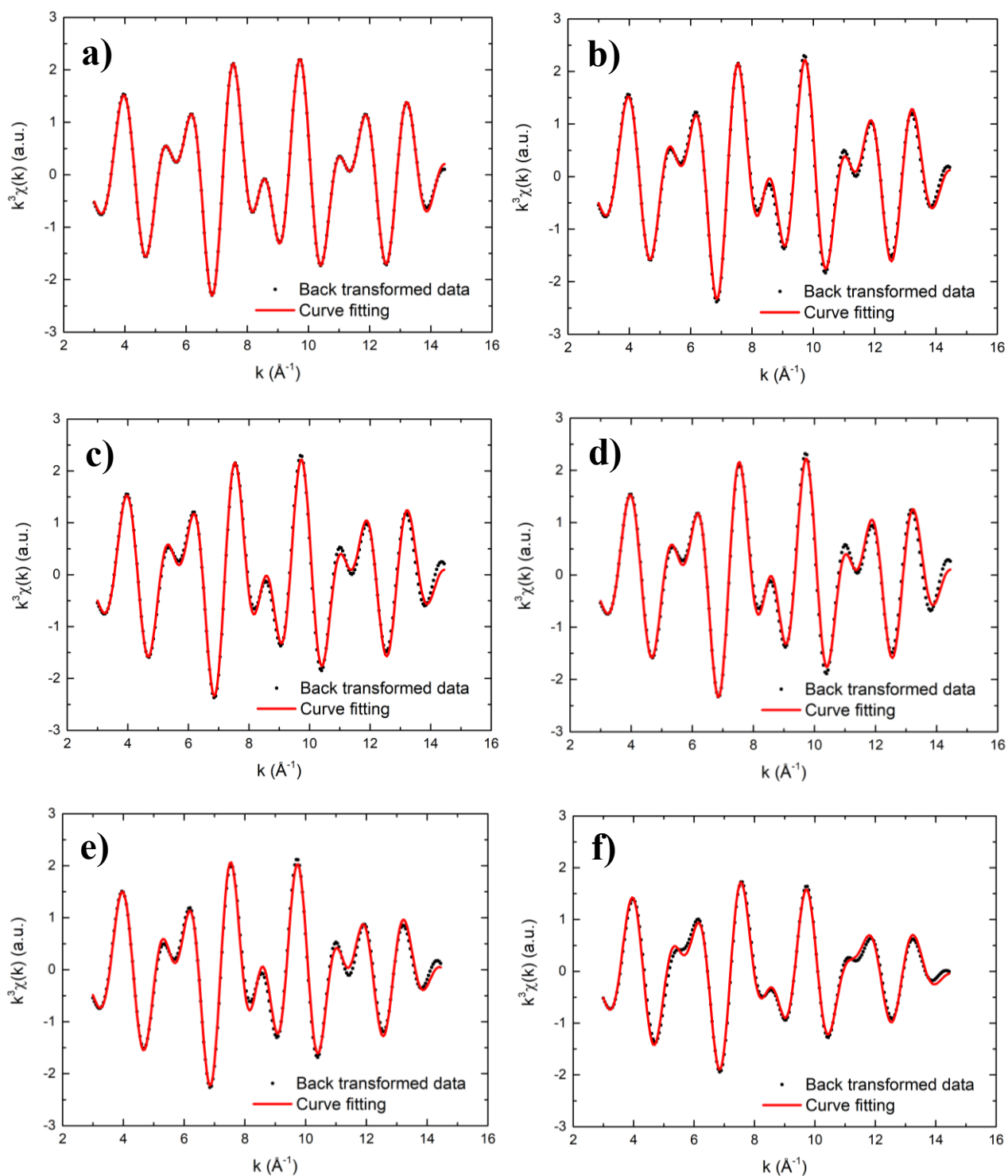


Figure 4.9 Back k -space or inverse Fourier transform curve fitting of each measurement temperature a) 5 K, b) 10 K, c) 30 K, d) 50 K, e) 100 K, and f) 297 K.

Table 4.2 parameters using in the curve fitting.

Parameters	Values
R range	1.335 – 3.084 Å
Fit method	Back k-space (Inverse Fourier transform)
Fitting range	3.0 -14.5 Å ⁻¹
Window type	Hanning
Window width	10

Table 4.3 The closeness of the fit or R-factor for each fitting results.

Temperature (K)	R-factor
5	0.04
10	0.56
30	0.85
50	1.29
100	1.05
297	0.79

Table 4.4 shows the obtained Debye-Waller factors from the fitting results. Overall, the Debye-Waller factors increase as measurement temperature increase. The environment of a single atom is not constant over time. At room temperature, most chemical bonds have vibration frequencies on the order of 10^{13} Hz which is 100 times higher of the typical core-hole lifetimes for X-ray spectroscopy. By sampling millions of atoms, we will thus be sampling the variations in absorber-scatterer distance caused by those thermal vibrations as well [20]. Therefore, the Debye-Waller factors increase because the effect of the thermal disorder increase

when temperature increase. As you can see from the table 4.4, the Debye-Waller factors for nitrogen atom are a bit higher than the carbon and gold atom. For the path of X-ray absorbing atom and Nitrogen, the photoelectron either travels first to carbon atom and then reach the nitrogen atom or directly to the nitrogen atom (depending on the scattering part it takes). The scattered photoelectron then returns back to X-ray absorbing atom by either travelling to carbon atom first and then X-ray absorbing atom or directly return to the X-ray absorbing atom (depending on the scattering part it takes). The number of atom that photoelectron in this case has to travel to is higher than the case of carbon and gold atom. Therefore, The Debye-Waller factor is a bit higher for every measurement temperature. The structural information is determined from the 5 K data set owing to the least crystal vibration hence maximum reliability. The obtained structural information is shown in Table 4.5. It has been found that there are 2 carbon atoms at distance 2.00 Å and a Nitrogen atom at distance 3.14 Å from the gold atom. These are match with the structural information obtained from the X-ray crystallography as studied previously. Aside from the Carbon and Nitrogen shell that is a part of molecular structure, another Gold atom is also found at distance 2.87 Å from the X-ray absorbing atom.

Table 4.4 Debye-Waller factors (σ) for designated atom of various measurement temperature.

Measurement Temperature (K)	Debye-Waller factor (σ) for designated atom (Å)		
	Carbon	Nitrogen	Gold
5	0.044	0.091	0.045
10	0.044	0.088	0.052
30	0.045	0.087	0.055
50	0.045	0.088	0.054
100	0.054	0.087	0.067
297	0.057	0.107	0.066

Table 4.5 The obtained structural information from 5 K data set.

Shell	Coordination number	Distance (Å)	Debye-Waller factor (σ^2)
C	1.8	2.00	0.044
N	1.3	3.14	0.091
Au	0.3	2.87	0.045

To confirm the presence of Gold atom at distance 2.87 Å from the X-ray absorbing atom, the Hamilton test[21, 22] is applied to the curve fitting result of 5 K data set. The Hamilton test or F-test is using to evaluate the significant of an improvement in R-factor obtained by adding parameters. To evaluate, the 5 K data set is subjected to curve fitting as has been done previously but including or excluding Gold shell. The curve fitting results of both kind of fitting are shown in Figure 4.10 and figure 4.11. The curve fitting that is not include the Gold shell is worse than the one that include it. The closeness of the fit or R-factor for each fitting results are shown in the Table 4.5. The curve fitting including Gold shell is almost 18 times better than the one excluding Gold shell. By determining from the parameters using in the fit, the dimension and degree of freedom can be obtained as following values, 4 and 2.81, respectively. Using these values and R-factors, evaluation of the Hamilton test leads to the conclusion that the improvement in the R-factor, obtained by introducing Au nearest neighbors, has a significance level of 99.5 %.

The need of including Gold atom in the fitting was confirmed by the Hamilton test. The coordination number of Gold shell from the curve fitting is 0.3 which is considered a bit low. In addition, its distance is almost the same as nitrogen atom. Light atom such as carbon, oxygen, nitrogen has a major contribute in k-space at lower k range. The intensity is heavier reduced as k increase. On the contrary, the spectral intensity of heavy element such as gold, silver, platinum is not heavily reduced when k increases as occurred in the light

atom. By performing curve fitting with the different k range used in the Fourier transformation, we can probe the trace contribution of gold atom. Spectral intensity in k space of Nitrogen drops rapidly and contributes tiny to the overall

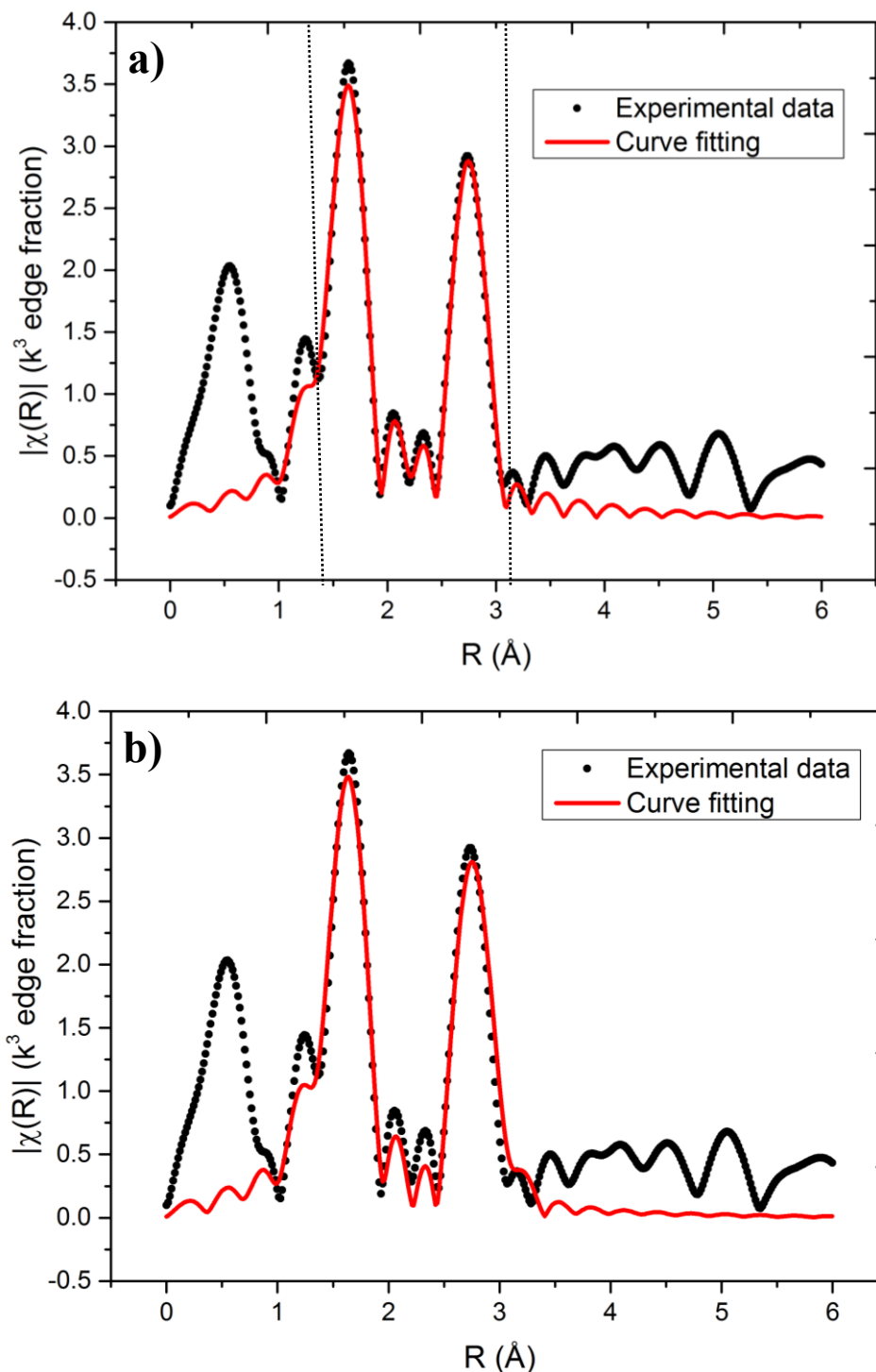


Figure 4.10 a) The curve fitting results of the 5 K data as shown in figure 4.6 (a) (include gold atom in the fitting) b) The result when exclude gold atom in the fitting. The dotted lines indicate the fitting range.

after $k = 6 \text{ \AA}^{-1}$ [23]. Using this fact, the Fourier transformation of 5 K data set with k range = 3 - 14.5 and 6 - 14.5 \AA^{-1} were performed. The results are shown in Figure 4.12. To able to compare the both spectra in r space, the normalization is

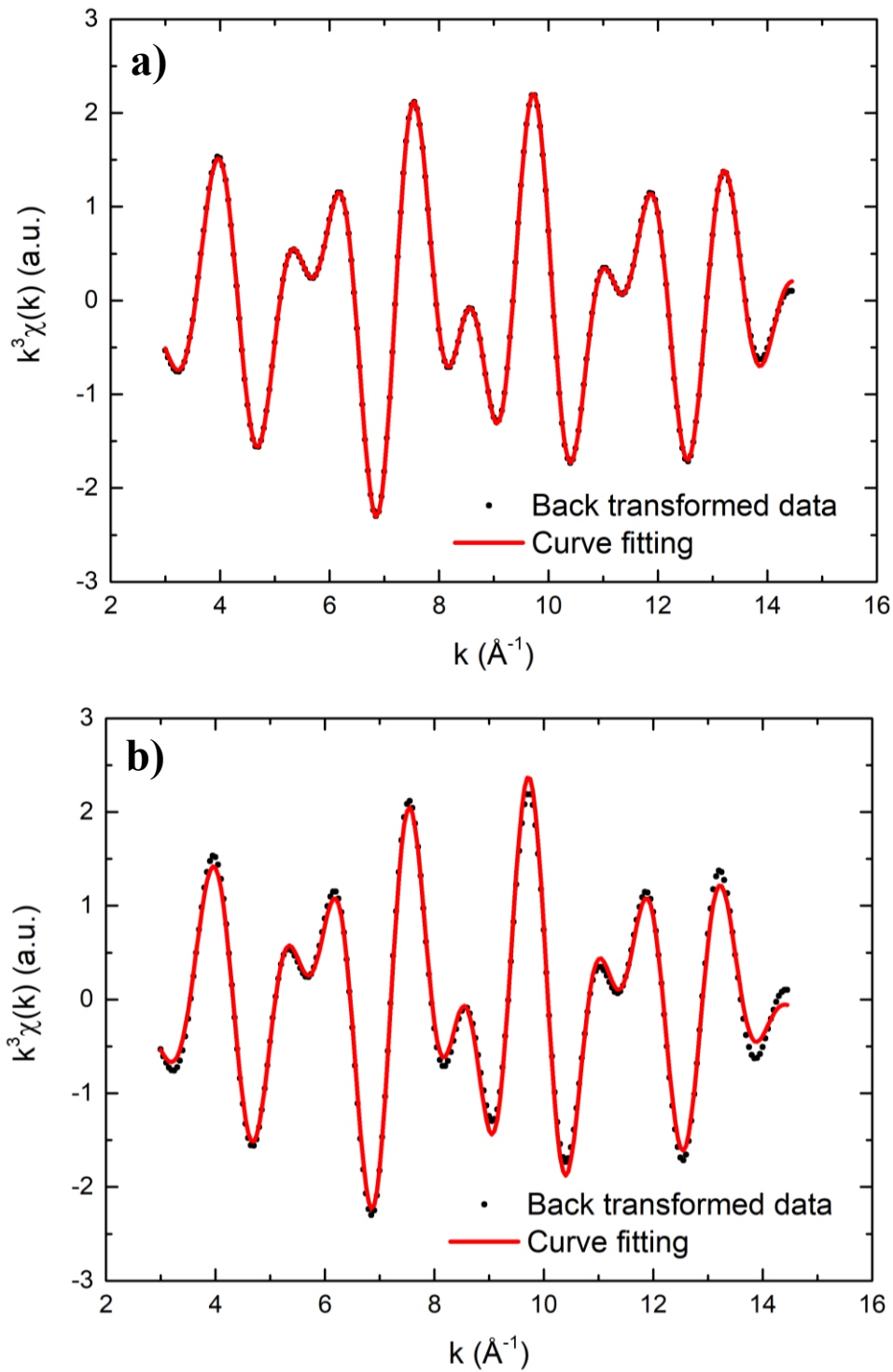


Figure 4.11 The same results as shown in figure 4.10 but in back k space or inverse Fourier transform.

performed in the spectrum that using k range = 6 - 14.5 \AA^{-1} in Fourier transformation by using the parameters from the first peak at $R = 1.7 \text{\AA}$ of spectrum that using k range = 3 - 14.5 \AA^{-1} . The clear contribution is found when comparing the peak at $R = 2.7 \text{\AA}$ which belongs to nitrogen and gold shell as shown in Figure 4.12.

Table 4.6 R-factor or the closeness of the fit of each spectrum in figure 4.10.

Gold shell	R-factor
Include	0.04
Exclude	0.68

In unground complex, the next nearest gold atom is 5.19 \AA . In addition, we know from the previous result that the molecular structure is still intact after grinding. Our finding that the distance of the next nearest gold atom reduced to 2.87 \AA might be a cause for the red shifted observed in the fluorescence spectra. It is well known that changes in intermolecular interactions change luminescence of mechanochemical compounds. As the distance between gold atom is reduced from 5.19 to 2.87 \AA , there is new type of interaction or bonding occurred which is called Auophilic interaction. Auophilic (Au–Au) interactions is observed in gold complexes with Au–Au distances in the range of 2.7–3.3 \AA [9, 24]. In the literature, Auophilic interaction responsible for the red-shift in many Au complex [2-5, 25-33]. Therefore, the reduced distance between 2 gold atoms generated the Auophilic interaction might be the cause for the mechanochromism in the material.

4.4. Conclusion

The smallest Au-Au distance between neighboring molecules is reduced to 2.87 \AA in the ground sample, in contrast to a value of 5.2 Angstrom in the

unground sample. The red-shift of the phosphorescence spectra after grinding might be due to an Auophilic interaction. Moreover, the statistical significance corresponding to the addition of nearest neighbor Gold atoms has been shown with the Hamilton test.

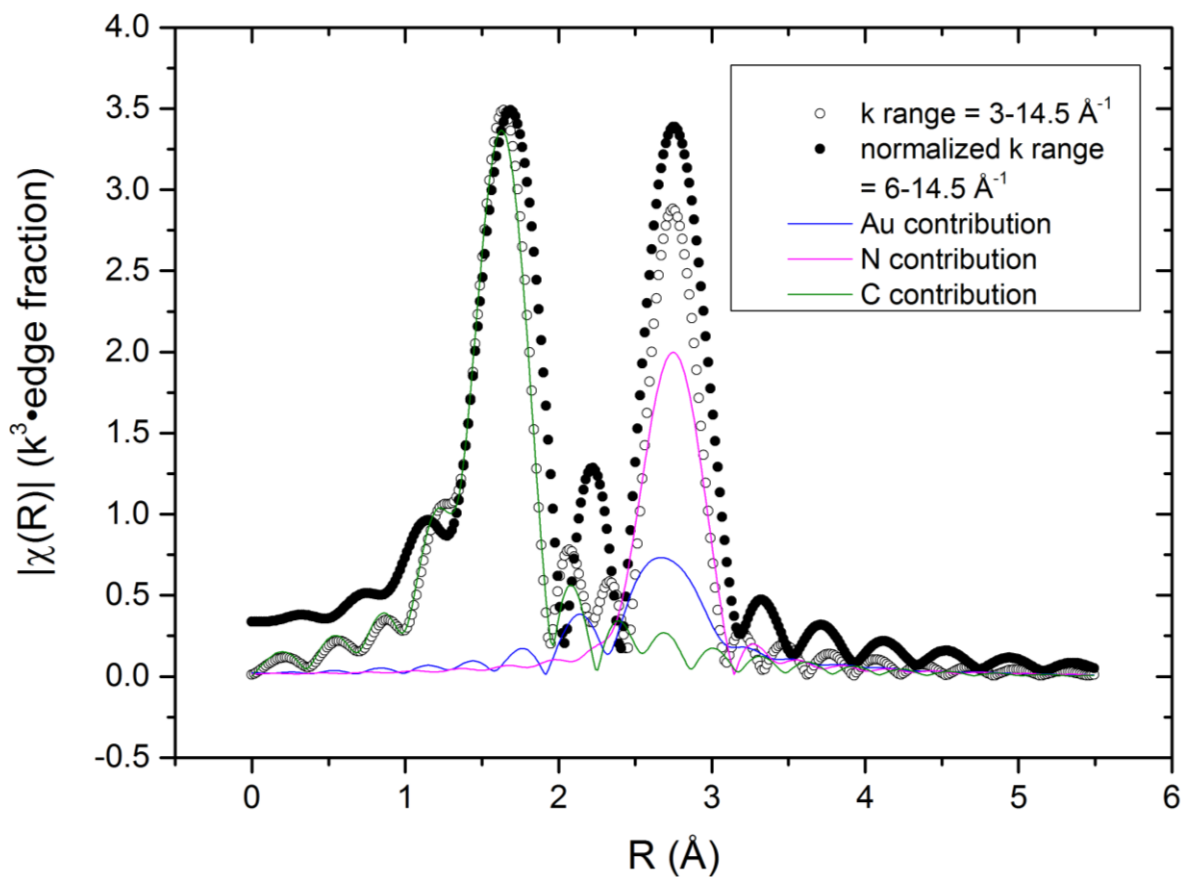


Figure 4.12 Contribution of each shell to the spectrum both complete k range and high k range.

References

- [1] H. Ito, T. Saito, N. Oshima, N. Kitamura, S. Ishizaka, Y. Hinatsu, M. Wakeshima, M. Kato, K. Tsuge, M. Sawamura, Reversible Mechanochromic Luminescence of $[(C_6F_5Au)_2(\mu-1,4-Diisocyanobenzene)]$, *Journal of the American Chemical Society*, 130 (2008) 10044-10045.
- [2] H. Ito, M. Muromoto, S. Kurenuma, S. Ishizaka, N. Kitamura, H. Sato, T. Seki, Mechanical stimulation and solid seeding trigger single-crystal-to-single-crystal molecular domino transformations, *Nature Communications*, 4 (2013) 2009.
- [3] T. Seki, K. Sakurada, H. Ito, Mismatched changes of the photoluminescence and crystalline structure of a mechanochromic gold(i) isocyanide complex, *Chemical Communications*, 51 (2015) 13933-13936.
- [4] T. Seki, K. Sakurada, M. Muromoto, S. Seki, H. Ito, Detailed Investigation of the Structural, Thermal, and Electronic Properties of Gold Isocyanide Complexes with Mechano-Triggered Single-Crystal-to-Single-Crystal Phase Transitions, *Chemistry – A European Journal*, 22 (2016) 1968-1978.
- [5] M. Jin, T. Seki, H. Ito, Mechano-Responsive Luminescence via Crystal-to-Crystal Phase Transitions between Chiral and Non-Chiral Space Groups, *Journal of the American Chemical Society*, 139 (2017) 7452-7455.
- [6] J.C. Vickery, M.M. Olmstead, E.Y. Fung, A.L. Balch, Solvent-Stimulated Luminescence from the Supramolecular Aggregation of a Trinuclear Gold(I) Complex that Displays Extensive Intermolecular Au \cdots Au Interactions, *Angewandte Chemie International Edition in English*, 36 (1997) 1179-1181.
- [7] S.H. Lim, M.M. Olmstead, A.L. Balch, Molecular Accordion: Vapoluminescence and Molecular Flexibility in the Orange and Green Luminescent Crystals of the Dimer, $Au_2(\mu-bis-(diphenylphosphino)ethane)_2Br_2$, *Journal of the American Chemical Society*, 133 (2011) 10229-10238.
- [8] M.A. Malwitz, S.H. Lim, R.L. White-Morris, D.M. Pham, M.M. Olmstead, A.L. Balch, Crystallization and Interconversions of Vapor-Sensitive, Luminescent Polymorphs of $[(C_6H_{11}NC)_2AuI](AsF_6)$ and $[(C_6H_{11}NC)_2AuI](PF_6)$, *Journal of the American Chemical Society*, 134 (2012) 10885-10893.
- [9] P. Pyykkö, Theoretical Chemistry of Gold, *Angewandte Chemie International Edition*, 43 (2004) 4412-4456.

- [10] M.J. Katz, K. Sakai, D.B. Leznoff, The use of aurophilic and other metal–metal interactions as crystal engineering design elements to increase structural dimensionality, *Chemical Society Reviews*, 37 (2008) 1884-1895.
- [11] V.W.-W. Yam, E.C.-C. Cheng, Highlights on the recent advances in gold chemistry—a photophysical perspective, *Chemical Society Reviews*, 37 (2008) 1806-1813.
- [12] A.L. Balch, Dynamic Crystals: Visually Detected Mechanochemical Changes in the Luminescence of Gold and Other Transition-Metal Complexes, *Angewandte Chemie International Edition*, 48 (2009) 2641-2644.
- [13] X. He, V.W.-W. Yam, Luminescent gold(I) complexes for chemosensing, *Coordination Chemistry Reviews*, 255 (2011) 2111-2123.
- [14] H. Schmidbaur, A. Schier, Aurophilic interactions as a subject of current research: an up-date, *Chemical Society Reviews*, 41 (2012) 370-412.
- [15] T. Taguchi, REX2000 Version 2.5: Improved DATA Handling and Enhanced User-Interface, *AIP Conference Proceedings*, 882 (2007) 162-164.
- [16] P.H. Citrin, P. Eisenberger, B.M. Kincaid, Transferability of Phase Shifts in Extended X-Ray Absorption Fine Structure, *Phys Rev Lett*, 36 (1976) 1346-1349.
- [17] P.A. Lee, B.-K. Teo, A.L. Simons, EXAFS: a new parameterization of phase shifts, *Journal of the American Chemical Society*, 99 (1977) 3856-3859.
- [18] B.-K. Teo, P.A. Lee, A.L. Simons, P. Eisenberger, B.M. Kincaid, EXAFS: approximation, parameterization, and chemical transferability of amplitude functions, *Journal of the American Chemical Society*, 99 (1977) 3854-3856.
- [19] A.L. Ankudinov, B. Ravel, J.J. Rehr, S.D. Conradson, Real-space multiple-scattering calculation and interpretation of x-ray-absorption near-edge structure, *Phys. Rev. B*, 58 (1998) 7565-7576.
- [20] S. Calvin, XAFS for Everyone, CRC press, 2013.
- [21] W.C. Hamilton, Significance tests on the crystallographic R factor, *Acta Crystallographica*, 18 (1965) 502-510.
- [22] L. Downward, C.H. Booth, W.W. Lukens, F. Bridges, A Variation of the F-Test for Determining Statistical Relevance of Particular Parameters in EXAFS Fits, *AIP Conference Proceedings*, 882 (2007) 129-131.
- [23] B.-K. Teo, P.A. Lee, Ab initio calculations of amplitude and phase functions for extended x-ray absorption fine structure spectroscopy, *Journal of the American Chemical Society*, 101 (1979) 2815-2832.
- [24] H. Schmidbaur, The aurophilicity phenomenon: A decade of experimental findings, theoretical concepts and emerging applications, *Gold Bulletin*, 33 (2000) 3-10.

- [25] T. Seki, S. Kurenuma, H. Ito, Luminescence Color-Tuning through Polymorph Doping: Preparation of a White-Emitting Solid from a Single Gold(I)–Isocyanide Complex by Simple Precipitation, *Chemistry – A European Journal*, 19 (2013) 16214-16220.
- [26] T. Seki, K. Sakurada, H. Ito, Controlling Mechano- and Seeding-Triggered Single-Crystal-to-Single-Crystal Phase Transition: Molecular Domino with a Disconnection of Auophilic Bonds, *Angewandte Chemie International Edition*, 52 (2013) 12828-12832.
- [27] T. Seki, T. Ozaki, T. Okura, K. Asakura, A. Sakon, H. Uekusa, H. Ito, Interconvertible multiple photoluminescence color of a gold(i) isocyanide complex in the solid state: solvent-induced blue-shifted and mechano-responsive red-shifted photoluminescence, *Chemical Science*, 6 (2015) 2187-2195.
- [28] T. Seki, K. Sakurada, M. Muromoto, H. Ito, Photoinduced single-crystal-to-single-crystal phase transition and photosalient effect of a gold(i) isocyanide complex with shortening of intermolecular auophilic bonds, *Chemical Science*, 6 (2015) 1491-1497.
- [29] K. Sakurada, T. Seki, H. Ito, Mechanical path to a photogenerated structure: ball milling-induced phase transition of a gold(i) complex, *CrystEngComm*, 18 (2016) 7217-7220.
- [30] T. Seki, Y. Takamatsu, H. Ito, A Screening Approach for the Discovery of Mechanochromic Gold(I) Isocyanide Complexes with Crystal-to-Crystal Phase Transitions, *Journal of the American Chemical Society*, 138 (2016) 6252-6260.
- [31] S. Yagai, T. Seki, H. Aonuma, K. Kawaguchi, T. Karatsu, T. Okura, A. Sakon, H. Uekusa, H. Ito, Mechanochromic Luminescence Based on Crystal-to-Crystal Transformation Mediated by a Transient Amorphous State, *Chemistry of Materials*, 28 (2016) 234-241.
- [32] M. Jin, T. Seki, H. Ito, Luminescent mechanochromism of a chiral complex: distinct crystal structures and color changes of racemic and homochiral gold(i) isocyanide complexes with a binaphthyl moiety, *Chemical Communications*, 52 (2016) 8083-8086.
- [33] T. Seki, M. Jin, H. Ito, Introduction of a Biphenyl Moiety for a Solvent-Responsive Aryl Gold(I) Isocyanide Complex with Mechanical Reactivation, *Inorg. Chem.*, 55 (2016) 12309-12320.

Chapter 5

Evidence for Multi-Atom Resonance X-ray Raman Spectroscopy - An *In Situ* Low Z-element and Bond-specific X-ray spectroscopy

5.1. Introduction

XAFS that has been used in the aforementioned provides invaluable local structural information. However, it is difficult to obtain the local structure around a specific compound by XAFS if the real system consists of a mixture of compounds having same X-ray absorbing atoms. Moreover, XAFS cannot distinguish whether the neighboring atoms are bonded to the absorbing atom or not. This information is invaluable for the system having the same element as of neighboring atom present elsewhere. For example, it is difficult to measure the XAFS of O on Pt nanoparticle in the water environment. Therefore, it is priceless for the development if there is a technique that can distinguish such kind of atom.

X-ray spectroscopy is a widely used technique because it has many advantages over another kind of spectroscopy. For instance, it is possible to carry out an *in situ* measurement of catalysts and electrodes under reaction conditions owing to its large penetration ability. However, when applied to low Z elements, which have an X-ray absorption edge in the soft X-ray regime (less than 1000 eV), it is quite difficult to observe the XAFS under the reaction conditions because the soft X-ray has a small penetration ability (for example, the transmittance of an X-ray with 500 eV is just 0.1 into a 1 mm-thick layer at 1 bar atmosphere).

X-ray Raman spectroscopy, however, can provide *in situ* XAFS measurements on low Z elements because the X-ray Raman technique uses hard X-rays and provides the low Z element XAFS as the X-ray energy loss spectra [1, 2]. However, the X-ray Raman intensity is quite low. Moreover, when X-ray Raman spectroscopy is applied to a real system that consists of a mixture of compounds of the same X-ray absorbing atoms, it is difficult to obtain the local

structure around a specific compound. Under visible light, a resonant Raman scattering enhances the sensitivity and selectivity by tuning the incident visible light energy to the electronic transition of the specific compound. In the X-ray region, resonant X-ray Raman scattering is observed [4] and enhances the Raman sensitivity [5]. In this resonant X-ray Raman scattering, the X-ray is tuned to the absorption edge and the Raman signal of the same X-ray absorbing atom is detected. Therefore, the X-ray absorption and Raman emission occur at a single atom. If one uses an absorption edge of the central metal in a metal complex to which low Z atoms are directly coordinated and if the excitation energy transfer occurs from the X-ray absorbing atom to the coordinating low Z atoms, one can obtain the X-ray Raman spectrum of the directly bonded low Z atoms, which is enhanced through the X-ray absorption of the central atom. To the best of our knowledge, nobody has previously estimated the probability of such a process experimentally or theoretically. In this work, we measured the interatomic resonant Raman signal. The X-ray tuned to the excitations of Ta L₃-edge and Er L₁-edge with the detection of Raman emission of N K-edge and C K-edge, respectively, in order to see such an enhancement occurs or not, qualitatively. In this preliminary work we found some possibility of the occurrence of this new type of interatomic resonant X-ray Raman.

5.2. Experimental procedure

5.2.1. Sample preparation

X-ray Raman measurements were carried out in the beam line, BL36XU of SPring-8 [3, 6]. The SPring-8 was operated in a top-up mode of the current of 100 mA and the ring energy 8 GeV. The First sample was 10 wt % TaN diluted with SiO₂. TaN and SiO₂ were used as received without further purification. The mixture was thoroughly ground and subsequently pressed to 10 mm disk. The sample content was 100 mg. The second sample was tris(cyclopentadienyl) erbium(III) (Er(C₅H₅)₃) or Er(Cp)₃. This compound is air- and water sensitive therefore it must be put in the special cell. The home-made sample holder has been designed and assembled to house the compound. Figure 5.1 shows the home-made sample holder. In the middle of the cell is polyimide film acting as an X-ray window. Each sample holder was subjected to check the leak before using it in the measurement. Then, Er(C₅H₅)₃ was put into the sample holder in a

glove box under an inert atmosphere. Er_2O_3 was used as received without further purification. Next, it was thoroughly ground and then was pressed to 10 mm disk.



Figure 5.1 Home-made sample holders.

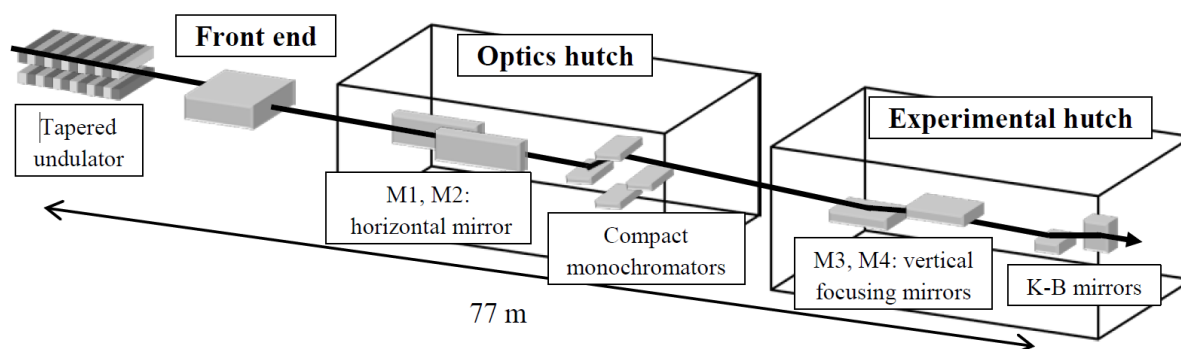


Figure 5.2 Schematic of the beamline BL36XU [3].

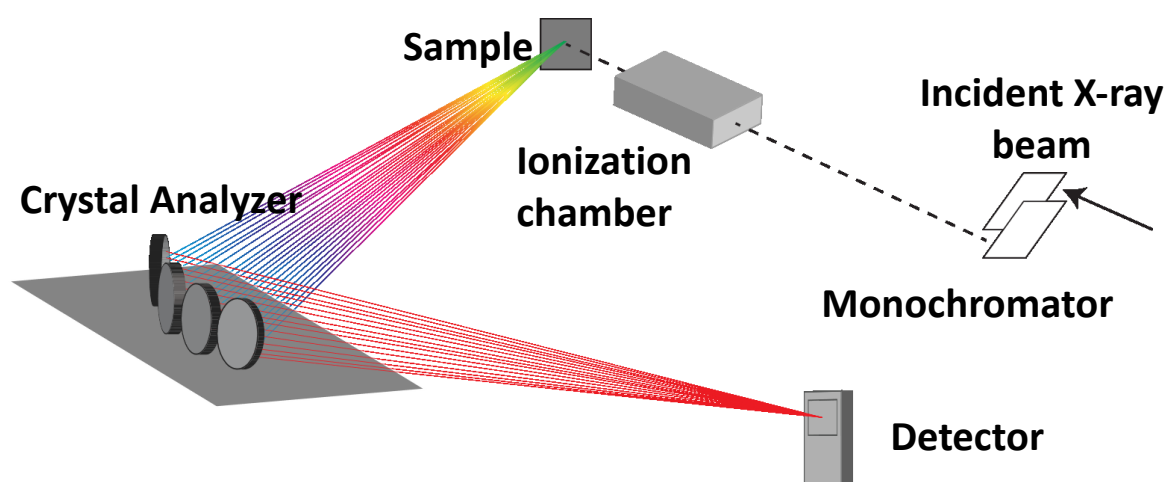


Figure 5.4 simplified diagram for the instrumental setup.

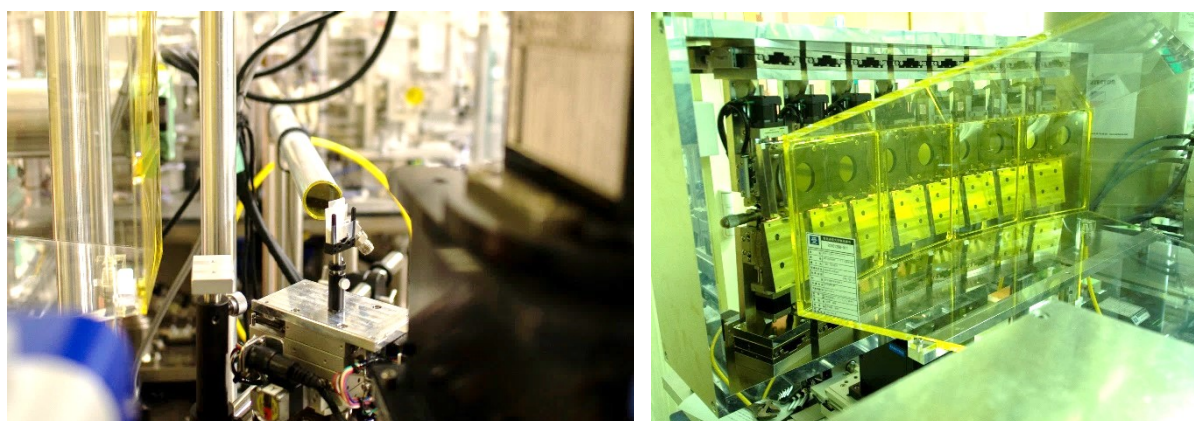


Figure 5.3 Pictures of experimental setup. Left: Sample stage, Right: Crystal Analyzers.

5.2.2. Instrument

Figure 5.2 shows the schematic of the beamline BL36XU. The high brilliant X-ray is produced by an in-vacuum type tapered undulator. The beam line comprises of 2 hutched which are optics hutch and experimental hutch. The

optics hutch consists of 2 horizontal mirrors and 2 compact monochromators. The mirror1 or M1 is a deflection mirror which is cooled by liquid-nitrogen. The mirror2 or M2 which is a water-cooled spherically bent flat mirror is used for horizontal focusing. Both M1 and M2 are 1 m long. The 2 monochromators which are a liquid-nitrogen cooled channel-cut Si(111) (for 4.5 -28 keV) and a Si(220) (for 7 -35 keV) double crystal are tandemly arrange. We can change the type of monochromator for monochromatizing the incident X-ray by using vertical translation stages without losing a vacuum. In this experiment, a Si (220) double crystal is used. The experimental hutch consists of 3 mirrors which are mirror3 (M3), mirror4 (M4) and K-B mirrors. In order to obtain a high reduction ratio of the focusing mirror, its distance is 77 m far from the light source. The M3 and M4 mirrors are the same type as M2 but used for vertical focusing and higher harmonic rejection, respectively. Both M3 and M4 are 0.7 m long. All mirrors are made of Silicon and coated by Platinum and Rhodium stripes which are able to be switched depending on the energy region of the measurement.

Figure 5.3 shows the simplified diagram for the instrumental setup and Figure 5.4 shows the pictures taken from the real measurement. The incident X-ray (I_0) is analyzed by ionization chamber. Sample is put on the sample holder where the incident X-ray beam makes a 45 degree to the sample surface. The emitted X-rays were analyzed by Johan type 4 Ge (660) monochromator located at 820 mm from the sample. The monochromator was just behind the plastic case filled with He gas. Since the emission analyzer was designed to study the Pt catalyst by high energy resolution fluorescence detection X-ray spectroscopy, the detectable range of emission energy was limited to 9440 ± 50 eV which covered the energy regions of loss spectra for N K-edge at Ta L_3 -edge. Emission intensities were plotted against both excitation and loss energies in a two-dimensional way. The energy step and spectrum range of the excitation X-ray were 1eV and 30 eV, respectively. Those of emission X-ray were 0.5eV and 30 eV, respectively. Accumulation time was 10 s per point. Then the incident X-ray energy was fixed at 9865 eV (before the edge) and 9886 eV (just on the resonance) for Ta L_3 -edge. For the Er compound, the incident X-ray energy was fixed at 9752 eV for Er L_1 -edge. Emitted X-rays from a sample were detected by a two-dimensional pixel array detector with 512 by 512 pixels (Medipix3RX; Merlin). It has been found that the intensity of the I_0 was almost constant because of the top-up mode.

The obtained data were analyzed by ImageJ2 software[7] and Python scientific computing packages [8, 9] which are NumPy [10], SciPy, Pandas [11] and IPython [12]. Color mapping is plotted by Python 2D graphics packages which are Matplotlib [13, 14] and Seaborn [15].

5.3. Results and Discussion

5.3.1. Tantalum compound

Since BL36XU is designed to study the Pt catalyst by high energy resolution fluorescence detection X-ray spectroscopy, a great amount of time spent to adjust and optimize the system for Ta L_3 -edge measurement is inevitable. Figure 5.5 shows the summation of raw data of 32 scans as was seen by the detector when scattering photon streams are scattered from the crystal analyzer. There is a tiny uniform noise scattered all over the detector area. The bright areas

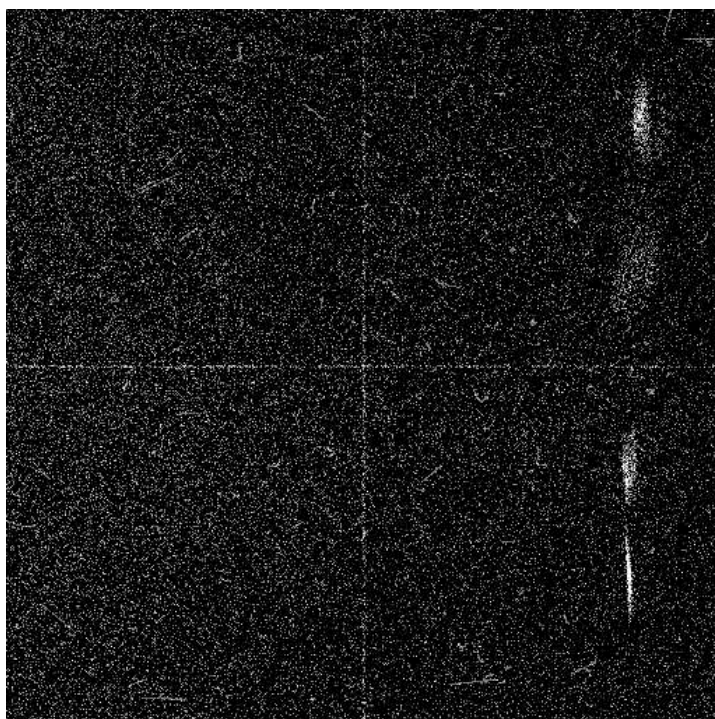


Figure 5.5 raw data as seen from the detector (32 scans).

are where the scattering photon hit the detector. These areas are then processed

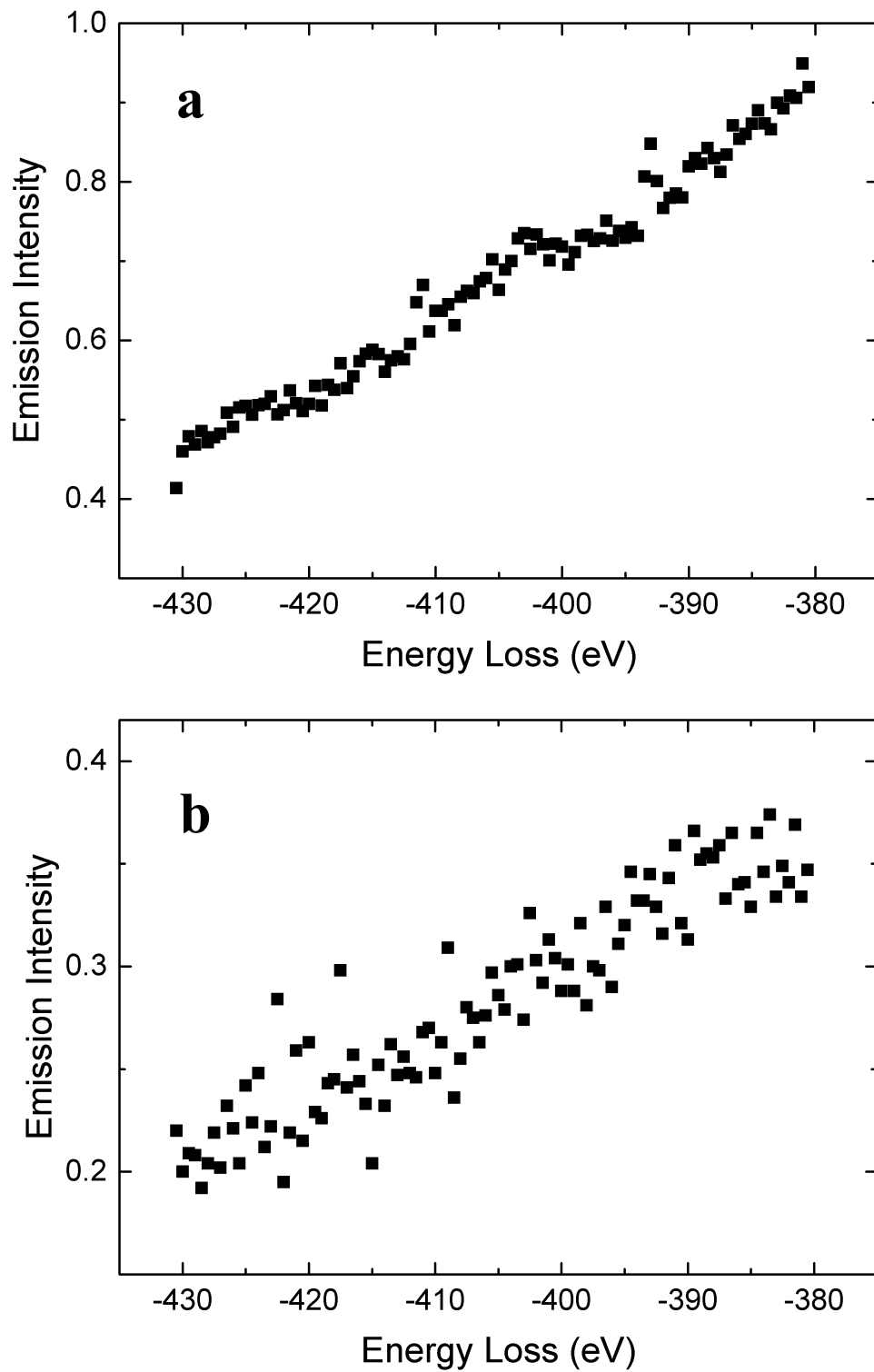


Figure 5.6 Raman spectra of 10 wt% TaN/SiO₂ when excitation energy is a) 9860 eV and b) 9886 eV.

and analyzed by the ImageJ macro scripts and python programs as mention in the experimental procedure. Figure 5.6a shows the Energy loss spectra of 10 wt% TaN/SiO₂ excited at 9860.0 eV. Ta L₃ absorption edge energy is 9881 eV. No peak appears in the spectrum. As mention earlier, the resonance condition might greatly boost the signal. Figure 5.6b shows the Energy loss spectra of 0.1 wt% TaN/SiO₂ excited at 9881.5 eV. The 10 wt% TaN/SiO₂ could not be measured at the resonant condition due to the accidentally damaged to the sample. The spectrum is noisier than the one excited at 9860 might be caused by the 100 times lower in concentration. Even though the resonance condition is met by using excitation energy just after the Ta L₃-edge, peak still not be observed in the spectrum. There are several factors that might cause the peak not appears. First, this phenomenon does not exist. Second, it might be caused by too dilute sample. Last but not least, as we can predict that this kind of phenomena have tiny

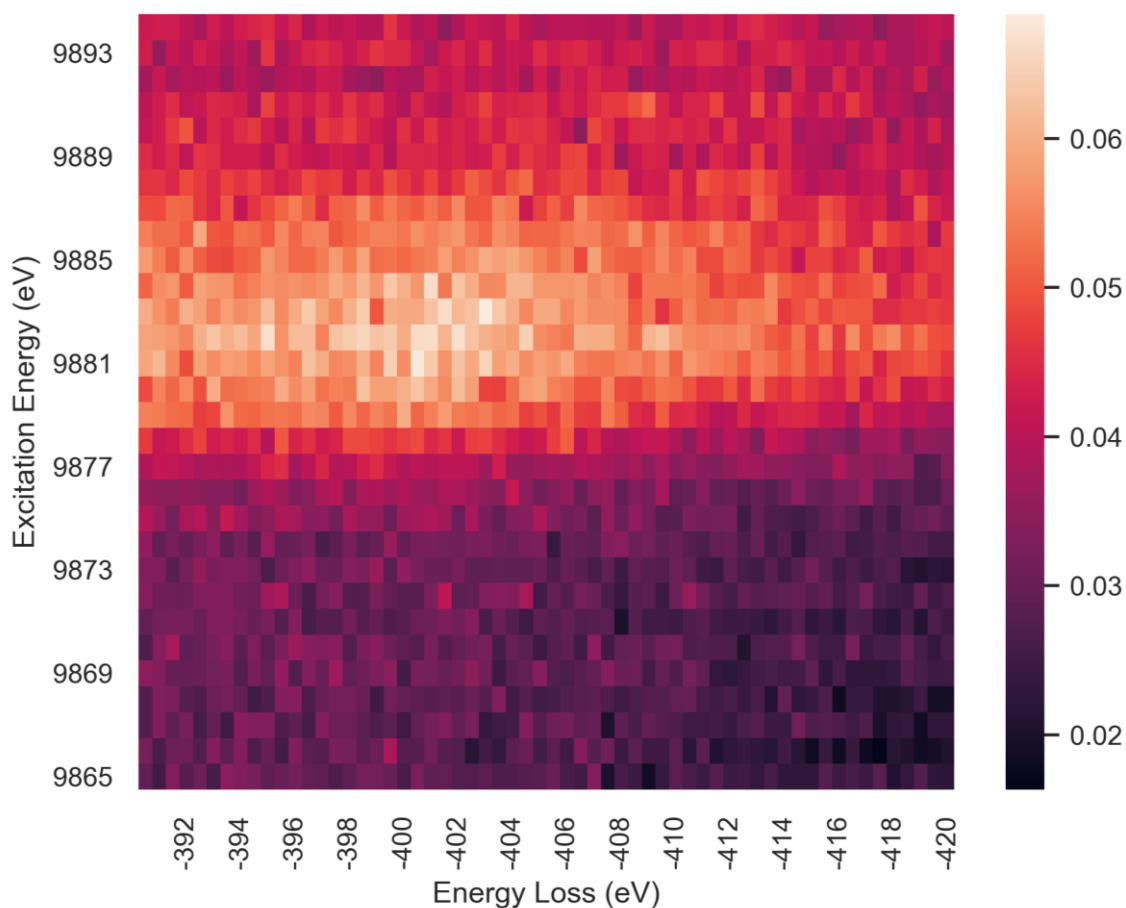


Figure 5.7 Color mapping of the scattering X-ray intensity against excitation energy and energy loss.

probability, more tuning and optimizing the measurement system will help us to detect a very faint signal in the sea of noise.

In the next beam time, adjusting and optimization for Ta L_3 -edge measurement are further done and the results look promising. Figure 5.7 shows the 2-dimensional mapping of emitted x-ray of 10 wt% TaN/SiO₂ although the spectrum is noisy. To aid the spectrum interpretation, two-dimensional gaussian smoothing which is a weighted smoothing method might help reducing data noise if the noise is random [16]. Even though the resolution is reduced after applying the smoothing, we will get the cleaner data which may aid in visualizing the spectrum. The two-dimensional gaussian smoothing which is defined by the following equation (equation 1) is applied to the same data set of Figure 5.7. The result is shown in Figure 5.8. We found the higher intensity range (bright region)

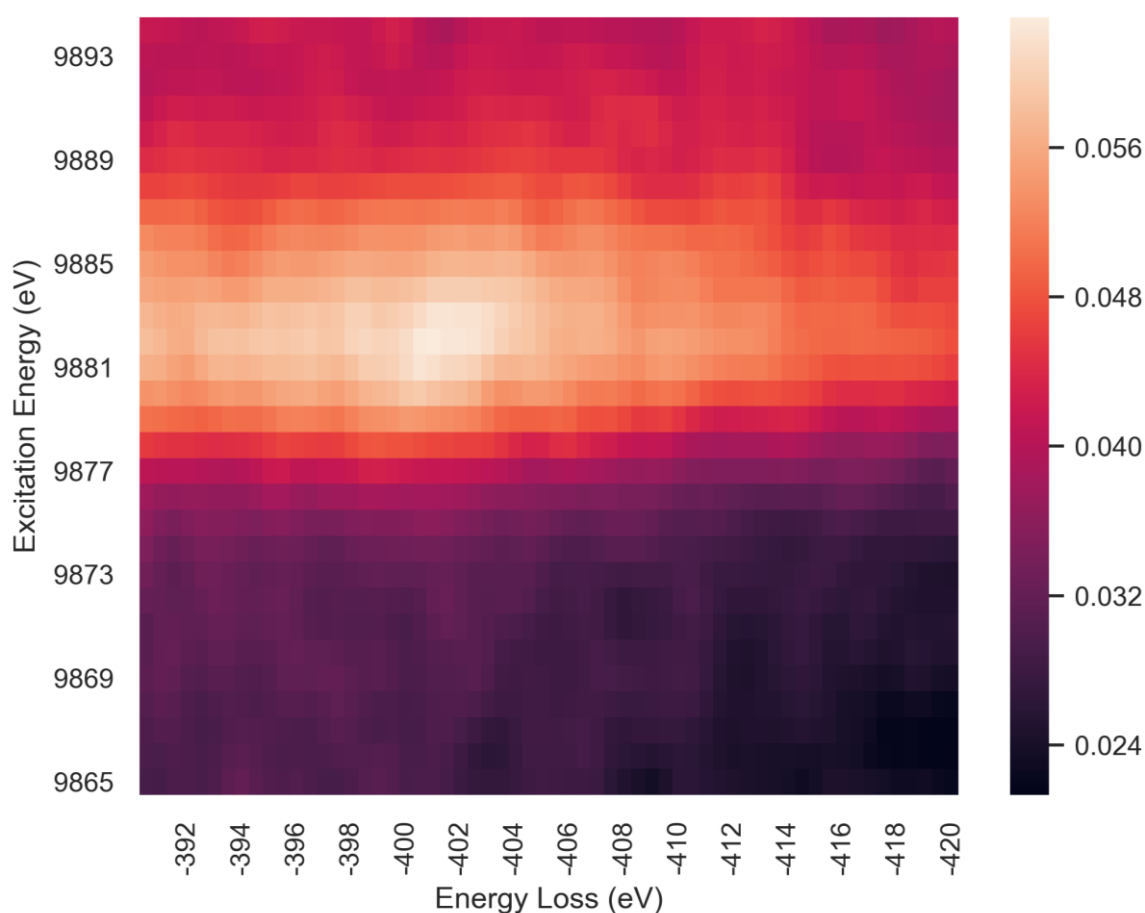


Figure 5.8 Two-dimensional Gaussian smoothing of figure 5.10 ($\sigma = 1$, padding mode = “nearest”, truncate = 3.0).

around 9881 ~ 9885 eV in the excitation energy axis and -396 ~ -404 eV in the loss energy axis. Note that Ta L₃ absorption edge energy was 9881 eV and N K-edge appears at 401 eV [17]. The high intensity region appeared at the Ta L₃ absorption edge in the excitation energy and N K-edge in the loss spectrum.

$$G(x, y) = \frac{1}{2\pi\sigma^2} e^{-\frac{x^2+y^2}{2\sigma^2}} \quad (1)$$

Figure 5.9 shows the Raman spectra TaN excited at 9865 eV (smaller than Ta L₃-edge) and 9886 eV (a little larger than Ta L₃-edge), respectively. The emission intensities were clearly changed at the N K-edge position when the sample was excited at 9886 eV. We did not find a peak in the Ta foil emission

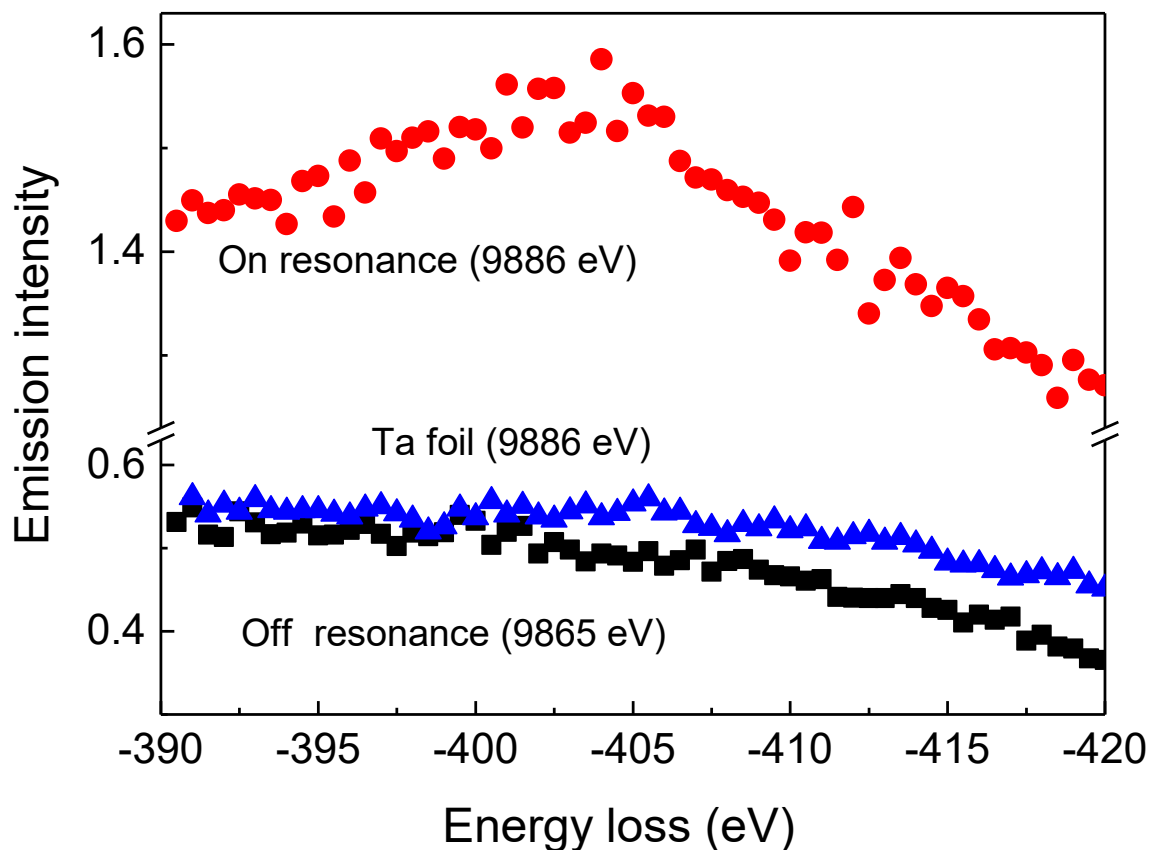


Figure 5.9 Raman spectra at 9865 eV (Black square) and 9886 eV (red circle). Blue triangle shows the emission spectrum of Ta foil.

spectra excited at 9886 eV as shown in Figure 5.9. Figures 5.7, 5.8 and 5.9 are the evidence of the possibility of enhancement effect on the N Raman signal by the neighboring Ta L₃ absorption though the S/N ratio was not so good as the N K-edge spectrum of TaN available in the literature [18].

There is a possibility to observe the peak emission line involving the transition of the electrons in the same absorbing atom. Actually, a weak N₃L₃ transition is found in the literature at 9474 eV, corresponding to -412 eV in term of energy loss in Figure 5.9 [17]. In the present case, we found the peak at -405 eV in term of energy loss or 9481 eV in term of emission energy. However, we did not find a change in the emission spectrum of Ta foil which should also have shown the emission line if it had been the N₃L₃ transition. It indicates that N₃L₃ transition intensity might be tiny.

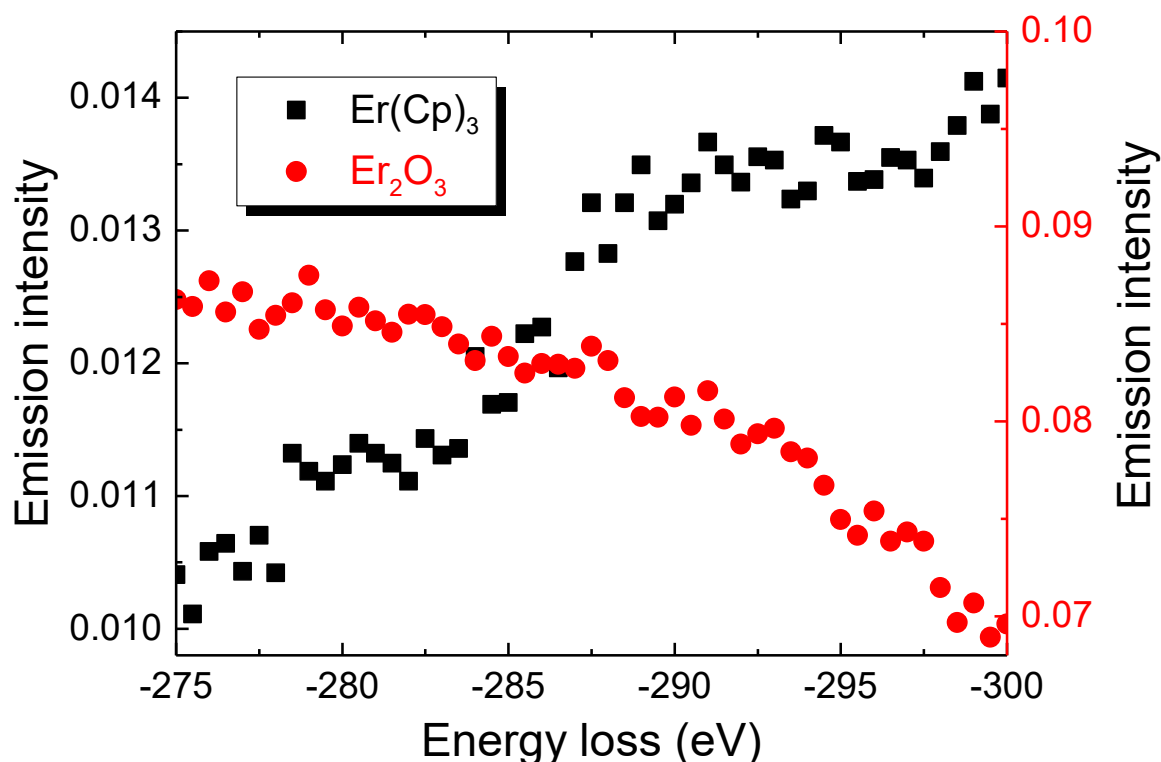


Figure 5.10 Raman spectra at 9752 eV of $\text{Er}(\text{C}_5\text{H}_5)_3$ (Black square) and Er_2O_3 (red circle).

5.3.2. Erbium compound

Figure 5.10 shows the C K-edge Raman spectra tuned at 9752 eV just above the Er L_1 -edge of $\text{Er}(\text{C}_5\text{H}_5)_3$. There was a sudden change in the emission intensities around -287 eV, the energy of which corresponded to the C K-edge loss energy. We did not find a change at corresponding loss energy around -287 eV in the Er_2O_3 emission spectra for reference in the same region as shown in Figure 5.10.

Multi-Atom Resonance X-ray Raman process is similar to MARPE (Multi-atom Resonant Photoemission) which was first demonstrated experimentally by Kay [19-21] in 2000 and theoretically by Arai in 2003 [22]. In the MARPE, the total excitation energy was transferred to the photoelectron's kinetic energy. In our process, the imperfect energy transfer occurs, and the radiated X-ray signals reflect the energy loss spectrum or Raman spectrum of N(C) K-edge similar to a radiative Auger process which was demonstrated experimentally by Kawai late 1990's [23, 24] and theoretically by Fujikawa [25] though their processes were in the same atom or intra-atomic processes. The multi-atom X-ray emission was observed in the $K\beta''$ transition where the electron in the bonding orbital directly fills the core hole [26]. In our case, the enhancement of N(C) K-edge X-ray Raman occurs using Ta(Er) L_3 -(L_1 -) edge when the resonant conditions are satisfied where the electron at the antibonding being relaxed to core hole produces the radiative Auger. There is also a criticism why a fine structure does not appear like XANES (X-ray absorption near edge structure). It might be caused by the low S/N ratio resulting in the fine structure unclear.

Although the further studies must be necessary to establish the process, this Raman process leads to a new characterization method if it is true. In this Raman spectroscopy, we can use hard X-rays to obtain the N X-ray absorption spectra. Thus, it will be a new way to perform an *in situ* measurement for low Z-element. In addition, it is a bond-specific method. Only N which has a bond to Ta is enhanced even if the other N is present. This is important when the method is applied to the real system. For example, Raman spectra of C or O adsorbed on Pt surfaces of nanoparticles can selectively be measured even if the Pt is present on graphite(C) in the water (H_2O) atmosphere like fuel cell electrodes. Since the incident X-ray energy can be fixed to a certain energy, X-ray free electron laser (XFEL) may be a good X-ray source. It will provide a high time resolution technique using the pump-probe measurement [27, 28] and the Von Hamos type

energy analyzer [29]. The new X-ray Raman spectroscopy is coined as Multi-Atom Resonant X-ray Raman (MARX-Raman) though we need many further studies such as improvement of the S/N ratio of the spectrum and the applicability to other elements as well as theoretical justifications.

5.4. Conclusion

TaN is excited at before (9865 eV) and just after (9886 eV) Ta L₃-edge and N K-edge loss spectrum is measured. Enhancement of emission spectrum is found when the excitation X-ray energy was tuned to the Ta L₃-edge and inelastic scattering spectra were recorded around 400 eV loss corresponding to the N K-edge Raman region. The enhancement at N K-edge Raman region was not observed when the excitation X-ray energy was below Ta L₃-edge. In addition, the same enhancement was not observed in Ta foil even though the excitation X-ray energy was tuned to the just after Ta L₃-edge (9886 eV). The same measurement was also applied to Er(C₅H₅)₃ with have different absorbing metal and neighboring atom. We observed the change at -286 eV loss energy position (corresponding to C K-edge Raman region), but we did not observe a clear change at C K-edge energy in the emission spectrum of Er₂O₃. Therefore, both spectra indicate the most probable assumption is Multi-Atom Resonance X-ray Raman process. These experimental results indicated the possibility of MARX-Raman phenomenon which may lead to a new *in situ* and bond-specific XAFS spectroscopy for low Z elements.

References

- [1] K. Tohji, Y. Udagawa, Novel approach for structure analysis by x-ray Raman scattering, *Phys. Rev. B*, 36 (1987) 9410-9412.
- [2] H. Hayashi, Y. Udagawa, J.-M. Gillet, W.A. Caliebe, C.-C. Kao, CHEMICAL APPLICATIONS OF INELASTIC X-RAY SCATTERING, *Chemical Applications of Synchrotron Radiation*, WORLD SCIENTIFIC, 2011, pp. 850-908.
- [3] O. Sekizawa, T. Uruga, M. Tada, K. Nitta, K. Kato, H. Tanida, K. Takeshita, S. Takahashi, M. Sano, H. Aoyagi, A. Watanabe, N. Nariyama, H. Ohashi, H. Yumoto, T. Koyama, Y. Senba, T. Takeuchi, Y. Furukawa, T. Ohata, T. Matsushita, Y. Ishizawa, T. Kudo, H. Kimura, H. Yamazaki, T. Tanaka, T. Bizen, T. Seike, S. Goto, H. Ohno, M. Takata, H. Kitamura, T. Ishikawa, T. Yokoyama, Y. Iwasawa, New XAFS beamline for structural and electronic dynamics of nanoparticle catalysts in fuel cells under operating conditions, *Journal of Physics: Conference Series*, 430 (2013) 012020.
- [4] Y. Udagawa, K. Tohji, Observation of X-ray resonant Raman spectra and transition to resonant fluorescence, *Chem. Phys. Lett.*, 148 (1988) 101-106.
- [5] U. Bergmann, P. Glatzel, S.P. Cramer, Bulk-sensitive XAS characterization of light elements: from X-ray Raman scattering to X-ray Raman spectroscopy, *Microchemical Journal*, 71 (2002) 221-230.
- [6] O. Sekizawa, T. Uruga, Y. Takagi, K. Nitta, K. Kato, H. Tanida, K. Uesugi, M. Hoshino, E. Ikenaga, K. Takeshita, S. Takahashi, M. Sano, H. Aoyagi, A. Watanabe, N. Nariyama, H. Ohashi, H. Yumoto, T. Koyama, Y. Senba, T. Takeuchi, Y. Furukawa, T. Ohata, T. Matsushita, Y. Ishizawa, T. Kudo, H. Kimura, H. Yamazaki, T. Tanaka, T. Bizen, T. Seike, S. Goto, H. Ohno, M. Takata, H. Kitamura, T. Ishikawa, M. Tada, T. Yokoyama, Y. Iwasawa, SPring-8 BL36XU: Catalytic Reaction Dynamics for Fuel Cells, *Journal of Physics: Conference Series*, 712 (2016) 012142.
- [7] C.T. Rueden, J. Schindelin, M.C. Hiner, B.E. DeZonia, A.E. Walter, E.T. Arena, K.W. Eliceiri, ImageJ2: ImageJ for the next generation of scientific image data, *BMC Bioinformatics*, 18 (2017) 529.
- [8] T.E. Oliphant, *Python for Scientific Computing*, *Computing in Science & Engineering*, 9 (2007) 10-20.
- [9] K.J. Millman, M. Aivazis, *Python for Scientists and Engineers*, *Computing in Science & Engineering*, 13 (2011) 9-12.
- [10] T.E. Oliphant, *Guide to NumPy*, CreateSpace Independent Publishing Platform, 2015.
- [11] W. McKinney, *Data Structures for Statistical Computing in Python*, in: S.v.d. Walt, J. Millman (Eds.) *Proceedings of the 9th Python in Science Conference*, Austin, Texas, 2010, pp. 51-56.

- [12] F. Perez, B.E. Granger, IPython: A System for Interactive Scientific Computing, *Computing in Science & Engineering*, 9 (2007) 21-29.
- [13] J.D. Hunter, Matplotlib: A 2D Graphics Environment, *Computing in Science & Engineering*, 9 (2007) 90-95.
- [14] M. Droettboom, T.A. Caswell, J. Hunter, E. Firing, J.H. Nielsen, N. Varoquaux, A. Lee, E.S. derade, B. Root, D. Stansby, P. Elson, D. Dale, J.-J. Lee, R. May, J.K. Seppänen, D. McDougall, A. Straw, P. Hobson, cghohlke, J. Klymak, T.S. Yu, E. Ma, S. Silvester, C. Moad, A.F. Vincent, J. Katins, N. Kniazev, F. Ariza, P. Würtz, Cimarron, matplotlib/matplotlib v2.1.2, 2018.
- [15] M. Waskom, O. Botvinnik, D. O'Kane, P. Hobson, S. Lukauskas, D.C. Gemperline, T. Augspurger, Y. Halchenko, J.B. Cole, J. Warmenhoven, J.d. Ruitter, C. Pye, S. Hoyer, J. Vanderplas, S. Villalba, G. Kunter, E. Quintero, P. Bachant, M. Martin, K. Meyer, A. Miles, Y. Ram, T. Yarkoni, M.L. Williams, C. Evans, C. Fitzgerald, Brian, C. Fonnesbeck, A. Lee, A. Qalieh, mwaskom/seaborn: v0.8.1 (September 2017), 2017.
- [16] R.C. Gonzalez, R.E. Woods, *Digital Image Processing*, 3rd ed., Prentice Hall, United States of America, 2008.
- [17] G. Zschornack, *X-Ray Emission Lines and Atomic Level Characteristics*, *Handbook of X-Ray Data*, Springer, Berlin, Heidelberg, 2007, pp. 179-609.
- [18] J.C. Jan, P.D. Babu, H.M. Tsai, C.W. Pao, J.W. Chiou, S.C. Ray, K.P.K. Kumar, W.F. Pong, M.-H. Tsai, C.A. Jong, T.S. Chin, Bonding properties and their relation to residual stress and refractive index of amorphous Ta(N,O) films investigated by x-ray absorption spectroscopy, *Appl Phys Lett*, 86 (2005) 161910.
- [19] A. Kay, E. Arenholz, S. Mun, F.J. Garcia de Abajo, C.S. Fadley, R. Denecke, Z. Hussain, M.A. Van Hove, Multi-atom resonant photoemission: A method for determining near-neighbor atomic identities and bonding, *Science*, 281 (1998) 679-683.
- [20] A.W. Kay, E. Arenholz, B.S. Mun, J.G. de Abajo, C.S. Fadley, R. Denecke, Z. Hussain, M.A. Van Hove, Multiple atom resonant photoemission: A new technique for studying near-neighbor atomic identities and bonding, *J Electron Spectrosc Relat Phenom*, 101 (1999) 647-652.
- [21] A.W. Kay, F.J.G. de Abajo, S.H. Yang, E. Arenholz, B.S. Mun, N. Mannella, Z. Hussain, M.A. Van Hove, C.S. Fadley, Multiatom resonant photoemission, *Phys. Rev. B*, 63 (2001) 115119.
- [22] H. Arai, T. Fujikawa, Theoretical Study of Multi-atom Resonant Photoemission, *Journal of Surface Analysis*, 14 (2008) 352-355.
- [23] J. Kawai, K. Hayashi, Y. Awakura, Extended X-ray absorption fine structure (EXAFS) in X-ray fluorescence spectra, *J. Phys. Soc. Jpn.*, 66 (1997) 3337-3340.
- [24] J. Kawai, T. Yamamoto, Y. Harada, S. Shin, Fluorine $K\alpha$ X-ray fluorescence spectra of MnF₂ excited at threshold, *Solid State Communications*, 105 (1998) 381-385.
- [25] T. Fujikawa, J. Kawai, Theory on extended X-ray emission spectra, *J. Phys. Soc. Jpn.*, 68 (1999) 4032-4036.

- [26] C.J. Pollock, S. DeBeer, Valence-to-Core X-ray Emission Spectroscopy: A Sensitive Probe of the Nature of a Bound Ligand, *Journal of the American Chemical Society*, 133 (2011) 5594-5601.
- [27] Y. Uemura, H. Uehara, Y. Niwa, S. Nozawa, T. Sato, S. Adachi, B. Ohtani, S. Takakusagi, K. Asakura, In Situ Picosecond XAFS Study of an Excited State of Tungsten Oxide, *Chemistry Letters*, 43 (2014) 977-979.
- [28] Y. Uemura, D. Kido, Y. Wakisaka, H. Uehara, T. Ohba, Y. Niwa, S. Nozawa, T. Sato, K. Ichiyonagi, R. Fukaya, S.-i. Adachi, T. Katayama, T. Togashi, S. Owada, K. Ogawa, M. Yabashi, K. Hatada, S. Takakusagi, T. Yokoyama, B. Ohtani, K. Asakura, Dynamics of Photoelectrons and Structural Changes of Tungsten Trioxide Observed by Femtosecond Transient XAFS, *Angewandte Chemie International Edition*, 55 (2016) 1364-1367.
- [29] J. Szlachetko, M. Nachtegaal, E. de Boni, M. Willmann, O. Safonova, J. Sa, G. Smolentsev, M. Szlachetko, J.A. van Bokhoven, J.C. Dousse, J. Hozowska, Y. Kayser, P. Jagodzinski, A. Bergamaschi, B. Schmitt, C. David, A. Lucke, A von Hamos x-ray spectrometer based on a segmented-type diffraction crystal for single-shot x-ray emission spectroscopy and time-resolved resonant inelastic x-ray scattering studies, *Review of Scientific Instruments*, 83 (2012) 103105.

Chapter 6

General conclusion

The present work demonstrates the usefulness of XAFS for investigation of the local structure of various systems which show unique properties, but it is difficult to obtain its structure. The conclusion of each system is briefly given below.

Ni and Pt evaporated onto the premodified surface $\text{TiO}_2(110)$ with *o*-MBA are investigated. Atomically dispersed Ni species were formed on a $\text{TiO}_2(110)$ surface premodified with *o*-MBA. The three-dimensional structure of the Ni species was determined using the PTRF-EXAFS technique. A S-Ni-O motif, which is similar to the local metal structure found in previous studies with Cu and Au, was formed on the modified $\text{TiO}_2(110)$ surface. In contrast, Pt was not atomically dispersed but instead aggregated to form clusters on the *o*-MBA/ $\text{TiO}_2(110)$ due to the low affinity of Pt atoms for S atoms compared with that for other Pt atoms. These results demonstrate that Polarization-dependent X-ray absorption fine structure (PTRF-XAFS) analysis can uniquely provide three-dimensional structural information around highly dispersed metal species on the single crystal surface which conventional XAFS cannot. In addition, A new indicator, R_{X-M-O} (X=S or O), has been proposed for the single metal dispersion on the $\text{TiO}_2(110)$ surface. This indicator would help the scientific community predict whether metal could be used to obtain the highly dispersed on the $\text{TiO}_2(110)$ surface.

The gold (I) complex $[(\text{C}_6\text{F}_5\text{Au})_2(\mu\text{-}1,4\text{-diisocyanobenzene})]$ exhibit the unique properties called reversible mechanochromism. The luminescence color was changed, from blue to yellow, when applying the mechanical force such as grinding with a spatula. The polycrystalline state is changed to the amorphous state as expected when applying the mechanical force. According to the author, it was found that grinding does not destroy the molecular structure. Recrystallization of the complex yields the single crystal suitable for the single crystal X-ray diffraction analysis. Single crystal X-ray diffraction (XRD) reveals the structure of blue luminescence polymorph having Single crystal X-ray diffraction (XRD) reveals the structure of blue luminescence polymorph having

shortest Au-Au distance around 5.19 Å. The amorphous state that exhibits yellow luminescence, however, remains unknown. I applied the Extended X-ray Absorption Fine Structure (EXAFS) to get the local structure of Au. EXAFS results show that the shortest Au-Au distance is reduced to 2.87 Å. As a result, the ground crystal has the new kind of interaction called Auophilic interaction which is not found in the blue polymorph. The Auophilic interaction might be the origin for the mechanochromism. Moreover, the statistical significance corresponding to the addition of nearest neighbor Gold atoms has been shown with the Hamilton test. This test will be a big help for us working on a complicated system which has a lot of element. When fitting data to theoretical standards such as those obtained from the FEFF calculation, a common question when fitting EXAFS data is to ask whether adding another shell (which often includes the addition of multiple parameters) would significantly improve the fit. Another question found in the common EXAFS analysis is whether including additional parameters for a given scattering shell, such as a third cumulant, is significant or not. Applying the Hamilton test during the analysis process helps us determining relevancy in EXAFS and get rid of data errors especially when the system being studied has the shell that slightly contribution to the overall EXAFS oscillation, as described previously.

XAFS that has been used in the aforementioned provides invaluable local structural information. However, when applied to low Z elements, which have an X-ray absorption edge in the soft X-ray regime, it is quite difficult to observe the XAFS under the reaction conditions. If one uses an absorption edge of the central metal in a metal complex to which low Z atoms are directly coordinated and if the excitation energy transfer occurs from the X-ray absorbing atom to the coordinating low Z atoms, one can obtain the X-ray Raman spectrum of the directly bonded low Z atoms. This will help us receive a deep understanding of what happens in catalysis or fuel-cell system in working condition. Describe below is the evidence for the new phenomena I found that might lead to the development of new kind of spectroscopy

TaN is excited at before (9865 eV) and just after (9886 eV) Ta L₃-edge and N K-edge loss spectrum are measured. Enhancement of emission spectrum is found when the excitation X-ray energy was tuned to the Ta L₃-edge and inelastic scattering spectra were recorded around 400 eV loss corresponding to the N K-edge Raman region. The enhancement at N K-edge Raman region was not observed when the excitation X-ray energy was below Ta L₃-edge. In addition,

the same enhancement was not observed in Ta foil even though the excitation X-ray energy was tuned to the Ta L_3 -edge. The same measurement was also applied to $\text{Er}(\text{C}_5\text{H}_5)_3$ with have different absorbing metal and neighboring atom. We observed the change at -286 eV loss energy position (corresponding to C K-edge Raman region), but we did not observe a clear change at C K-edge energy in the emission spectrum of Er_2O_3 . Therefore, both spectra indicate the most probable assumption is Multi-Atom Resonance X-ray Raman process. These experimental results indicated the possibility of MARX-Raman phenomenon which may lead to a new *in situ* and bond-specific XAFS spectroscopy for low Z elements. In this Raman spectroscopy, we can use hard X-rays to obtain the N X-ray absorption spectra. Thus, it will be a new way to perform an *in situ* measurement for low Z-element. In addition, it is a bond-specific method. The Only N which has a bond to Ta is enhanced even if the other N is present. This is important when the method is applied to the real system. For example, Raman spectra of C or O adsorbed on Pt surfaces of nanoparticles can selectively be measured even if the Pt is present on graphite(C) in the water (H_2O) atmosphere like fuel cell electrodes. Since the incident X-ray energy can be fixed to a certain energy, X-ray free electron laser (XFEL) may be a good X-ray source. It will provide a high time resolution technique using the pump-probe measurement [1, 2] and the Von Hamos type energy analyzer [3]. The new X-ray Raman spectroscopy is coined as Multi-Atom Resonant X-ray Raman (MARX-Raman) though we need many further studies such as improvement of the S/N ratio of the spectrum and the applicability to other elements as well as theoretical justifications.

In summary, XAFS methods are able to determine local structure around metal and provide the local structural information precisely. Moreover, the new possible phenomena I found that might lead to the development of new kind of spectroscopy are introduced. These works have contributed to XAFS spectroscopy and material science in the following way.

1. I demonstrated that three-dimensional structural information of the highly dispersed metal species on the single crystal surface could be obtained by PTRF-EXAFS, unlike conventional EXAFS which cannot provide such information.
2. A new indicator, R_{X-M-O} (X=S or O), has been proposed for the single metal dispersion on the $\text{TiO}_2(110)$ surface. It provides us the new way to predict how well the dispersion of the metal species on the $\text{TiO}_2(110)$ surface.

3. I demonstrated how Hamilton test or F-test plays an important role in curve fitting analysis of the complicated system in which slightly contribution to the overall oscillation of the atomic species could be identified. It helps in answering the common question when fitting EXAFS data “adding the particular shell or parameter will significantly improve the fit or not”.
4. I demonstrated the evidence that might lead to the development of a new kind of spectroscopy. With further study this new phenomenon, which has coined the name as Multi-Atom Resonant X-ray Raman (MARX-Raman), it will be a new way to perform an *in situ* XAFS measurement for low Z-element with bond-specific capability. It will provide the insight information of the catalysts, electrode under working condition. The fuel cell research is an example to gain a huge benefit from the new technique.

References

- [1] Y. Uemura, H. Uehara, Y. Niwa, S. Nozawa, T. Sato, S. Adachi, B. Ohtani, S. Takakusagi, K. Asakura, In Situ Picosecond XAFS Study of an Excited State of Tungsten Oxide, *Chemistry Letters*, 43 (2014) 977-979.
- [2] Y. Uemura, D. Kido, Y. Wakisaka, H. Uehara, T. Ohba, Y. Niwa, S. Nozawa, T. Sato, K. Ichiyanagi, R. Fukaya, S.-i. Adachi, T. Katayama, T. Togashi, S. Owada, K. Ogawa, M. Yabashi, K. Hatada, S. Takakusagi, T. Yokoyama, B. Ohtani, K. Asakura, Dynamics of Photoelectrons and Structural Changes of Tungsten Trioxide Observed by Femtosecond Transient XAFS, *Angewandte Chemie International Edition*, 55 (2016) 1364-1367.
- [3] J. Szlachetko, M. Nachtegaal, E. de Boni, M. Willmann, O. Safonova, J. Sa, G. Smolentsev, M. Szlachetko, J.A. van Bokhoven, J.C. Dousse, J. Hozowska, Y. Kayser, P. Jagodzinski, A. Bergamaschi, B. Schmitt, C. David, A. Lucke, A von Hamos x-ray spectrometer based on a segmented-type diffraction crystal for single-shot x-ray emission spectroscopy and time-resolved resonant inelastic x-ray scattering studies, *Review of Scientific Instruments*, 83 (2012) 103105.